



**FRIEDRICH-SCHILLER-
UNIVERSITÄT
JENA**

**Optical design methods of non-
rotationally symmetric optical systems
with freeform surfaces**

Dissertation

for the acquisition of the academic title

Doctor Rerum Naturalium (Dr. rer. nat.)

submitted to the Council of the Faculty of Physics and Astronomy

of Friedrich-Schiller-Universität Jena

By M.Sc. Yi Zhong

born in Guiyang, Guizhou Province, China on 12.06.1989

Gutachter:

1. Prof. Dr. Herbert Gross, Friedrich-Schiller-Universität Jena
2. Prof. Dr. Alois Herkommer, Universität Stuttgart
3. Prof. Dr. Rongguang Liang, the University of Arizona

Day of the Disputation: 25 October 2018

Zusammenfassung

Heutzutage spielen Freiformflächen eine wichtige Rolle bei der Verbesserung der Abbildungsleistung in nicht-rotationssymmetrischen optischen Systemen. Allerdings gibt es derzeit noch keine allgemeingültigen Regeln für das Design mit Freiformflächen. Das Ziel dieser Arbeit ist es zum Design nicht-rotationssymmetrischer Systeme mit einer Methode zur Startsystementwicklung, der Analyse und Korrektur von Bildfehlern, sowie Regeln zur Positionierung der Freiformflächen beizutragen.

Zuerst wird eine Methode zur Startsystementwicklung basierend auf der nodal-aberration-theory und der Gaussian-brackets aufgezeigt. Ein gutes Startsystem hat nur minimale Bildfehler, sowie eine sinnvolle Struktur, bevor Freiformflächen angewendet werden können. Die Gaussian-brackets-Methode ist hierbei nicht auf den Systemtyp oder die Anzahl der Flächen beschränkt. Die Bildfehler werden dann mit der Methode der kleinsten Quadrate optimiert.

Die vektorielle Bildfehlertheorie ist wichtig für Designstrategien und die Bewertung des Systems. Auf dieser Grundlage werden Designstrategien zum Ermitteln von Knotenpunkten für Koma und Astigmatismus abgeleitet. Die Auswahlregeln zur Positionierung von Asphären und Freiformflächen resultieren aus dem Verhalten in Abhängigkeit der Position zur Pupille.

Da bikonische Flächen im Design von Freiformsystemen häufig als Grundform verwendet werden, werden die daraus erzeugten Bildfehler abgeleitet. Damit kann aus der Bildfehlertheorie geschlossen werden, dass Koma und Astigmatismus, die durch die bikonische Fläche erzeugt werden, entkoppelt sind, was ein Vorteil ist, um Knotenpunkte für Startsystem zu erhalten.

Die Methode zur Startsystementwicklung mit Gaussian-brackets wird mit TMAs demonstriert. Darüber hinaus wird erweitertes Yolo-Teleskop mit drei Spiegeln und einer kleinen Blendenzahl designt. Das feldkonstante Koma wird hier durch die Strategie basierend auf der nodal-aberration-theory korrigiert. Der große Astigmatismus wird durch die bikonische Grundformen, sowie Freiform-polynome höherer Ordnung korrigiert. Auf der Grundlage der Auswahlregeln ist ein Scheimpflug-System in dieser Arbeit mit zwei Freiform-Oberflächen designt. Es ist erwiesen, dass die Uniformität eines Scheimpflug-Systems nur mit Freiformflächen ausbalanciert werden kann.

This page is left blank intentionally.

Abstract

Nowadays freeform surfaces play important roles in improving the imaging performance in non-rotationally symmetric optical systems. However, there are currently no general rules for the design with freeform surfaces. In this work, the aim is to contribute to the workflow of non-rotationally symmetric system design with the initial system design method, the analysis and the correction of aberrations in the systems, and the position selection rules for freeform surfaces.

Firstly, an initial system design method is proposed based on nodal aberration theory and Gaussian brackets. A good initial system with minimum aberrations and reasonable structure is essential before adding freeform surfaces. The other already existing methods are limited to certain types of systems. The Gaussian brackets method is not limited to the system type or the number of surfaces. The aberrations are optimized using the nonlinear least-squares solver.

The vectorial aberration theory is important for design strategies and the performance evaluation. Thus, design strategies for obtaining nodal points of coma and astigmatism are concluded in this work based on the vectorial aberration theory. The surface position selection rules for aspheres and freeform surfaces are also generated based on the different behaviors when the surface is located at or away from the pupil.

Since the biconic surface is often used as the basic shape in the freeform system design, the aberrations generated by the biconic surface are derived in this work. Thus, it is concluded from the aberration theory that coma and astigmatism generated by the biconic surface are decoupled, which is a benefit to obtain nodal points when designing initial systems.

Based on the Gaussian brackets initial system design method, initial setups of TMA systems are designed to demonstrate the design procedure. An extended Yolo telescope with three mirrors is designed with a small f-number. The field-constant coma is corrected by the strategy based on nodal aberration theory. The large astigmatism is further corrected using biconic surfaces and higher order freeform polynomials. Based on the selection rules, a Scheimpflug system is designed in this work with two freeform surfaces. It is proved that the uniformity of Scheimpflug systems can be balanced only with freeform surfaces.

This page is left blank intentionally.

Contents

Zusammenfassung	i
Abstract	iii
Contents	1
1 Introduction and motivation.....	3
2 State of the art.....	6
2.1 Initial system design methods.....	6
2.2 Traditional aberration theory	8
2.3 Nodal Aberration Theory	13
2.4 Gaussian brackets and Generalized Gaussian Constants.....	17
2.5 Aspheres.....	20
2.6 Freeform surface representations	24
2.7 Traditional design process	28
2.8 Problems for non-rotationally symmetrical systems	31
3 New methods and results.....	36
3.1 Vectorial aberration theory	36
3.2 Parabasal reference.....	40
3.3 Initial system finding.....	42
3.3.1 Conic-confocal method	43
3.3.2 Gaussian brackets method.....	51
3.4 Obscuration.....	61
3.5 Aberrations.....	65
3.5.1 Primary coefficients.....	66
3.5.2 Zernike fringe freeform surface	70
3.5.3 Impact of a biconic basic shape	73
3.6 Selection of freeform surface position.....	78
4 Examples and applications	81
4.1 TMA system	81
4.2 Yolo telescope	87
4.3 Scheimpflug system.....	91
5 Conclusions	99
Appendix A: Vector relations	101

Appendix B: Aberrations generated by Zernike fringe freeform polynomials.....	103
Appendix C: Verification of the aberrations generated by the biconic surface.....	115
References	117
List of Figures	121
List of Tables	124
List of Abbreviations	126
List of Symbols	127
Acknowledgement	131
Ehrenwörtliche Erklärung	132
Curriculum Vitae	133
Publications	134

1 Introduction and motivation

In the past, a large number of optical systems are rotationally symmetric due to the limitation of computational and manufacturing techniques and the benefits of symmetry. Before the existing of computers, telescopes with small fields but good imaging quality were already designed. With the appearance of photography, many good camera lens systems have been designed and produced in the last centuries, which have extended field-of-view (FOV) compared with the old telescope systems. However, the lens design technology developed quite slowly until the existing of computers. Although aberration theory and ray tracing were established before that, the computing capacity was poor with only a small number of rays. The designers should have enough experience to determine the direction and changes of the design [1].

Since the middle of 20th century, computers were programmed to trace a large number of rays, illustrate the system analysis, and realize the optimization of the system [1]. With the fast development of computer technology, it also allows the possibility to couple complicated mathematics in the design process, for instance, the surface shape can be extended to aspherical or freeform surfaces with series of polynomials. Therefore, the development of optical design was highly improved in the last decades relying on the improvement of computational technology and manufacturing technology.

Nowadays, the specifications of design become more challenging towards the trend of small F-number, large FOV, very compact size, low cost, etc. Many good imaging systems are designed such as fish-eye objectives, zoom lens system, microscope objectives, and lithography systems.

Additionally, systems without rotational symmetry are investigated in specialized applications. Off-axis three mirror anastigmats (TMAs) are designed to achieve high resolution, small size, and obscuration free due to the folding of the ray paths [2]. By combining reflective and refractive elements, applications as head-mounted displays (HMDs) are also designed [3]. Scheimpflug systems realized large shift of object distance using the asymmetric imaging condition [4]. Since the manufacturing technology nowadays allows the use of freeform surfaces, in those non-rotationally symmetric systems mentioned above, freeform surfaces are widely used to compensate the asymmetric effect and improve the system

performance in the past 20 years. However, due to the limitation of the most frequently used optimization algorithms such as Damped Least Squares (DLS), it is more complicated when dealing with freeform surfaces. On the one hand, the large number of degrees of freedom provide possibilities to achieve good performance. On the other hand, the performance of the starting point, the selection of surface representation, the selection of surface position, and the optimization steps will influence the final result. Many details should also be considered, such as the manufacturability controlling during the design procedure and the optimization steps when increasing the number of variables by adding more polynomials to the surface. The analysis of system performance and aberrations are also quite different from the traditional designs. There are so far no general rules of designing a non-rotationally symmetric system with freeform surfaces. Therefore, the main objective of this thesis is to solve some problems for the system design without rotational symmetry, which are methods to obtain a good initial system, analysis of aberrations in the systems, and the position selection rules to locate aspheres and freeform surfaces. The methods and techniques are applied in some typical non-rotationally symmetric applications.

Similarly to traditional systems, the analysis and the optimization of system performance rely on ray tracing and aberration theory. Based on the aberration theory, the designers decide how to deal with the system. Therefore, our work is mainly based on vectorial aberration theory.

Chapter 2 opens a brief introduction of already existing initial system design methods and their limitations to be improved. Since our work is mainly based on aberration theory, the traditional Seidel aberration theory for centered systems and the extension to Nodal Aberration Theory (NAT) for the off-axis systems are briefly introduced. In non-rotationally symmetric systems, aspheres and freeform surfaces are often used. Thus, the most frequently used representations and their properties of the aspherical and freeform surfaces are also shortly introduced. Additionally, the traditional design process and the problems of non-rotationally symmetric systems are discussed.

In Chapter 3, the vectorial aberration theory is explained in detail, based on which the design strategies can be proposed. When the system reference changes from

paraxial to paraboloidal, the aberration distribution over the FOV is no longer rotationally symmetric, which can be represented in a vectorial formulation. The systematic initial design procedure based on confocal conic surfaces is introduced in this chapter. The techniques to avoid obscuration are also discussed. We also propose a new initial system design method based on Gaussian brackets and NAT, which overcomes the limitation of the number of surfaces, and the limitation of refractive or reflective type. Based on NAT, the paraxial environment is extended to the paraboloidal environment. Therefore, this method can deal with rotationally symmetric, plane-symmetric, and general non-rotationally symmetric systems. In this chapter, the system geometry to minimize the aberrations and the surface selection rules are also generated based on the understanding of aberration contribution in the system. Therefore, the primary aberration coefficients, the contribution of the aspherical part and freeform parts based on vectorial representations are studied. Since biconic surfaces become the beneficial choice for the basic surface shape, the aberrations of the biconic surface are also derived.

Three typical applications without rotational symmetry are demonstrated in Chapter 4. The unobscured TMA system is the most often seen plane-symmetric reflective system. The Yolo telescope system shows a complete loss of symmetry. Scheimpflug systems do not belong to the off-axis systems. Instead, it is a special kind of non-rotationally symmetric system with a variant magnification along the field, which leads to non-rotationally symmetric imaging condition in the FOV. It is shown how the initial setups of the three kinds of systems can be designed based on the Gaussian brackets method. The aberration behavior of off-axis systems is analyzed to decide the tilt angles, which vanish the aberrations of the central field. For TMA systems and Yolo systems, since the number of surfaces is small, all the surfaces are often added with aspheres and freeform surfaces. But the Scheimpflug system consists of more surfaces. Thus the position selection should be made for the freeform surface location. The surface positions are analyzed based on vectorial aberration theory, which gives a hint which aberrations would be influenced at a certain position. The surfaces are selected based on the rules that are generated.

Finally, the conclusions and outlooks are drawn in Chapter 5.

2 State of the art

2.1 Initial system design methods

For general system design, the starting point is important for the following optimization procedure. In traditional system design, a good starting point provides the possibility to achieve the system performance by only a small number of iterations of the structural modification or material replacement. For an optical design with freeform surfaces, the starting point influences the number and complexity of freeform surfaces, which correspond to the cost and difficulty in fabrication. Therefore, it is important to find an initial system, which has minimum aberrations before the optimization procedure.

In traditional system design, the initial system can be selected from an already existing system. The paraxial properties of the selected existing system are similar or the same as the specifications of the design. Therefore, the final design can be achieved after certain iterations of structural change and optimization. For this method, the designer should have enough experience in system design and certain database of existing designs, such as patents [5].

Another option of conventional methods is to begin with a thin-lens model [6]. This method works fine with even complicated systems such as zoom systems. With this method, the focal power of each group of components is represented by one thin lens. The paraxial properties, such as focal length, numerical aperture, and zoom factor, are fulfilled with the thin-lens model. By substituting the thin components by real lenses and further changing the bending or splitting the lenses, the final system performance can be achieved. For instance, the zoom system consists of an afocal system in front of the camera lens. The afocal system has three groups of components. The front and rear groups have positive focal power, and the middle group is negative. The system has variant focal length by moving the middle group. Therefore the afocal system can be initially designed with the thin lens model as in Figure 2-1.

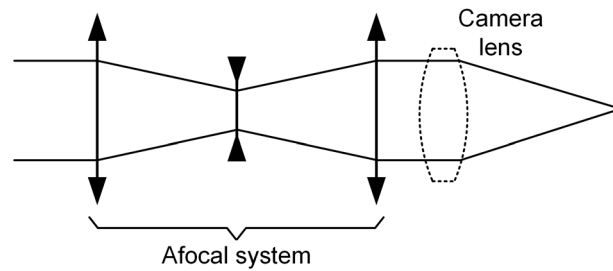


Figure 2-1 Thin lens model of zoom system [6]

The manufacturing technique nowadays allows the possibility to use freeform surfaces in the systems. Therefore, the system can be extended to an off-axis structure. The design process of off-axis systems differs from centered systems due to the complicated aberrations and geometric behavior. Therefore, certain methods are proposed to find a good starting point before adding the freeform surfaces. One method is to use confocal conic sections [7]. Reflective conic surfaces are also named Cartesian surfaces [8]. Rays starting from one geometric focal point will be perfectly imaged to the other focal point, which provides the possibility to have one field perfectly imaged. Therefore, it means that the nodal point can be obtained in the FOV of an off-axis system. However, problems appear when adding freeform surfaces to the system because of the large off-axis use of the conic sections. The design procedure of the conic-confocal method will be introduced in our work. We formulate the general rules and steps to obtain the on-axis model and tilt the surfaces at the confocal points, the relations between the angles to obtain linear astigmatism free, and the technique to check the obscuration condition.

The Simultaneous Multiple Surface (SMS) method differs from the methods mentioned above since it is used to design the initial system directly with freeform surfaces instead of the basic shapes such as spherical surfaces or conic sections. In the case of finite FOV, the SMS method allows coupling of the chosen rays from a certain number of fields into image points by using a certain number of freeform surfaces [9]. In recent years, it is a hot topic to extend the SMS method concerning the number of freeform surfaces and the number of selected fields. Therefore, the limitation of this method is the number of surfaces and the number of fields.

To overcome the shortcomings of the existing methods, we have developed a method based on NAT and Gaussian brackets to design the initial system [10]. Gaussian brackets defined by Tanaka was used to design centered system based on Seidel aberration theory. NAT can bring the system from on-axis environment to paraxial environment. Therefore, the new method can deal with both refractive and reflective systems. The number of surfaces is not limited. The method works for centered systems, off-axis systems and also special asymmetric imaging systems such as Scheimpflug systems.

2.2 Traditional aberration theory

In real optical imaging applications, it is impossible to achieve a perfect image, which is due to the aberrations generated by each component in the system. In ideal optical systems, all rays starting from one object point are supposed to be imaged to an ideal image point on the Gaussian image plane. In real imaging systems, the displacement of rays from the ideal image point along the image plane is called transverse aberration, while the displacement along the optical axis is called longitudinal aberration. Since the rays are always perpendicular to the wavefront, the deformation of the wavefront and the transverse aberration of the rays are equivalent. The wavefront deformation is called wave aberration [11]. The relation of those three descriptions of aberrations is illustrated in Figure 2-2.

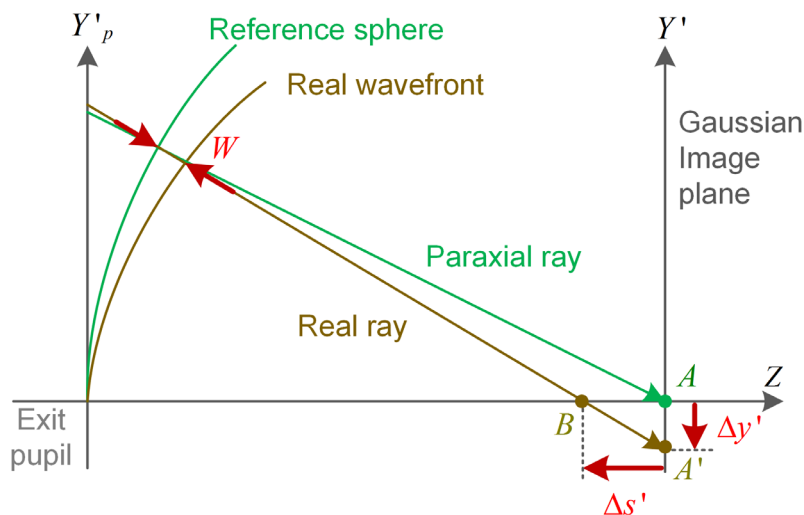


Figure 2-2 Relation of different aberration description [11]

As shown in Figure 2-2, the wave aberration is the difference between the real wavefront and the reference sphere at the exit pupil, which is represented as W .

The ideal image is located at point A, however, due to deformation of the wavefront, the intersection point of the real ray with the image plane locates at point A'. The transverse aberration shown as $\Delta y'$ is the deviation from A to A' along the image plane. The real ray intersects with the optical axis at point B. Hence the displacement $\Delta s'$ measured along the optical axis from A to B is the longitudinal aberration.

The traditional aberration theory was developed for rotationally symmetric systems. Therefore it is sufficient to use two rays, which are the marginal ray (MR) and the chief ray (CR) of the largest field as seen in Figure 2-3, to represent the whole paraxial ray tracing in the system. Normally, the two paraxial rays are selected in the tangential (meridional) plane of the system.

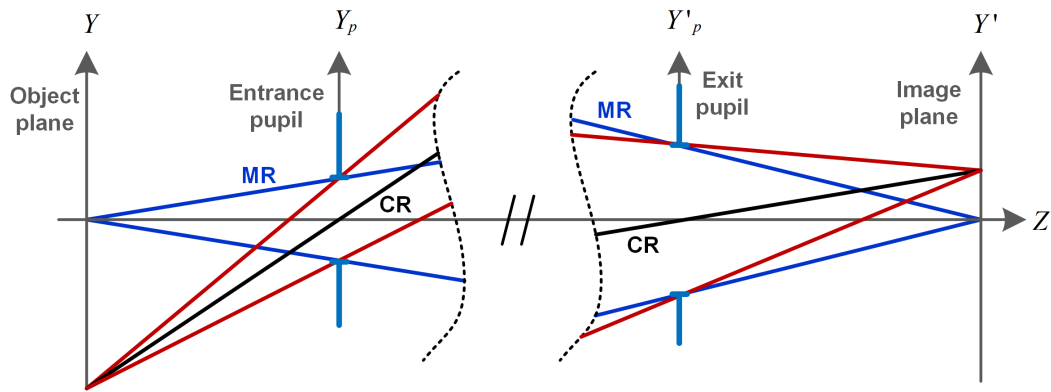


Figure 2-3 Marginal ray and chief ray in an off-axis field in the optical system.

The traditional aberration theory is called Seidel aberration theory that is named after Ludwig von Seidel, who first gave the third order aberrations systematically in 1856 [12]. The five Seidel aberrations are named spherical aberration, coma, astigmatism, field curvature and distortion. When the aberrations are represented by transverse aberration, they are of the third order. The relation between the wave aberration and the transverse aberration is given as [11, 13, 14]

$$\Delta x' = -\frac{R_{ref}}{n} \frac{\partial W(x_p, y_p)}{\partial x_p}, \quad (2-1)$$

$$\Delta y' = -\frac{R_{ref}}{n} \frac{\partial W(x_p, y_p)}{\partial y_p}, \quad (2-2)$$

where $\Delta x'$ and $\Delta y'$ denote the transverse aberration in x and y coordinates. R_{ref} denotes the radius of the reference sphere. x_p and y_p are the pupil coordinates in x- and y-axis. n is the refractive index in the image space. Therefore, it can be

seen that wave aberration is one order higher than transverse aberration. Therefore, the five monochromatic primary aberrations regarding wave aberration are of the fourth order.

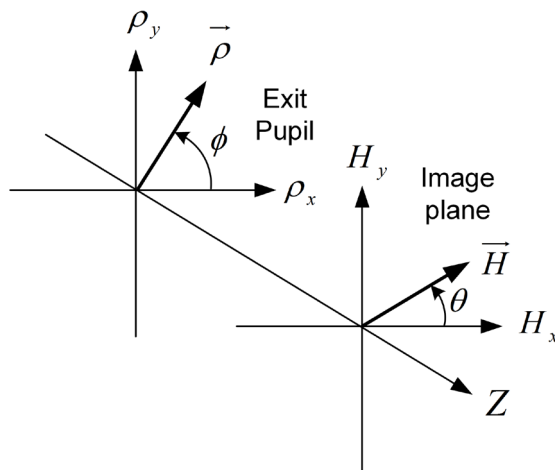


Figure 2-4 Polar coordinate of pupil and field height

In this thesis, we unify the polar coordinate of the field coordinate and the pupil coordinate and illustrate them in Figure 2-4. Different from some of the literature, where the azimuthal angle is defined as the angle from the y-axis to the field vector or the pupil vector, we define the azimuthal angle as the angle from the x-axis to the field vector or the pupil vector. In this case, the definition of the coordinate matches the polar coordinate definition for some of the freeform surface representations such as Zernike fringe polynomials. As mentioned, the aberrations in the system can be decomposed into aberration contribution of each surface. Additionally, the aberrations generated by each surface can be further decomposed into the aberrations generated by different parts of the surface sag. Therefore, it makes sense to unify the coordinates.

In rotationally symmetric systems with spherical surfaces, the wave aberration is expanded in a Taylor power series regarding the aperture and field as [12-15]

$$W = \sum_j \sum_p \sum_n \sum_m (W_{klm})_j H^k \rho^l \sin^m \phi, \quad \begin{matrix} k = 2p + m \\ l = 2n + m \end{matrix}, \quad (2-3)$$

where H denotes the normalized field height (actual field height divided by the largest field height), ρ denotes the normalized radial aperture height in the pupil coordinate, and ϕ denotes the azimuthal angle of the pupil coordinate. W_{klm} denotes the aberration coefficients. The coefficients of the primary aberrations of the j^{th} surface in the system are listed in Table 2-1. The aberration coefficients

$S_I \sim S_V$ are the five Seidel coefficients [12-15]. The total wavefront aberration is written as the sum of contributions of each surface in the system. The coefficients W_{klm} can be calculated using the paraxial ray trace data. u_j denotes the marginal ray angle, \bar{u}_j denotes the chief ray angle, h_j denotes the marginal ray height, and \bar{h}_j denotes the chief ray height. n_j is the refractive index.

The parameters A_j and \bar{A}_j are defined as

$$A_j = n_j (h_j c_j + u_j), \quad (2-4)$$

$$\bar{A}_j = n_j (\bar{h}_j c_j + \bar{u}_j). \quad (2-5)$$

The Lagrange invariant is given as

$$H_{Lag j} = n_j (\bar{h}_j u_j - h_j \bar{u}_j). \quad (2-6)$$

Table 2-1 Calculation of primary monochromatic aberration coefficients

Aberrations	Coefficients
Spherical aberration	$W_{040j} = \frac{1}{8} S_{Ij} = -\frac{1}{8} A_j^2 h_j \left(\frac{u'_j}{n_j} - \frac{u_j}{n_{j-1}} \right)$
Coma	$W_{131j} = \frac{1}{2} S_{IIj} = -\frac{1}{2} \bar{A}_j A_j h_j \left(\frac{u'_j}{n_j} - \frac{u_j}{n_{j-1}} \right)$
Astigmatism	$W_{222j} = \frac{1}{2} S_{IIIj} = -\frac{1}{2} A_j^2 h_j \left(\frac{u'_j}{n_j} - \frac{u_j}{n_{j-1}} \right)$
Field curvature	$W_{220j} = \frac{1}{4} S_{IVj} = -\frac{1}{4} H_{Lag j}^2 c_j \left(\frac{1}{n_j} - \frac{1}{n_{j-1}} \right)$
Distortion	$W_{311j} = \frac{1}{2} S_{Vj} = -\frac{1}{2} \left[\begin{array}{l} -\bar{A}_j^3 h_j \left(\frac{1}{n_j^2} - \frac{1}{n_{j-1}^2} \right) \\ + \bar{h}_j \bar{A}_j (2h_j \bar{A}_j - \bar{h}_j A_j) c_j \left(\frac{1}{n_j} - \frac{1}{n_{j-1}} \right) \end{array} \right]$

The wave aberrations discussed above only concern monochromatic aberrations. For refractive systems, the index of refraction depends on the wavelength. Therefore, the focal power of the system varies for different wavelength, which causes chromatic aberrations. Concerning chromatic change of aberrations, the most significant changes are the chromatic change of magnification and defocus. Chromatic aberration can be described by transverse chromatic aberration and longitudinal chromatic aberration corresponding to the chromatic change of magnification and the chromatic change of defocus, which are illustrated in Figure 2-5. The variation of focal length with wavelength is called the longitudinal chromatic

aberration shown as the difference $\Delta s'_{long}$ between blue and red wavelengths as an example. Since the transverse chromatic aberration is the change of magnification with the wavelength and the image height depends on the chief ray, the transverse aberration is illustrated as the difference $\Delta y'_{trans}$ between the chief ray heights of blue and red wavelengths in the Gaussian image plane [11, 14].

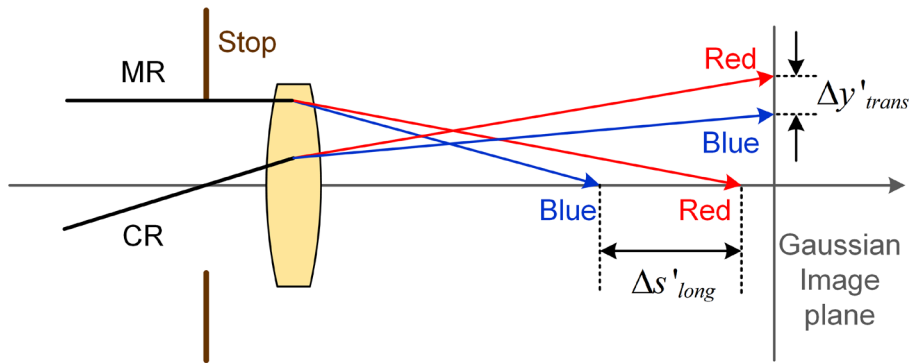


Figure 2-5 Longitudinal and transverse chromatic aberrations of blue and red wavelengths.

Chromatic aberration is the second-order property of the wavefront deformation. Thus, the second order change in wavefront with wavelength is given as [14]

$$\partial_{\lambda}W = \partial_{\lambda}W_{000} + \partial_{\lambda}W_{200}H^2 + \partial_{\lambda}W_{111}H\rho\sin\phi + \partial_{\lambda}W_{020}\rho^2. \quad (2-7)$$

The terms and the corresponding types of aberrations are listed in Table 2-2.

Table 2-2 Chromatic aberration terms

Term	Aberration
$\partial_{\lambda}W_{000}$ and $\partial_{\lambda}W_{200}$	Chromatic changes of piston
$\partial_{\lambda}W_{020}$	Chromatic change of focus
$\partial_{\lambda}W_{111}$	Chromatic change of magnification

The calculation of the two chromatic aberration coefficients are listed in Table 2-3. The two coefficients are also calculated based on the paraxial ray trace data of the chief ray and the marginal ray. They are also named as C_I and C_{II} in some literature and shown with the five monochromatic Seidel coefficients $S_I \sim S_V$ in bar diagrams for the analysis of aberrations in rotationally symmetric systems [11-14].

The aberration coefficients in Table 2-1 and Table 2-3 are derived for the j^{th} surface in the optical system. The total aberration can be calculated as the sum of the contribution of each surface.

Table 2-3 Calculation of the primary chromatic aberration coefficients

Aberration	Coefficient
Transverse chromatic aberration	$\partial_\lambda W_{111j} = C_{IIj} = \bar{A}_j h_j \Delta \left(\frac{\partial n_j}{n_j} \right)$
Longitudinal chromatic aberration	$\partial_\lambda W_{020j} = \frac{1}{2} C_{Ij} = \frac{1}{2} A_j h_j \Delta \left(\frac{\partial n_j}{n_j} \right)$

2.3 Nodal Aberration Theory

When optical systems are without rotational symmetry, such as plane-symmetric, double plane-symmetric, or non-symmetric systems, the traditional aberration theory (Seidel aberration theory) is not valid, because the rays in the tangential (meridional) plane cannot represent all the rays in the system. Therefore, to extend the aberration theory to non-rotationally symmetric systems, the wave aberration function is extended based on the field and aperture vectors [14-16]. R. V. Shack wrote the aberration function in the vectorial form as

$$W(\vec{H}, \vec{\rho}) = \sum_j \sum_p \sum_n \sum_m (W_{klm})_j (\vec{H} \cdot \vec{H})^p (\vec{\rho} \cdot \vec{\rho})^n (\vec{H} \cdot \vec{\rho})^m. \quad (2-8)$$

As shown in Figure 2-4, the normalized field vector in the image plane is given as

$$\vec{H} = H e^{i\theta}. \quad (2-9)$$

Therefore, the two components of the field vector in x- and y-axis are given as

$$\begin{cases} H_x = H \cos \theta \\ H_y = H \sin \theta \end{cases} \quad (2-10)$$

Similarly, the normalized pupil vector and the two components in x- and y-axis are given as

$$\vec{\rho} = \rho e^{i\phi}, \quad (2-11)$$

$$\begin{cases} \rho_x = \rho \cos \phi \\ \rho_y = \rho \sin \phi \end{cases} \quad (2-12)$$

The vectorial relations are as

$$\vec{H} \cdot \vec{H} = H^2 \cos(\theta - \theta) = H^2, \quad (2-13)$$

$$\vec{\rho} \cdot \vec{\rho} = \rho^2 \cos(\phi - \phi) = \rho^2, \quad (2-14)$$

$$\vec{H} \cdot \vec{\rho} = H \rho \cos(\theta - \phi). \quad (2-15)$$

Therefore, in rotationally symmetric systems, where the field height is represented by the fields along the y -axis, which means $\theta = \pi/2$, the vectorial wave aberration representation as in Eq. (2-8) can be written in the form of Eq. (2-3).

In non-rotationally symmetric systems, there is one group called tilted component systems (TCS), which means the components in the system are tilted or decentered while each of them is individually axially symmetric. For a system consisting of only spherical surfaces, if the surface is tilted or decentered, it can be seen as a total tilted effect, because the vertex of a spherical surface can be an arbitrary point on the surface. As shown in Figure 2-6, the spherical surface is decentered along y -direction with a distance of δv and tilted with an angle of β . Thus, the center of curvature O is decentered to O' with a displacement of δo in paraxial approximation. The original vertex v_0 moves to v . The local axis 1 is along the new vertex v and the new center of curvature O' . If the new vertex of the surface is assumed to be v^* , which locates on the reference axis, the equivalent local axis becomes local axis 2. Then the decentering and tilt effects can be seen as an equivalent tilt effect. The tilt parameter is given as [15]

$$\beta_0 = \beta + c\delta v = c\delta o. \quad (2-16)$$

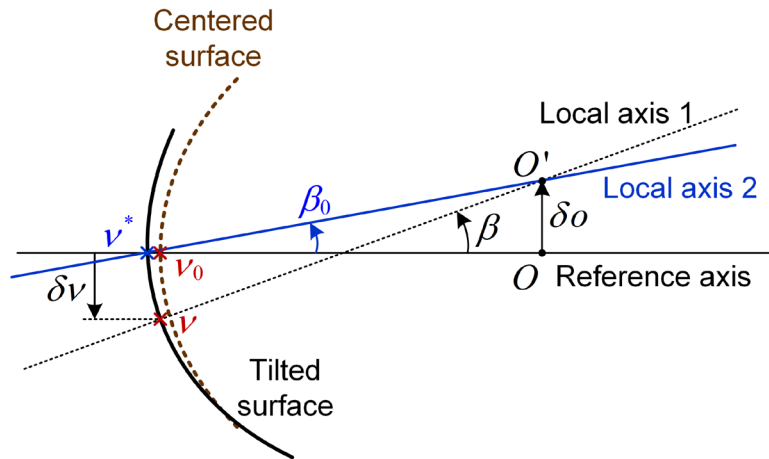


Figure 2-6 Equivalent local axis and tilt parameter of a spherical surface. [15]

Therefore, every decentered or tilted surface can be treated as a tilted surface. The tilt effect leads to a displacement of the normalized field vector, which is defined as $\bar{\sigma}$. Therefore, the wave aberration for tilted component systems are given as [15]

$$W(\vec{H}, \vec{\rho}) = \sum_j \sum_p \sum_n \sum_m (W_{klm})_j [(\vec{H} - \vec{\sigma}_j) \cdot (\vec{H} - \vec{\sigma}_j)]^p (\vec{\rho} \cdot \vec{\rho})^n [(\vec{H} - \vec{\sigma}_j) \cdot \vec{\rho}]^m, \quad (2-17)$$

in which, $k = 2j + m$ and $l = 2n + m$. The wave aberration expansion of the fourth order is written as

$$\begin{aligned} W = & \sum_j W_{040j} (\vec{\rho} \cdot \vec{\rho})^2 + \sum_j W_{131j} [(\vec{H} - \vec{\sigma}_j) \cdot \vec{\rho}] (\vec{\rho} \cdot \vec{\rho}) \\ & + \sum_j W_{222j} [(\vec{H} - \vec{\sigma}_j) \cdot \vec{\rho}]^2 \\ & + \sum_j W_{220j} [(\vec{H} - \vec{\sigma}_j) \cdot (\vec{H} - \vec{\sigma}_j)] (\vec{\rho} \cdot \vec{\rho}) \\ & + \sum_j W_{311j} [(\vec{H} - \vec{\sigma}_j) \cdot (\vec{H} - \vec{\sigma}_j)] [(\vec{H} - \vec{\sigma}_j) \cdot \vec{\rho}]. \end{aligned} \quad (2-18)$$

Therefore, the effective normalized field height defined as $\vec{H}_{Aj} = \vec{H} - \vec{\sigma}_j$ for the j^{th} surface is shown as in Figure 2-7.

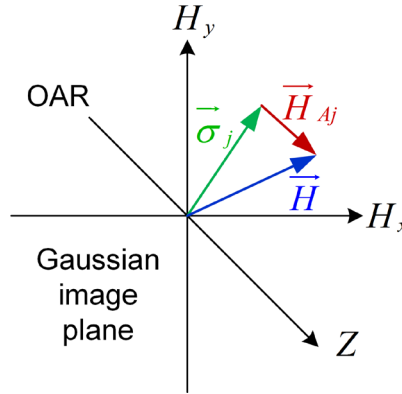


Figure 2-7 The effective field height and the field shift vector of a surface [15]

The field shift vector can be calculated using the real ray tracing data of the optical axis ray (OAR). The definition of the OAR is the ray passing through the center of the object plane, the center of the image plane, and the center of pupils for all the surfaces in the system. Hence, the OAR is the chief ray of the central field in an off-axis system. When all the surfaces are centered, the OAR passes along the optical axis through the vertex of each surface. The incident angle of the OAR is always zero. When the surface is tilted, the OAR has a certain incident angle on the surface. The field shift vector $\vec{\sigma}$ can be derived using the OAR incident angle \vec{i}_j^* and the paraxial ray trace data of the largest chief ray. When the surface is tilted in both x- and y-direction, the OAR incident angle is represented as a vector. For the off-axis system, the paraxial ray trace is considered as in the centered case. When making paraxial ray trace, it is assumed that all the tilted or

decentered surfaces are centered on the common optical axis. The field shift vector is given as [15-17]

$$\vec{\sigma}_j = -\frac{\vec{i}_j^*}{\bar{h}_j c_j + u_j}. \quad (2-19)$$

The calculation of the field shift vector is real-ray based. The ray direction cosine data of the OAR is obtained in the local coordinate of the object plane of each surface, which corresponds to the object plane and its conjugates in the system.

The three normal vectors, which are used to calculate the field shift vector, are illustrated in Figure 2-8. The system is assumed as centered when performing paraxial ray trace. All the surfaces and pupils are centered on the optical axis as in Figure 2-8(a). The paraxial ray trace data of the marginal ray and the chief ray of the largest field is also used to calculate the Seidel aberration coefficients as in Table 2-1. In Figure 2-8(b), the surface is decentered and tilted from the optical axis. The local coordinate is defined in the object plane. Hence the normal vector of the object plane is defined as \vec{N} , which is normalized. The original vertex v of the surface is decentered from the optical axis. The normalized direction vector of the OAR is defined as \vec{R} . As mentioned above, the vertex can be an arbitrary point on the spherical surface. Thus the intersection point of the OAR with the surface is defined as the new vertex of the tilted surface. The axis of the surface is along the center of curvature O' and the new vertex v^* . The normal vector \vec{S} with length of 1 at the OAR intersection point is along the axis of the surface. The direction cosines along the z-axis of the three unit vectors \vec{R} , \vec{S} , and \vec{N} are always defined as negative. Therefore, the direction cosines of the vectors in the local coordinate of the j^{th} surface are given as [10, 17]

$$\vec{R}_j = (0, 0, -1), \quad (2-20)$$

$$\vec{S}_j = (SRL_j, SRM_j, SRN_j), \quad (2-21)$$

$$\vec{N}_j = (0, 0, -1). \quad (2-22)$$

Therefore, the value of the field shift vector is calculated as

$$\vec{\sigma}_j = \frac{[\vec{N}_j \times (\vec{R}_j \times \vec{S}_j)]}{\bar{u}_j + \bar{h}_j c_j} = \begin{pmatrix} -\frac{SRL_j}{\bar{u}_j + \bar{h}_j c_j} \\ SRM_j \\ -\frac{SRN_j}{\bar{u}_j + \bar{h}_j c_j} \end{pmatrix}. \quad (2-23)$$

The Seidel aberration coefficients $(W_{klm})_j$ and the field shift vector $\vec{\sigma}_j$ can be obtained by tracing the paraxial chief ray, the paraxial marginal ray, and the real OAR. The primary aberrations of a system with off-axis spherical surfaces can be derived using Eq.(2-18) and Eq.(2-23).

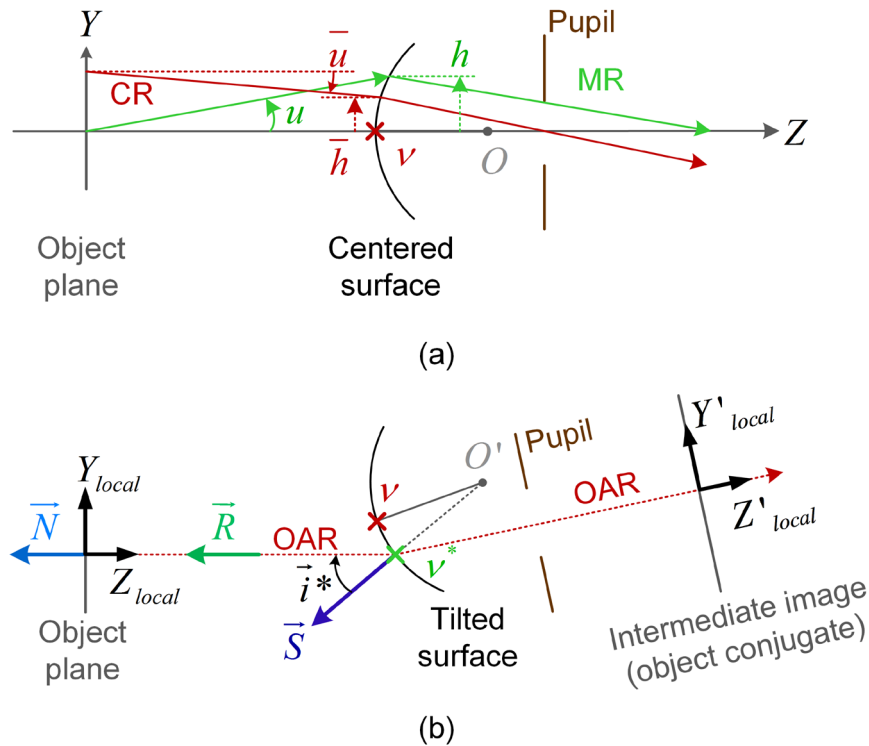


Figure 2-8 Real-ray-based calculation of the field shift vector. (a) Centered surface for paraxial ray trace (b) tilted surface for real OAR trace.

2.4 Gaussian brackets and Generalized Gaussian Constants

In Section 2.2 and 2.3, it is mentioned that the Seidel aberration coefficients are calculated based on paraxial ray trace data. It is well known that ray transfer matrix (also known as ABCD matrix) is used for ray tracing in paraxial approximation [11, 18]. Thus, Gaussian brackets and the Generalized Gaussian Constants (GGC's) are used to perform paraxial ray tracing based on a matrix method [19-22]. Instead of the individual matrix for each element, it is always written as one total 4x4 matrix, which consists four elements called GGC's. Each Generalized Gaussian Constant is defined as a Gaussian bracket.

As a generalization of the ideas and theories of Herzberger [19-21], the description of Gaussian brackets is defined by Tanaka based on the theory of continued

fractions [22]. A Gaussian bracket, whose elements consist of a set of numbers or functions, $a_i, a_{i+1}, a_{i+2}, \dots, a_{j-1}, a_j$, is written in the form as

$${}^i G_j = [a_i, a_{i+1}, a_{i+2}, \dots, a_{j-1}, a_j]. \quad (2-24)$$

The expression in a recurrent form is given as

$${}^i G_j = \begin{cases} {}^i G_{j-1} a_j + {}^i G_{j-2}, & i \leq j, \\ 1, & i = j+1, \\ 0, & i = j+2. \end{cases} \quad (2-25)$$

If the bracket is empty, it corresponds to the second line in Eq. (2-25). If there are plural elements, the Gaussian bracket is defined as the first line. For instance, when the Gaussian bracket consists of four elements, ${}^i G_{i+3}$, it is obtained as

$$\begin{aligned} {}^i G_{i-2} &= 0, \\ {}^i G_{i-1} &= 1, \\ {}^i G_i &= a_i, \\ {}^i G_{i+1} &= a_i a_{i+1} + 1, \\ {}^i G_{i+2} &= a_i a_{i+1} a_{i+2} + a_i + a_{i+2}, \\ {}^i G_{i+3} &= a_i a_{i+1} a_{i+2} a_{i+3} + a_i a_{i+1} + a_i a_{i+3} + a_{i+2} a_{i+3} + 1. \end{aligned} \quad (2-26)$$

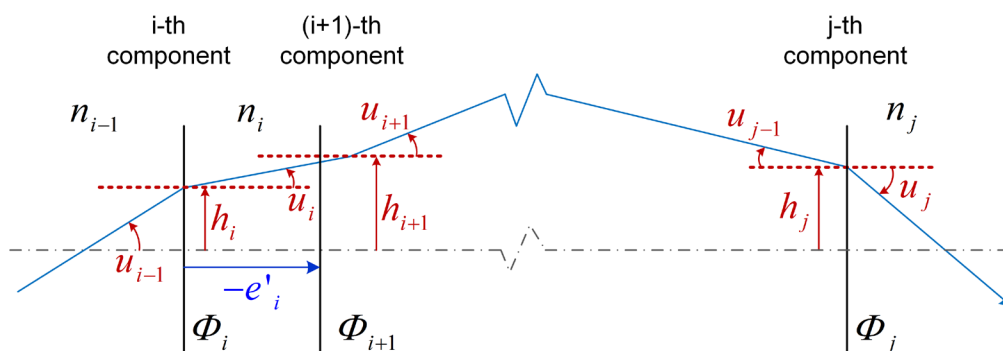


Figure 2-9 Ray path from the i^{th} component to the j^{th} component.

In an optical system as shown in Figure 2-9, the power of each component is defined as Φ_i and the reduced distance is named e'_i between the i^{th} and the $(i+1)^{\text{th}}$ components. The component here means a surface in a thick lens system or a lens in a thin lens system. The powers and the negative reduced distances are arranged in a series as

$$\Phi_1, -e'_1, \Phi_2, -e'_2, \dots, -e'_{k-1}, \Phi_k, -e'_k, \Phi_{k+1}, \dots. \quad (2-27)$$

For systems consisting of only spherical surfaces, the power and the reduced distance are given as

$$\Phi_i = (n_{i-1} - n_i) c_i, \quad (2-28)$$

$$e'_i = -\frac{d_i}{n_i}, \quad (2-29)$$

where c_i is the curvature of the i^{th} surface; n_{i-1} is the refractive index before the i^{th} surface; n_i is the refractive index after the i^{th} surface; d_i is the distance from the i^{th} surface to the $(i+1)^{\text{th}}$ surface.

Based on the definition of Gaussian brackets, GGC's for the subsystem from the i^{th} surface to the j^{th} surface are defined as

$${}^i A_j = [\Phi_i, -e'_i, \Phi_{i+1}, -e'_{i+1}, \dots, -e'_{j-1}], \quad {}^i A_i = 1, \quad (2-30)$$

$${}^i B_j = [-e'_i, \Phi_{i+1}, -e'_{i+1}, \dots, -e'_{j-1}], \quad {}^i B_i = 0, \quad (2-31)$$

$${}^i C_j = [\Phi_i, -e'_i, \Phi_{i+1}, -e'_{i+1}, \dots, -e'_{j-1}, \Phi_j], \quad {}^i C_i = \Phi_i, \quad (2-32)$$

$${}^i D_j = [-e'_i, \Phi_{i+1}, -e'_{i+1}, \dots, -e'_{j-1}, \Phi_j], \quad {}^i D_i = 1. \quad (2-33)$$

The relations between the four GGC's are given as

$${}^i A_j = \begin{cases} -{}^i C_{j-1} e'_{j-1} + {}^i A_{j-1}, & i < j, \\ 1, & i = j, \end{cases} \quad (2-34)$$

$${}^i C_j = \begin{cases} {}^i A_j \Phi_j + {}^i C_{j-1}, & i \leq j, \\ 0, & i = j+1, \end{cases} \quad (2-35)$$

$${}^i B_j = \begin{cases} -{}^i D_{j-1} e'_{j-1} + {}^i B_{j-1}, & i < j, \\ 0, & i = j, \end{cases} \quad (2-36)$$

$${}^i D_j = \begin{cases} {}^i B_j \Phi_j + {}^i D_{j-1}, & i < j, \\ 1, & i = j. \end{cases} \quad (2-37)$$

In paraxial approximation, the ray refraction or reflection at the i^{th} surface with the power of Φ_i is given as a matrix transfer as

$$\begin{pmatrix} h_i \\ n_i u'_i \end{pmatrix} = \begin{pmatrix} 1 & 0 \\ \Phi_i & 1 \end{pmatrix} \begin{pmatrix} h_i \\ n_{i-1} u_i \end{pmatrix}. \quad (2-38)$$

Different from the matrix definition of the thin lens, the power in Eq. (2-28) and Eq. (2-38) is derived according to the law of refraction of a single surface. If the component is considered as a thin lens in air, the power is given by the negative value of the focal power as $\Phi_i = -1/f'$.

The paraxial ray transfer from the i^{th} surface to the $(i+1)^{\text{th}}$ surface with the reduced distance of e'_i is written as

$$\begin{pmatrix} h_{i+1} \\ n_i u_{i+1} \end{pmatrix} = \begin{pmatrix} 1 & -e'_i \\ 0 & 1 \end{pmatrix} \begin{pmatrix} h_i \\ n_i u_{i+1} \end{pmatrix}. \quad (2-39)$$

By applying Eqs. (2-38) and (2-39) in the sequence, in which the ray passes through, and arranging the product by using the associated properties of the matrix, the paraxial ray trace from the i^{th} surface to the j^{th} surface can be obtained as the following four relations.

$$\begin{pmatrix} h_j \\ n_j u'_j \end{pmatrix} = \begin{pmatrix} {}^i A_j & {}^i B_j \\ {}^i C_j & {}^i D_j \end{pmatrix} \begin{pmatrix} h_i \\ n_{i-1} u_i \end{pmatrix}, \quad (2-40)$$

$$\begin{pmatrix} h_j \\ n_{j-1} u_j \end{pmatrix} = \begin{pmatrix} {}^i A_j & {}^i B_j \\ {}^i C_{j-1} & {}^i D_{j-1} \end{pmatrix} \begin{pmatrix} h_i \\ n_{i-1} u_i \end{pmatrix}, \quad (2-41)$$

$$\begin{pmatrix} h_j \\ n_j u'_j \end{pmatrix} = \begin{pmatrix} {}^{i+1} A_j & {}^i B_j \\ {}^{i+1} C_j & {}^i D_j \end{pmatrix} \begin{pmatrix} h_i \\ n_i u'_i \end{pmatrix}, \quad (2-42)$$

$$\begin{pmatrix} h_j \\ n_{j-1} u_j \end{pmatrix} = \begin{pmatrix} {}^{i+1} A_j & {}^i B_j \\ {}^{i+1} C_{j-1} & {}^i D_{j-1} \end{pmatrix} \begin{pmatrix} h_i \\ n_i u'_i \end{pmatrix}. \quad (2-43)$$

The paraxial properties of the system can also be derived using the GGC's. If the system consists of k surfaces, the back focal length from the k^{th} surface to the rear focal plane is given by

$$S'_F = \frac{{}^1 A_k}{{}^1 C_k}. \quad (2-44)$$

The focal length in the image space from the rear principal plane to the rear focal plane is given by

$$f' = \frac{1}{{}^1 C_k}. \quad (2-45)$$

2.5 Aspheres

To allow more degrees of freedom in improving the system performance, aspherical devices are used, which deviate from a spherical shape but are still rotationally symmetric.

Reflective surfaces with the shape of a conic section have special properties to focus certain bundles of rays without any geometric error [6, 8, 11]. A conic section, as a special aspherical shape, can be characterized by the following analytical representation as

$$z_{conic} = \frac{c(x^2 + y^2)}{1 + \sqrt{1 - (1 + \kappa)c^2(x^2 + y^2)}}, \quad (2-46)$$

where c denotes the surface curvature, and κ denotes the conic parameter. Different shapes corresponding to different values of the conic parameter are shown in Table 2-4.

Table 2-4 Shape of the conic sections as a function of the parameter [6, 11]

Shape of surface	Conic parameter
Paraboloid	$\kappa = -1$
Hyperboloid	$\kappa < -1$
Sphere	$\kappa = 0$
Oblate ellipsoid	$\kappa > 0$
Prolate ellipsoid	$-1 < \kappa < 0$

In Eq. (2-46), the surface is represented in Cartesian coordinates. If the aperture coordinate of the surface is converted into a polar coordinate, the coordinates x and y can be written as a vector $\vec{r} = (x, y)$, which is called the aperture vector of the surface. The two components of the aperture vector are given as

$$\begin{cases} x = r \cos \phi \\ y = r \sin \phi \end{cases} \quad (2-47)$$

where r denotes the radial coordinate, and ϕ denotes the angular coordinate, which corresponds to the azimuthal angle of the pupil coordinate in Figure 2-4. The coordinate of the surface aperture is illustrated as in Figure 2-10.

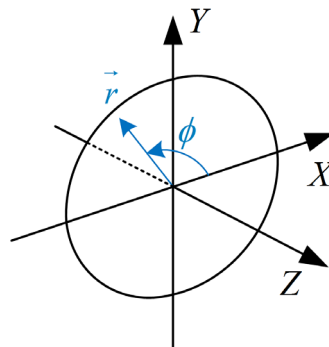


Figure 2-10 Polar coordinate of the surface aperture

Based on the conic surface shape, it is possible to add higher order aspherical deformation on the surface shape. The deviation from the conic shape can be represented as a set of polynomials. The traditional aspherical shape is characterized by Taylor expansion. The general aspherical surface with even orders is characterized by a conic shape as the basic shape and a series of polynomials. The representation in the polar coordinate of an even asphere is given as

$$z_{\text{even asphere}} = \frac{cr^2}{1 + \sqrt{1 - (1 + \kappa)c^2r^2}} + \sum_{m=0}^M a_{2m+4} r^{2m+4}, \quad (2-48)$$

where a_{2m+4} denotes the coefficients of the polynomials and m is the number of the polynomial. Therefore, the polynomials are added as a deviation in the z -direction. The deviation from the spherical shape can be illustrated as in Figure 2-11.

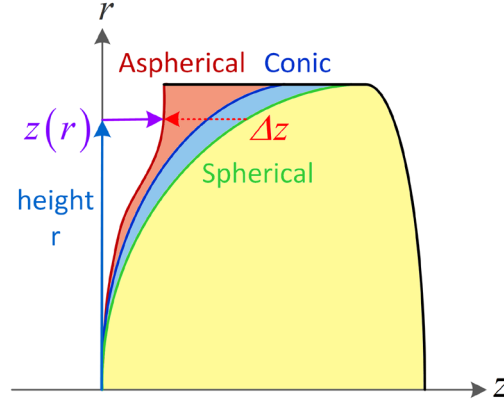


Figure 2-11 Aspherical surface

In Figure 2-11, r denotes the radial height of the aperture. Hence, the surface sag corresponding to the radial height is $z(r)$. The deviation from the spherical surface is shown as Δz .

The deviation of the aspherical surface from the conic shape can be characterized not only by Taylor expansion but also by orthogonal polynomials, which provide different properties in convergence and tolerancing compared with Taylor expansion. There is a kind of often used aspherical surface representation called the Forbes asphere (or the Q-type asphere). There are two types of the Q-type asphere, which are called the strong asphere (Qcon) and the mild asphere (Qbfs). The strong asphere is written as the basic conic shape and a series of orthogonal polynomials as [23].

$$z_{Qcon} = \frac{cr^2}{1 + \sqrt{1 - (1 + \kappa)c^2r^2}} + r^4 \sum_{m=0}^{M-4} a_m Q_m^{con}(\bar{r}^{-2}), \quad (2-49)$$

where a_m denotes the coefficients of the polynomials, $x^2 Q_m^{con}(x)$ (with $x = \bar{r}^{-2}$) denotes an orthogonal set of polynomials, and $\bar{r} = r/r_{norm}$ denotes the normalized aperture radial coordinate. r_{norm} is the normalization radius. The set of polynomials are orthogonal, and it follows the relation as

$$\int_0^1 x^2 Q_m^{con}(x) x^2 Q_n^{con}(x) dx = h_m \delta_{mn}, \quad (2-50)$$

where h_m denotes a normalization constant, and δ_{mn} is the Kronecker delta. Therefore, the Qcon polynomials are sag/spatially orthogonal polynomials, while the mild aspheres have the property of slope/gradient orthogonal. The mild asphere is written as

$$z_{Q_{bfs}} = \frac{c_{bfs} r^2}{1 + \sqrt{1 - c_{bfs}^2 r^2}} + \frac{r^{-2} (1 - r^{-2})}{\sqrt{1 - c_{bfs}^2 r^2}} \sum_{m=0}^M a_m Q_m^{bfs} (r^{-2}). \quad (2-51)$$

In this case, the basic shape is no longer a conic section but a spherical shape with the curvature of c_{bfs} . The elements of the normal-departure slope are written as

$$Q_m^{Slope}(\bar{r}) := \frac{d}{dr} \left\{ r^{-2} (1 - r^{-2}) Q_m^{bfs} (r^{-2}) \right\}. \quad (2-52)$$

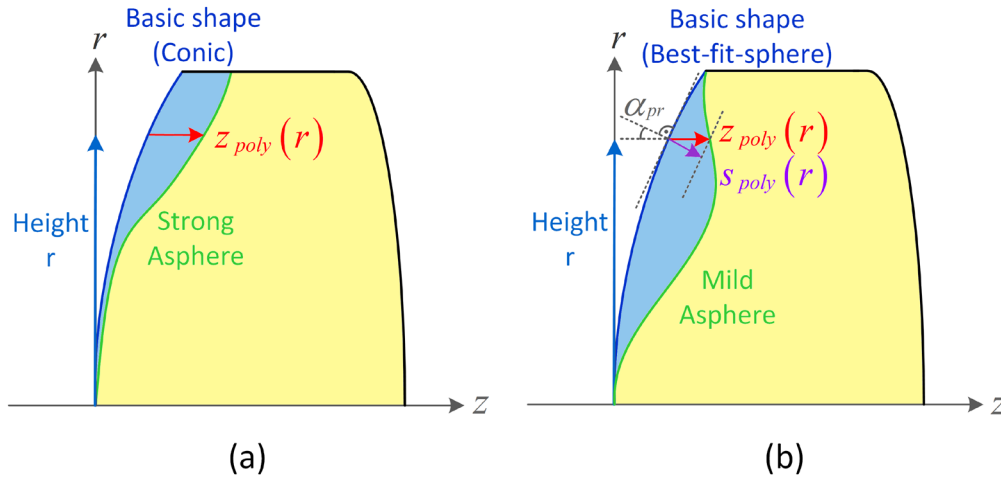


Figure 2-12 Deviation from the basic shape (a) along z-direction (b) projected from the normal direction.

The polynomials are chosen to make $Q_m^{Slope}(\bar{r})$ orthogonal. Thus the mild asphere is slope orthogonal. The polynomials are divided by a projection factor as

$$P(r) = \cos(\alpha_{pr}) = \sqrt{1 - c_{bfs}^2 r^2}, \quad (2-53)$$

where $\cos(\alpha_{pr})$ corresponds to the cosine of the projection angle. The projection angle is the angle between the local normal vector of the basic shape and the z-axis. The difference between strong asphere and mild asphere in the deviation from the basic shape as shown in Figure 2-12. For strong aspheres as in Figure 2-12 (a), the deviation from the basic shape to the aspherical shape is measured

along the z-axis. The polynomials are named as $z_{poly}(r)$. However for mild asphere as in Figure 2-12 (b), the polynomials without the projection factor named as $s_{poly}(r)$ are along the normal direction of the basic shape. When the polynomials are divided by the projection factor, they are projected onto the z-direction.

Thus, the strong asphere has a conic surface as the basic shape. The polynomials are sag orthogonal and along the z-axis. The mild asphere has a best-fit-sphere as the basic shape. The polynomials are slope orthogonal and along the normal direction.

2.6 Freeform surface representations

When optical systems are without rotational symmetry, freeform surfaces allow more degrees of freedom to improve the system performance. Freeform surfaces can be described using different mathematical representations. The frequently used freeform surfaces in optical system design are generalized as the sum of two parts. The first part is the basic shape, e.g., sphere, conic, or biconic, which incorporates mainly the paraxial behavior of the surface such as the focal power and the primary astigmatism. The second part is the deviation from the basic shape, which is normally described using different freeform polynomials. Therefore, the deviation part contains the freeform contribution from lower orders to higher orders [24]. The general description of a freeform surface is given as

$$z(x, y) = z_{basic}(x, y) + \frac{A(\bar{x}, \bar{y})}{P(x, y)} \sum F(\bar{x}, \bar{y}), \quad (2-54)$$

where z_{basic} denotes the sag of the basic shape, $A(\bar{x}, \bar{y})$ denotes the boundary function, $P(x, y)$ denotes the projection factor, and $F(\bar{x}, \bar{y})$ denotes the polynomials.

The normalization radius for circular aperture coordinate is replaced by two individual normalization length in x- and y-direction as x_{norm} and y_{norm} .

The general representation of the basic shape can also be written in the form of a biconic shape as

$$Z_{biconic} = \frac{c_x x^2 + c_y y^2}{1 + \sqrt{1 - (1 + \kappa_x) c_x^2 x^2 - (1 + \kappa_y) c_y^2 y^2}}. \quad (2-55)$$

When $c_x = c_y = c$ and $\kappa_x = \kappa_y = \kappa$, the basic shape becomes a conic section.

When $c_x = c_y = c$ and $\kappa_x = \kappa_y = 0$, the basic shape is a spherical surface.

The general description in Eq. (2-54) is written in Cartesian coordinates. For circular aperture based polynomials, the aperture coordinates can be written in the form of Eq. (2-47). The normalized radial aperture coordinate is written as $\bar{r} = r/r_{norm}$. For rectangular aperture based polynomials, the normalized aperture coordinate in x and y are defined according to Eqs. (2-56) and (2-57). The normalization radius for circular aperture is replaced with different normalization lengths x_{norm} and y_{norm} in x- and y-direction, but $x_{norm}^2 + y_{norm}^2 \neq r_{norm}^2$.

$$\bar{x} = \frac{x}{x_{norm}}. \quad (2-56)$$

$$\bar{y} = \frac{y}{y_{norm}}. \quad (2-57)$$

The frequently used freeform surface representations are written as follows.

- 1) Monomials (also known as XY-polynomials or Extended Polynomials) is one of the most frequently used freeform surface representations due to its suitability for manufacturing and the decoupling in x- and y-direction. The polynomials are based on Taylor expansion. However, since it is lack of orthogonality, the convergence in optimization is weak. The representation of monomials written in Cartesian coordinate is given as

$$Z_{Mono}(x, y) = Z_{basic}(x, y) + \sum_{m=0}^M \sum_{n=0}^N a_{mn} x^m y^n. \quad (2-58)$$

- 2) Zernike polynomials are sag orthogonal, which were used to describe the wavefront aberrations since different terms indicate different types of aberrations. Thus, due to its orthogonality and the direct relation to aberrations, it is often used to correct aberrations in non-rotationally symmetric optical systems. There are two sorting called standard convention and fringe convention. The Zernike standard surface representation in polar coordinate is written as

$$Z_{Zernike}(\bar{r}, \phi) = Z_{basic}(\bar{r}, \phi) + \sum_{n=0}^N \sum_{m=0}^M a_{nm} Z_n^m(\bar{r}, \phi). \quad (2-59)$$

The Zernike polynomials are defined in a circular aperture. The aperture coordinate is normalized. The standard convention can be transferred to the fringe convention, then it is written as

$$Z_{Zernike}(\bar{r}, \phi) = Z_{basic}(\bar{r}, \phi) + \sum_{i=0}^N a_i Z_i(\bar{r}, \phi). \quad (2-60)$$

- 3) As an extension of Forbes aspheres, the freeform surface can also be represented in the form of Forbes polynomials (also known as Q-polynomials). It holds the slope orthogonality with the benefit of both tolerance and convergence. It consists of the best-fit-sphere as the basic shape, the mild asphere part, and the freeform polynomials. The surface of Q-polynomials in polar coordinate is written as

$$\begin{aligned} Z_{Q-poly}(r, \theta) = & \frac{c_{bfs} r^2}{1 + \sqrt{1 - c_{bfs}^2 r^2}} + \frac{r^{-2} (1 - r^{-2})}{\sqrt{1 - c_{bfs}^2 r^2}} \sum_{n=0}^N a_n^0 Q_n^0(r^{-2}) \\ & + \frac{1}{\sqrt{1 - c_{bfs}^2 r^2}} \sum_{m=0}^M (\bar{r})^m \sum_{n=0}^N [a_n^m \cos(m\theta) + b_n^m \sin(m\theta)] \cdot Q_n^m(r^{-2}). \end{aligned} \quad (2-61)$$

With the projection factor, the Q-polynomials are also projected from the normal direction of the best-fit-sphere.

- 4) The Chebyshev 2D polynomials and Legendre 2D polynomials are spatially orthogonal. Different from Zernike polynomials, they are characterized by normalized rectangular apertures. However, the terms are not directly related to aberration terms. The mathematical form of those two types of polynomials are products of the 1D-polynomials, which are given as

$$Z_{Cheb}(x, y) = Z_{basic}(x, y) + \sum_{n=0}^N \sum_{m=0}^M a_{nm} T_n(\bar{x}) T_m(\bar{y}), \quad (2-62)$$

$$Z_{Lege}(x, y) = Z_{basic}(x, y) + \sum_{n=0}^N \sum_{m=0}^M a_{nm} P_n(\bar{x}) P_m(\bar{y}). \quad (2-63)$$

The difference is the expression of the 1D functions $T_n(x)$ and $P_n(x)$ due to different weighting function.

- 5) Considering all the properties of the mentioned surface representations such as orthogonality, aperture shape, boundary condition, and projection factor, there is one newly proposed freeform surface representation called A-polynomials. The basic shape is biconic, which provides different focal powers in x- and y-direction to compensate large astigmatism. Boundary

and projection factor can be defined to constrain the boundary properties and the direction of the polynomials along z-direction or normal direction. It combines the advantage of Zernike polynomials, which corresponds to aberration terms, and slope orthogonality of Q-polynomials. The aperture shape is rectangular. The general representation of A-polynomial is given as

$$z_{A-poly}(x, y) = z_{biconic}(x, y) + \frac{A(\bar{x}, \bar{y})}{P_{biconic}(x, y)} \sum_{i=0}^N a_i A_i(\bar{x}, \bar{y}). \quad (2-64)$$

The most significant difference between different freeform surface representations is the type of the polynomials. They can be classified into two types, which are non-orthogonal and orthogonal polynomials. The orthogonal polynomials consist of slope/gradient orthogonal and sag/spatial orthogonal polynomials. Surfaces with orthogonality tend to have better convergence in optimization, which is preferred by optical designers. The slope orthogonality also provides advantages in tolerancing. Other differences between the representations are the aperture shape, the boundary condition, the domain of definition, and whether they are Cartesian or polar based. The boundary function can define the property of the boundary and center of the surface. Some types of polynomials describe circular aperture, such as Zernike polynomials and Forbes polynomials. Some other types describe rectangular aperture, such as Chebyshev or Legendre polynomials, while monomial polynomials (also known as XY-polynomials) describe arbitrary aperture shape. The properties of some commonly used freeform polynomials are listed in Table 2-5.

Table 2-5 Comparison of different freeform surface representations

	Basis	Orthogonality	Domain
Monomials	Cartesian	None	Arbitrary
Chebyshev 2D	Cartesian	Spatial	Unit square
Legendre 2D	Cartesian	Spatial	Unit square
Zernike Fringe	Polar	Spatial	Unit circle
Q-polynomials	Polar	Gradient	Unit circle
A-polynomials	Polar	Gradient	Unit square

2.7 Traditional design process

Traditional optical systems are normally rotationally symmetric such as camera objectives, telescope objectives, and microscope objectives. The degrees of freedom in a system are the surface data, the thickness between surfaces and the materials. Since the optical components are centered on the optical axis, the geometry of the system structure is not very complicated.

The first step in the design process is always to review all the specifications, which include the first-order properties (such as focal length, f-number (F#), and numerical aperture), as well as the working spectral range, the field of view (FOV), system packaging constraints, the goal of imaging performance, material requirements, the detector size, the free working distance and etc.

Then a good starting point is essential for the further optimization. The methods mentioned in Section 2.1 aim to reach a good starting point for the system design. For traditionally systems, the starting configuration is normally capable of reaching some specifications such as the focal length or the f-number. The system can be formed by thin-lens components and then substituted with real lenses in the later optimization. It can also reach good performance for the on-axis field and small FOV. Later the FOV is step-by-step increased in the optimization. The designer can also use a patent or an existing system as the starting point, which has similar properties as the goal specifications, for modification and further optimization. The starting system can also be designed by the combination of two or more existing systems, which results in a so-called hybrid system [5].

Before further optimization, proper variables and constraints should be established in the design software. The spectral range and FOV are set as input [5]. The variables can be the radius of curvature, conic parameter, and distances (thicknesses and airspace), and the material characteristics. For more complicated systems, there will be more degrees of freedom corresponding to the complicated geometry or surface parameters. The constraints are corresponding to the specifications such as the first-order properties, the packaging parameters, the thickness constraints, the airspace range, and some ray height or angle constraints for specific rays when there is a special requirement for the detector or intermediate components.

After the constraints are set in the merit function (error function) of the software, the criteria of the performance should be set. Normally the default criteria are used in software as Zemax (OpticStudio). The performance criteria can be the root-mean-square (RMS) spot radius, the wavefront error, or the angular error for image space afocal systems. The number of arms and rings are defined to control the used sampling of rays in the optimization. The final merit function is evaluated with values of constraints and the performance criteria value. The goal is to optimize the value of the merit function so that the system performance, as well as constraints, can be fulfilled.

Normally the system does not reach the ideal performance by one simple optimization, especially for complicated systems with high specifications. There are local optimization and global optimization methods, which are based on different algorithms. The local optimization based on DLS is often used in Zemax. In this case, the optimization to reach the goal performance takes some time and iterations. The time and the difficulty depend on the complexity of the system. The more complex the system is, the more complicated the merit function will be. Thus, to run one cycle of optimization takes also longer time. It will also be hard to reach the global minimum value of the merit function by modifying the system structure or changing materials.

Before making a new iteration of the optimization, the system performance should be evaluated. The analysis of the performance can be based on the RMS spot radius, modulation transfer function (MTF), aberration values, or encircled energy, which give the information of the distribution of system errors. Before the next iteration of optimization, certain changes can be made in the system to reduce the influence of the error. For instance, if one surface has a large contribution in the aberrations, it can be split to redistribute the aberration contribution and reduce the sensitivity of the system. If the chromatic aberration is too large, it can be overcome by changing the materials. Furthermore, the weighting of different constraints in the merit function can also be changed. Every modification of the intermediate system will cause a change of the merit function. Therefore the system error jumps out of the local minimum and can be optimized again, which allows the possibility to meet the final performance. The strategy of the modification relies on the experience and theoretical basis of the designer. After

repeating the system optimization and performance evaluation for certain iterations, it is possible to reach the final goal of performance. Nevertheless, this is not the end of optical design.

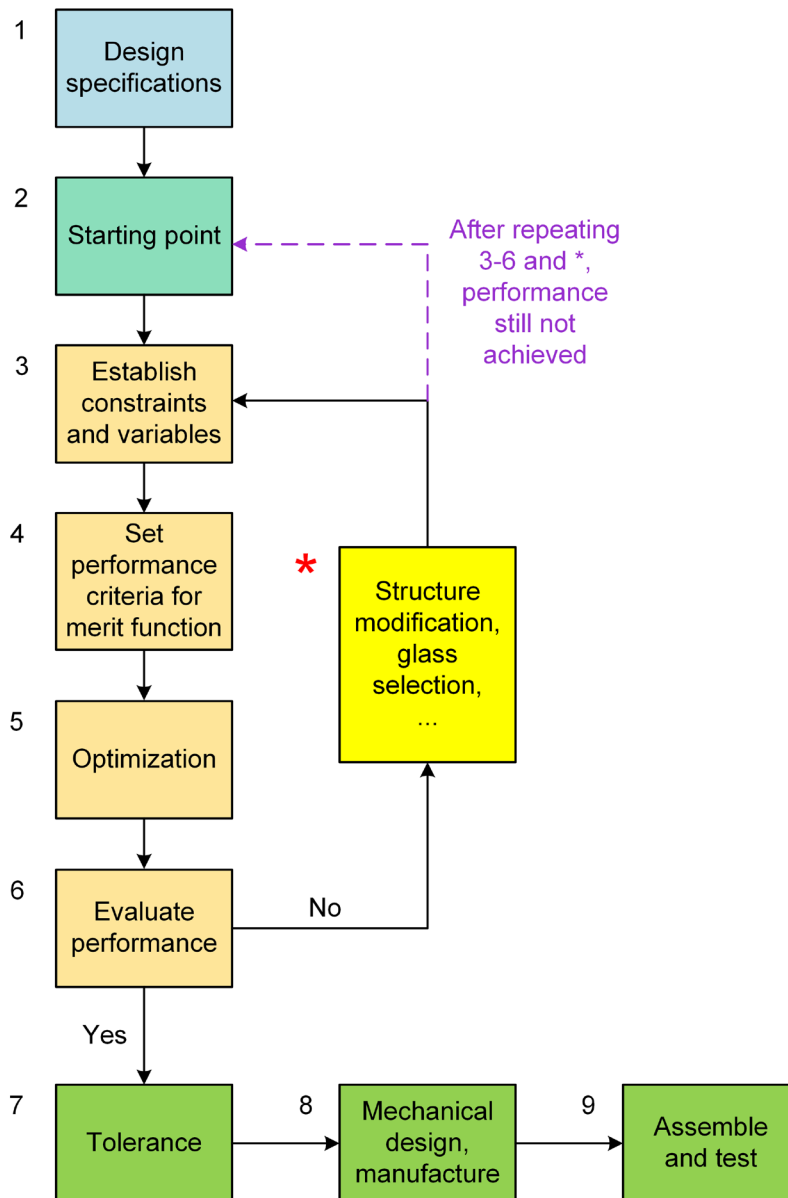


Figure 2-13 Workflow of the traditional design process [5]

In reality, no optical system can be optimized into ideal systems due to aberrations in the system. Similarly, the manufacturing and assembling have always errors, which lead to changes of surface data and distance, even with tilts and decentering of components. The tolerance analysis must be processed to see the influence of changes in every component and the sensitivity of the system before manufacturing. If the tolerance is too tight, a less sensitive system should

be selected or redesigned by reducing the influence of the most sensitive component with certain structure modification. The budget should be planned for the acceptable error range.

Finally, the system, which meets all the specifications and passes the tolerance analysis, can be manufactured. The mechanical design of the cell or housing is also important. Therefore, it is necessary to consider the mechanical design space in the design specifications. Once the optical and mechanical components are manufactured, the system can be assembled and tested. The last testing step also refers on the design specifications and requirements. The workflow of the traditional design process is illustrated in Figure 2-13. It can be seen that, beneath the repeating from step 3 to 6 and step (*) when the system performance is not fulfilled, a new starting point should be chosen when it is impossible to optimize the current structure to a final design [5].

2.8 Problems for non-rotationally symmetrical systems

Nowadays, it is hard to achieve the balance between the higher requirements of the optical system performance and the low-cost requirement. In traditional point of view, higher performance can be achieved using large number of elements and special materials. However, in reality, the working space and system size are normally limited. There is also a budget of the cost of the whole system. Therefore, it is normally the challenge to realize the achievable performance in the limited space with the limited cost.

One way to reduce the system size is to fold the system with reflective components. By using the same space several times by reflective effect, the system size is tremendously reduced. When the reflective components are tilted or decentered, obscuration can be avoided. That would lead to non-rotationally symmetric effect in the system performance. The development of manufacturing technology makes it realistic to use freeform surfaces. Components with freeform surfaces own the capability to compensate the non-rotationally symmetric aberrations in the system. Therefore, it is possible to reduce the number of components in non-rotationally symmetric systems by freeform surfaces. Typical applications are three-mirror-anastigmats (TMAs), head-mounted-displays (HMDs), and Yolo-telescope systems. In some other systems with special requirement of focal powers

in x- and y-direction, such as anamorphic systems, freeform surfaces are also used to achieve high performance. Therefore, in the last ten to twenty years, the focus of optical design shifts to non-rotationally symmetric systems with freeform surfaces to large extent. However, as a new topic in optical design, there are some problems to be solved for non-rotationally symmetric systems.

1) Complex geometric structure

In centered system, the geometric relation between components or surfaces are the distances or thicknesses. Therefore, the size of the system is normally limited by one dimension along the unique optical axis. The other dimension is limited by the optical component size, which can be constrained with the ray height on the component during optimization. Thus, the geometric structure of the centered system is relatively simple and clear. Nevertheless, when the components are shifted or tilted in a non-rotationally symmetric system, the geometry to describe the relation between components contains not only distances but also angles. The propagation lost rotational symmetry of the field coordinate. Even for the central field, the ray cone is not rotationally symmetric. The complex structure will lead to the following problems.

2) Analysis of aberrations

Non-rotationally symmetric effect is already studied to certain extent in centered systems, which corresponds to the misalignment of components. NAT was established based on the misalignment effect of optical components. When the surface is tilted or centered, it will introduce a perturbation effect in the system performance. Therefore, NAT is widely used in the analysis of non-rotationally symmetric systems. However, it is based on small perturbation of the system. Compared with real cases with large tilt angles or decentering, the aberration values are not accurate. It is normally used to analyze the nodal points of aberrations and if the system is dominated by field-constant aberration. The extension of NAT concerning large tilt and decentering is also one of the popular research topics. To analyze the aberrations in the system, we need new tools because the aberrations can no longer be represented simply by the largest field. Full-field-display of aberrations are implemented to illustrate the whole distribution of the aberrations over the FOV.

3) Change of aberrations due to structure change

According to Seidel aberration theory, rotationally symmetric systems suffer from rotationally symmetric distributed aberrations. Spherical aberration is field-constant. The marginal ray has the largest incident angle on each surface compared with other rays of the axial field. Coma, astigmatism, field curvature and distortion are all field-related. Thus the largest field suffers from the largest aberrations. By looking at the Seidel coefficients, we can see which surface has the largest aberration contribution. It is predictable that which aberrations will be influenced when the system structure changes, such as splitting or pupil shift. Seidel coefficients are the aberrations of the largest field because the field height is normalized by the largest field over the whole FOV. For both aberration analysis and optimization of rotationally symmetric systems, the strategies are relatively clear.

For the non-rotationally symmetric system, it has several differences. Concerning the influence of the basic shape as spherical surfaces, due to the tilt or decentering of the surface, there is a field shift factor, which leads to different changes of different aberrations due to the different power of field relation. For example, coma has a linear relation with the field. Thus the influence of the field shift factor can be seen as a constant value, which is added to the field-linear coma. At the end, the total coma of surfaces can be seen as the sum of the field-linear coma and the constant value. But for astigmatism, since the relation with field is nonlinear, the influence of the field shift factor is also complicated. Hence it is hard to decide how much the individual tilts or decentering should be to correct all the aberrations. For special systems such as Scheimpflug systems, the components are centered on the common optical axis, but the imaging condition is asymmetric. Thus, the aberration distribution is also non-rotationally symmetric. When aspherical surfaces or freeform surfaces are added on the surface shape, it becomes even more complicated because each ray will be locally influenced by the local curvature at the intersection point. It is hard to see how large the change of aberrations will be caused by different part of the surface. Therefore, the influence can only be optimized by the performance criteria in the merit function. The chosen of fields is also complicated because of the non-rotational symmetry. The whole FOV should be taken into consideration.

4) Obscuration

In centered systems with refractive components, obscuration is normally not considered. When the system consists of reflective components as telescopes, the obscuration is a problem. Beams are truncated at certain components. Therefore to achieve certain resolution and brightness, the components are normally quite large to overcome the loss of energy due to obscuration.

The obscuration size is controlled by the ray height on the surface and the distance between surfaces. However, off-axis systems provide the possibility to avoid obscuration and obtain small system size due to the large direction change of rays. But the controlling of obscuration during the design procedure is not easy. Since the ray direction is controlled not only by the focal power of the surface but also the tilt or decentering of the surface, during optimization certain constraints should be added in the merit function to keep the rays away from other components. When the system is formed by large number of surfaces or the same space is used several times due to the folding effect, constraints will be hard to define since the geometry is complicated, and the boundary ray heights should be constrained in more than one direction.

5) Initial setup

As mentioned, the aberrations in the non-rotationally symmetric systems are complicated. For bended axis ray, the system is in a real-ray-based paraxial environment. The resolution and distortion are separated, and it is more complicated to defined paraxiality. Therefore it is not enough to control the whole aberrations by reducing the aberrations of the boundary fields in the system. Before adding freeform polynomials, it is preferred to minimize the aberrations in the system with basic shapes. Thus, we can consider to minimize the aberrations of the central field. If the central field has no aberrations, which means it is the nodal point, the fields close to the nodal point will also suffer from relatively small aberrations. Therefore, one goal of initial system design is to obtain the nodal points in the FOV. In our work, we introduce two methods to optimize the aberrations of the selected field before adding freeform surfaces. There are also other methods to design the initial systems. From another point of view, the initial system can be directly formed by some freeform surfaces, which leads to sharp image of some field points. The SMS method mentioned in Section 2.1 works in this approach.

6) Design rules and workflow

In Section 2.7, the design procedure of the traditional systems is introduced. However, due to the new problems in non-rotationally symmetric systems, certain rules or details should be added in the workflow such as constraints to obtain obscuration free and the control of distortion. Some designers prefer to design the system with components centered on the axis, then tilt the components to remove obscuration. Some prefer to start with tilted plane surfaces to control the position of the surfaces and then optimize the curvatures to obtain the target focal power of the system. In different cases, the design procedure is completely different. In the optical design community, there is not yet a general rule to design non-rotationally system with freeform surfaces.

7) Freeform surfaces

In the design procedure, one of the biggest problems is the use of freeform surfaces. Different freeform surface representations have different mathematical properties, which lead to different performance in the design process. For different optical systems, the situation varies tremendously concerning number of components, the field distributions on the surfaces, and aberration contributions of surfaces. It is hard to generate a simple rule how to select the best working location of the freeform surface and the best working representation at the location. When more than one freeform surface are needed, it becomes even more complicated. It is preferred to have less number of freeform surfaces due to the low-cost requirement. The freeform surfaces should have a good performance working together. Therefore, it is still not clear about the best selection of the freeform surface locations and the optimization procedure with the increased number of polynomials. Constraints of the surface sag and slope are hard to define in optical design software, although they are important for the manufacturing procedure. Therefore, before coming to the tolerance step, not only the system performance but also the surface manufacturability should be evaluated. The tolerance of the freeform surface is also complicated since it can have huge number of polynomials, which are also the degrees of freedom in the system. The optimization procedure of freeform surfaces is already a large topic, although it is only one part of the whole design process.

3 New methods and results

3.1 Vectorial aberration theory

According to the symmetry of imaging systems, systems can be classified into general non-symmetric systems, plane-symmetric systems, double plane-symmetric systems, and axial symmetric systems as shown in Figure 3-1. In rotationally symmetric (axial-symmetric) systems, the distributions of aberrations are also rotationally symmetric. As mentioned in Section 2.2, the traditional description of aberrations is in the wave aberration, the transverse aberration, and the longitudinal aberration. The field height and the pupil coordinate are described by scalar parameters. The field is considered in the tangential plane. However, when the system loses the rotational symmetry, the ray propagation will be expanded from the two-dimensional vector to the four-dimensional vector with the ray heights h_x and h_y in x- and y-direction and the ray angles u_x and u_y in x- and y-direction.

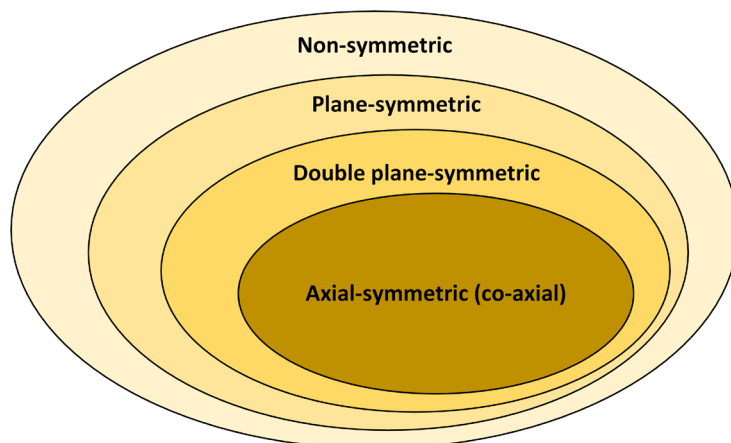


Figure 3-1 Classification of systems according to symmetry

Thus, the paraxial transfer matrix is extended from 2x2 to 4x4 matrix as [25]

$$\begin{pmatrix} h'_x \\ h'_y \\ u'_x \\ u'_y \end{pmatrix} = \begin{pmatrix} A_{xx} & A_{xy} & B_{xx} & B_{xy} \\ A_{yx} & A_{yy} & B_{yx} & B_{yy} \\ C_{xx} & C_{xy} & D_{xx} & D_{xy} \\ C_{yx} & C_{yy} & D_{yx} & D_{yy} \end{pmatrix} \begin{pmatrix} h_x \\ h_y \\ u_x \\ u_y \end{pmatrix}, \quad (3-1)$$

and is referred onto the local coordinates of the axis ray or chief ray, which can have an arbitrary path. When the ray propagation is extended from the tangential plane to the full 3-dimensional coordinates, the aberrations are no longer represented by the scalar parameters as in the Seidel aberration representation. The

field and pupil coordinates are both extended to vectorial representations in x- and y-axis. Therefore, if the normalized field and pupil vectors are projected to the same plane, the relation is illustrated as in Figure 3-2. The relation in the system is illustrated in Figure 3-3.

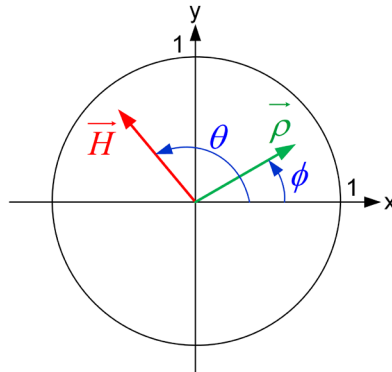


Figure 3-2 Normalized field vector \vec{H} and pupil vector $\vec{\rho}$

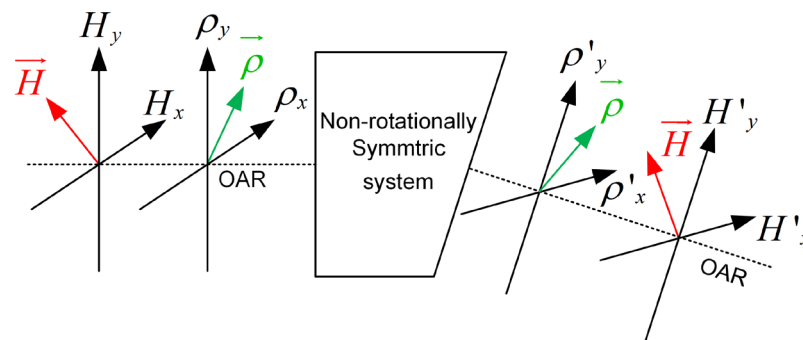


Figure 3-3 Vectorial coordinates in a non-rotationally symmetric system

Therefore, the wave aberration expansion as in Eq. (2-3) can be written in the form of Eq. (2-8), according to the relation in Eq. (2-10) and Eq. (2-12). The terms of the wave aberrations in scalar and vectorial representations are listed in Table 3-1. In Seidel aberration theory, the field is assumed on the y-axis. If $H_x = 0$ and $H_y = H$, the scalar terms in Table 3-1 are exactly the Seidel aberration terms in Eq. (2-3). For a system without rotational symmetry, the wave aberration can be expanded in the vectorial terms as in Table 3-1, where the piston terms are neglected.

For different object distances, since the paraxial ray trace data are not the same, the Seidel coefficients W_{klm} are variant. Thus, the aberrations in the whole system with variant object distance cannot be characterized by one single expansion as in Eq. (2-8).

Table 3-1 List of aberrations in scalar and vectorial representations

Order	Name of the term	Scalar representation	Vectorial representation
2	Change of magnification in x	$H_x \rho \cos \phi$	$\vec{H} \cdot \vec{\rho}$
	Change of magnification in y	$H_y \rho \sin \phi$	
	Defocus	ρ^2	$\vec{\rho} \cdot \vec{\rho}$
4	Spherical aberration	ρ^4	$(\vec{\rho} \cdot \vec{\rho})^2$
	Coma in x	$H_x \rho^3 \cos \phi$	$(\vec{H} \cdot \vec{\rho})(\vec{\rho} \cdot \vec{\rho})$
	Coma in y	$H_y \rho^3 \sin \phi$	
	Astigmatism in 0°	$(H_x^2 - H_y^2) \rho^2 \cos 2\phi$	$\vec{H}^2 \cdot \vec{\rho}^2$
	Astigmatism in 45°	$2H_x H_y \rho^2 \sin 2\phi$	
	Focal plane of medial astigmatism	$H^2 \rho^2$	$(\vec{H} \cdot \vec{H})(\vec{\rho} \cdot \vec{\rho})$
	Distortion in x	$H^2 H_x \rho \cos \phi$	$(\vec{H} \cdot \vec{H})(\vec{H} \cdot \vec{\rho})$
	Distortion in y	$H^2 H_y \rho \sin \phi$	
6	Oblique spherical aberration	$H^2 \rho^4$	$(\vec{H} \cdot \vec{H})(\vec{\rho} \cdot \vec{\rho})^2$
	Coma in x	$H^2 H_x \rho^3 \cos \phi$	$(\vec{H} \cdot \vec{H})(\vec{H} \cdot \vec{\rho})(\vec{\rho} \cdot \vec{\rho})$
	Coma in y	$H^2 H_y \rho^3 \sin \phi$	
	Astigmatism in 0°	$H^2 (H_x^2 - H_y^2) \rho^2 \cos 2\phi$	$(\vec{H} \cdot \vec{H})(\vec{H}^2 \cdot \vec{\rho}^2)$
	Astigmatism in 45°	$2H^2 H_x H_y \rho^2 \sin 2\phi$	
	Focal plane of medial astigmatism	$H^4 \rho^2$	$(\vec{H} \cdot \vec{H})^2 (\vec{\rho} \cdot \vec{\rho})$
	Distortion in x	$H^4 H_x \rho \cos \phi$	$(\vec{H} \cdot \vec{H})^2 (\vec{H} \cdot \vec{\rho})$
	Distortion in y	$H^4 H_y \rho \sin \phi$	
	Trefoil in x	$(H_x^3 - 3H_y^2 H_x) \rho^3 \cos 3\phi$	$\vec{H}^3 \cdot \vec{\rho}^3$
	Trefoil in y	$(3H_x^2 H_y - H_y^3) \rho^3 \sin 3\phi$	
	Spherical aberration	ρ^6	$(\vec{\rho} \cdot \vec{\rho})^3$
	Coma in x (secondary)	$H_x \rho^5 \cos \phi$	$(\vec{\rho} \cdot \vec{\rho})^2 (\vec{H} \cdot \vec{\rho})$
	Coma in y (secondary)	$H_y \rho^5 \sin \phi$	
	Astigmatism in 0° (secondary)	$(H_x^2 - H_y^2) \rho^4 \cos 2\phi$	$(\vec{\rho} \cdot \vec{\rho})(\vec{H}^2 \cdot \vec{\rho}^2)$
Astigmatism in 45° (secondary)	$2H_x H_y \rho^4 \sin 2\phi$		

For a Scheimpflug system, each object height has its own object distance and has an individual expansion of wave aberration regarding the field and pupil vectors. The wave aberration expansion mentioned in Eq. (2-8) only concerns the rotationally symmetric optical components. The Seidel aberrations are influenced

by the shift factor and derived in a set of conjugate shift equations [13]. It is difficult to correct all the aberrations with only the spherical shapes.

Table 3-2 Properties of systems with different symmetry

OAR	Surface symmetry	Aberration theory						Reference			Sample systems		
		4 th order		6 th order		Exact – all orders		Ray		Transfer matrix			
		Seidel, with field	Araki	Vectorial I – with field Shack/Thompson/Sasian	Vectorial II – with field Fuerschbach	Aldi's theory – one ray only Welford – one OPD point only	Oleszko - Zernike	Paraxial - axis	Parabasal around real OAR/CR	2x2		4x4	5x5
Straight	Rotational-symmetric	Dark Blue	Light Blue	Dark Blue	Light Blue	Dark Blue	Dark Blue	Dark Blue	Dark Blue	Dark Blue	Dark Blue	Dark Blue	Photographic lens, microscope, zoom lens
	Double plane-symmetric	Dark Blue	Light Blue	Dark Blue	Dark Blue	Yellow	Dark Blue	Dark Blue	Dark Blue	Dark Blue	Dark Blue	Dark Blue	Anamorphic
	Freeform (plane-symmetric)	Yellow	Light Blue	Yellow	Dark Blue	Yellow	Dark Blue	Dark Blue	Dark Blue	Dark Blue	Dark Blue	Dark Blue	Scheimpflug
	Freeform (non-symmetric)	Yellow	Light Blue	Yellow	Dark Blue	Yellow	Dark Blue	Dark Blue	Dark Blue	Dark Blue	Dark Blue	Dark Blue	Cubic phase plate for EDF
1D bend	Rotational-symmetric	Yellow	Dark Blue	Dark Blue	Dark Blue	Yellow	Dark Blue	Dark Blue	Dark Blue	Dark Blue	Dark Blue	Dark Blue	Schiefspiegler telescope, TMA (spherical), HMD
	Double plane-symmetric	Yellow	Dark Blue	Dark Blue	Dark Blue	Yellow	Dark Blue	Dark Blue	Dark Blue	Dark Blue	Dark Blue	Dark Blue	Anamorphic prism stretcher
	Freeform (plane-symmetric)	Yellow	Light Blue	Yellow	Dark Blue	Yellow	Dark Blue	Dark Blue	Dark Blue	Dark Blue	Dark Blue	Dark Blue	Unobscured telescope, TMA (corrected), HMD
	Freeform (non-symmetric)	Yellow	Light Blue	Yellow	Dark Blue	Yellow	Dark Blue	Dark Blue	Dark Blue	Dark Blue	Dark Blue	Dark Blue	Alvarez plate systems, panoramic zoom system
2D bend	Rotational-symmetric	Yellow	Dark Blue	Dark Blue	Dark Blue	Yellow	Dark Blue	Dark Blue	Dark Blue	Dark Blue	Dark Blue	Dark Blue	Yolo telescope (spherical)
	Freeform (non-symmetric)	Yellow	Light Blue	Yellow	Dark Blue	Yellow	Dark Blue	Dark Blue	Dark Blue	Dark Blue	Dark Blue	Dark Blue	Yolo telescope (corrected)

When the system consists of freeform components, the freeform deviation from the rotationally symmetric shape introduces some aberrations, which does not follow the relation of the even order rule as in Table 3-1. The relation of field and pupil orders are arbitrary, which will be introduced in the following sections. Therefore, the properties are summarized in Table 3-2 for systems with different symmetry. The properties are marked with different colors (dark blue: meaningful; light blue: valid but not meaningful; yellow: not valid). In the vectorial aberration of basic shapes (vectorial I), tilt and decentering are considered [14-17]. In the

extension of vectorial aberration theory (vectorial II), the influence of freeform surface is discussed [26, 27]. The aberration theory of Araki is valid for the primary aberration analysis [28, 29]. For higher order aberration analysis, Aldi's theory (only for one single ray) or the theory from Welford for one optical path difference (OPD) point, and the Zernike-based aberration analysis by Oleszko can be used [30-32]. Moreover, the 5×5 transfer matrix is the general formation if surface tilts, decentering, tilt addition and image translation are considered [33]. The reference of ray is discussed in Section 3.2.

3.2 Parabasal reference

When classical rotationally symmetric systems are discussed, the starting point is usually paraxial optics. It is assumed that all the ray angles are small. Thus, only the linear effect of refraction is considered. The perturbation of real ray heights and angles from the paraxial case leads to errors in the imaging condition, which is called aberration. Since the surface vertexes, the object and image centers, and the pupil centers are all located on the unique optical axis, it is assumed that the rays lie in a neighborhood of the optical axis. Therefore rotationally symmetric systems are based on paraxial reference.

In non-rotationally symmetric systems, there is a group of systems with all the components located on the same optical axis. The non-rotational symmetry is introduced to the system by using freeform components or non-uniform imaging condition. The system environment is still in paraxial reference. For instance, in the anamorphic system as in Figure 3-4 (a), the two cylindrical lenses introduce asymmetric focal powers in x- and y-direction to the system. The OAR is along the unique axis of the system. Thus, the analysis of aberrations is still based on paraxial approximation.

Another example is the Scheimpflug system as in Figure 3-4 (b). The non-symmetry is due to the variant magnification along the field. The object plane is tilted around the x-axis. Therefore, the object points A, B and C along the field have different object distances. When analyzing the aberrations of those three fields, the marginal rays and chief rays are different for different object distances. For each object distance, it can be regarded as a rotationally symmetric system. Each object distance is analyzed in paraxial environment.

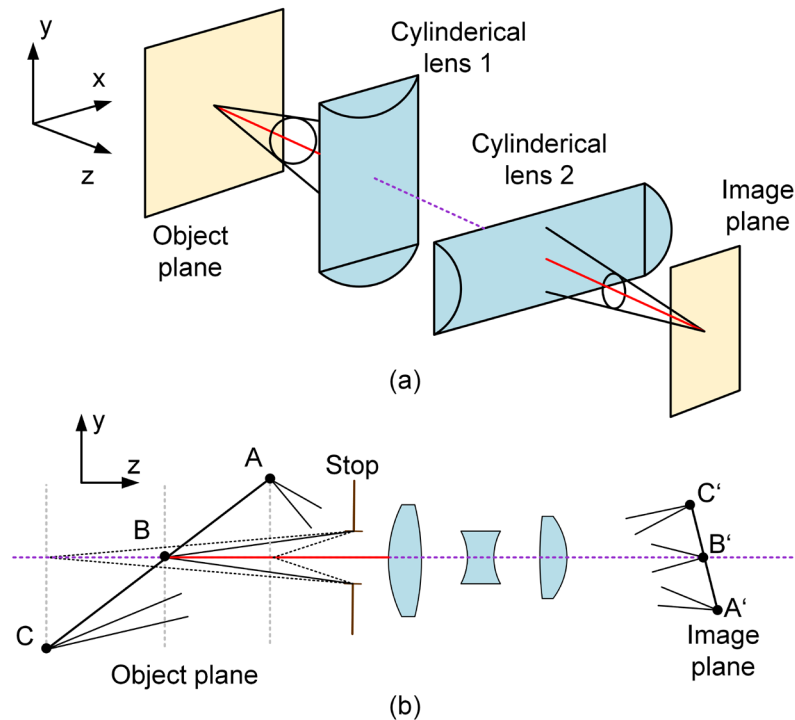


Figure 3-4 Non-rotationally symmetric systems with paraxial environment. (a) Anamorphic system; (b) Scheimpflug system.

The second group of non-rotationally symmetric systems is the off-axis system. Four kinds of off-axis systems are illustrated in Figure 3-5. The first system in Figure 3-5(a) is a two-mirror telescope system with off-axis aperture. The two mirrors are centered on the same optical axis. However, due to the shift of the stop from the co-axis, the fields are also decentered from the optical axis, which means only off-axis apertures of the two mirrors are used. If we only consider the used part of the mirror, the system can be seen as an off-axis system. Figure 3-5 (b) shows a TMA system, in which all the three mirrors are off-axis. Each mirror has an individual axis along the vertex and the center of the surface. In Figure 3-5 (c), the HMD system with two reflective and two refractive surfaces is shown. The reflective surfaces are used to fold the ray path in order to reduce the system size. The last system in Figure 3-5 (d) is a Yolo telescope system with two mirrors. For Yolo telescope, the beam is not only folded in the tangential plane, but also in the sagittal plane. Therefore, the system is without symmetry.

For all the systems in Figure 3-5, the OAR is not along a unique axis anymore. Instead, the OAR is bent by the surfaces, which leads to a certain finite non-paraxial incident angle of the OAR on the surface. Therefore, the OAR is not the paraxial ray anymore. It is called the parabal ray and must be based on real

ray trace. In paraxial reference, all the rays are assumed to be in an environment near the paraxial ray, while in off-axis systems all the rays are assumed to be in an environment near the parabasal ray [34].

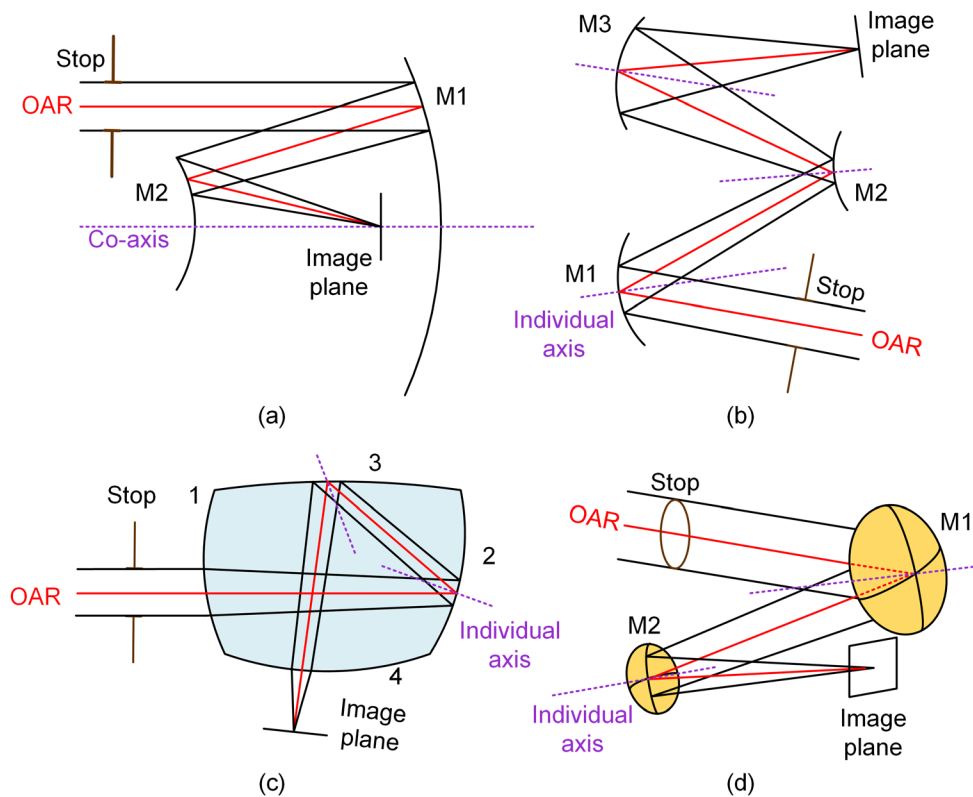


Figure 3-5 Off-axis systems with parabolasal environment. (a) Co-axis two-mirror system; (b) TMA system; (c) HMD system; (d) Yolo telescope.

In the parabolasal environment, when the bending of OAR leads to large incident angles of the surfaces, the aberrations of the central field cannot be neglected, which corresponds to the field shift vector in NAT. The OAR (parabolasal ray) should be based on the real ray tracing. The other fields are based on paraxial ray tracing near the parabolasal ray. Therefore, when we use NAT to analyze an off-axis system, the theory is based on a mixture of paraxial environment and parabolasal environment with finite ray trace of the OAR.

3.3 Initial system finding

Finding a good starting system is always an important topic in optical design. In this chapter, two kinds of methods are introduced to design non-rotationally symmetric systems. One is based on confocal conic surfaces, which works for off-axis systems. The conic confocal method is investigated by many researches [7,

35, 36]. In this thesis, we illustrate the complete design process step by step and add the correction of field curvature together with the obscuration free condition. The other one is called Gaussian brackets method based on NAT, which works for general systems. In this method, the initial system is designed with spherical surfaces, which allows further correction by conic or aspherical surfaces before adding freeform surfaces.

3.3.1 Conic-confocal method

In principle, the conic-confocal method can be applied to both refractive and reflective system with more than one surfaces [7, 35-37]. In this work, we demonstrate the method with a special case, which is with three mirrors. As mentioned in Section 2.5, conic shaped reflective surfaces can image certain bundles of rays without any geometric error. The reflective surface shapes, which have the property to reflect all rays emerging from an initial point to the same image point, are called Cartesian surfaces [8]. Thus, the conic-shaped reflectors are Cartesian surfaces. The parabolic reflector, the hyperbolic reflector, and the elliptical reflector all have two geometric focal points as in Figure 3-6. For a parabolic reflector, one geometric focal point is at infinite distance from the surface. Those three kinds of conic reflectors can image the field starting from one geometric focal point perfectly to another. The two geometric focal points are named a stigmatic pair. The imaging property is called stigmatism [8].

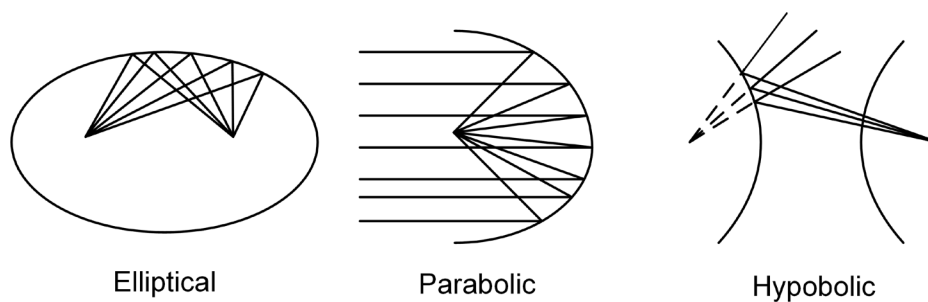


Figure 3-6 Cartesian surfaces

It is known that in an off-axis TMA system, it is possible to minimize spherical aberration, coma, astigmatism, and field curvature with three mirrors. However, the condition to achieve the goal is complicated in calculation. For instance, it follows different conditions to achieve sine condition and astigmatism free

condition, or to correct Petzval curvature. When the TMA system consists of certain FOV, it is even more challenging to correct aberrations of every field. One approach to correct the aberrations is to add freeform degrees of freedom to the mirrors, which means the freeform surface will provide the ability to compensate the residual aberrations in the initial system. From the manufacturing point of view, the cost and difficulty to manufacture a freeform surface is directly related to the complexity of the freeform shape. It is also known that the freeform surface provides possibility to change the bending of rays locally with different local curvature at individual points of the surface. Large residual aberrations in the initial system request large deviation of the freeform part to provide more correction ability, which will increase the cost and difficulty in manufacturing. Thus, it is a smarter design strategy to obtain a good initial system with small residual aberrations before adding the freeform surface.

Considering the 4th order wave aberrations, which are the primary aberrations in a system, it is not realistic to request all the fields corrected for an off-axis system with only basic surface shapes. Therefore, one design strategy is to obtain one or more nodal points in the FOV. Then the fields near the nodal point will suffer from relatively small aberrations. In a three-mirror system, it is possible to obtain one nodal point by using three Cartesian surfaces, if the second mirror has one confocal point with the first mirror and another confocal point with the third mirror. The object point, intermediate image points and the image point of the field all locate on the stigmatic pairs. Here, the central field is selected as the nodal point. The first mirror is always parabolic shaped in the case of a telescope with the object lying in infinity. The second and the third mirrors can be either elliptical or hyperbolic shaped. The types of mirrors are listed in Table 3-3.

Table 3-3 Surface types in conic-confocal method

	M1	M2	M3
Infinite object	Parabolic	Elliptical/hyperbolic	Elliptical/hyperbolic
Finite object	Elliptical/hyperbolic	Elliptical/hyperbolic	Elliptical/hyperbolic

From the NAT, it is known that the spherical aberration is field-constant for an imaging system with fixed object distance. For a TMA system, if the central field is perfectly imaged, it means the spherical aberration vanishes.

The condition to obtain corrected field curvature is relatively simple. It is only related to the radii of curvature of the three mirrors. According to the definition of

Petzval curvature as in Eq. (3-2), the condition to flatten the field is to obtain the value of Petzval curvature as zero [11].

$$\frac{1}{R_{ptz}} = -n'_k \sum_j \frac{n_j' - n_j}{n_j \cdot n_j'} \cdot c_j, \quad (3-2)$$

where $1/R_{ptz}$ denotes the Petzval curvature. n'_k denotes the index in the image space. c_j denotes the curvature of the j^{th} surface. n_j and n_j' denote the refractive index before and after the j^{th} surface. Therefore, for a three-mirror system, the Petzval curvature vanishing condition can be derived as

$$c_1 - c_2 + c_3 = 0. \quad (3-3)$$

It is known that astigmatism is introduced because of the different focal powers of a surface in tangential and sagittal planes. In an off-axis system, the incident angle of the OAR on each surface leads to different focal powers in x- and y-direction. By certain combination of the OAR incident angles on the three mirrors, it is possible to achieve equal focal powers in tangential and sagittal directions for the whole system. Since the central field is perfectly imaged, the astigmatism is already canceled. However, it is better to obtain small astigmatism near the central field. According to the theory of S. Chang, the linear astigmatism of a three-mirror system can be vanished following the relation as

$$(1 + m_1)m_2m_3 \tan(i_1) + (1 + m_2)m_3 \tan(i_2) + (1 + m_3) \tan(i_3) = 0, \quad (3-4)$$

where m_j denotes the local magnification of the j^{th} mirror. i_j denotes the incident angle of the OAR on the j^{th} mirror [7, 36]. Due to the parabal environment, the definition of local magnification is different from the paraxial magnification.

As it can be seen in Figure 3-7, the object distance l is defined as the distance between the object point and the intersection point of the OAR. The image distance l' is defined as the distance from the intersection point of the OAR to the image point. Then the local magnification of the j^{th} surface is defined as the ratio between the image distance and the object distance as in Eq.(3-5). The incident angle is defined as the angle from the normal vector to the OAR.

$$m_j = \frac{l_j'}{l_j} \quad (3-5)$$

Therefore, the design steps of the conic-confocal method are as follows. The workflow is shown in Figure 3-8.

1) Obtain the on-axis setup with spherical surfaces

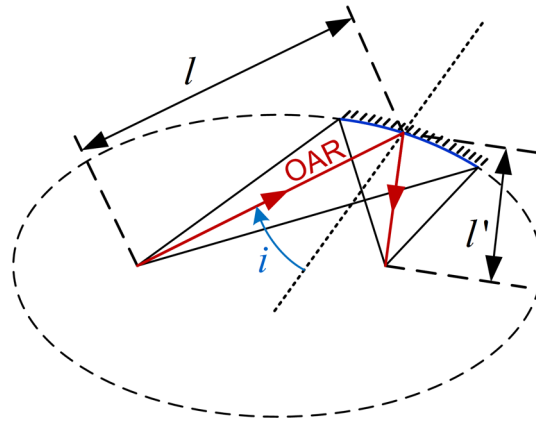


Figure 3-7 Local magnification of an off-axis conic surface

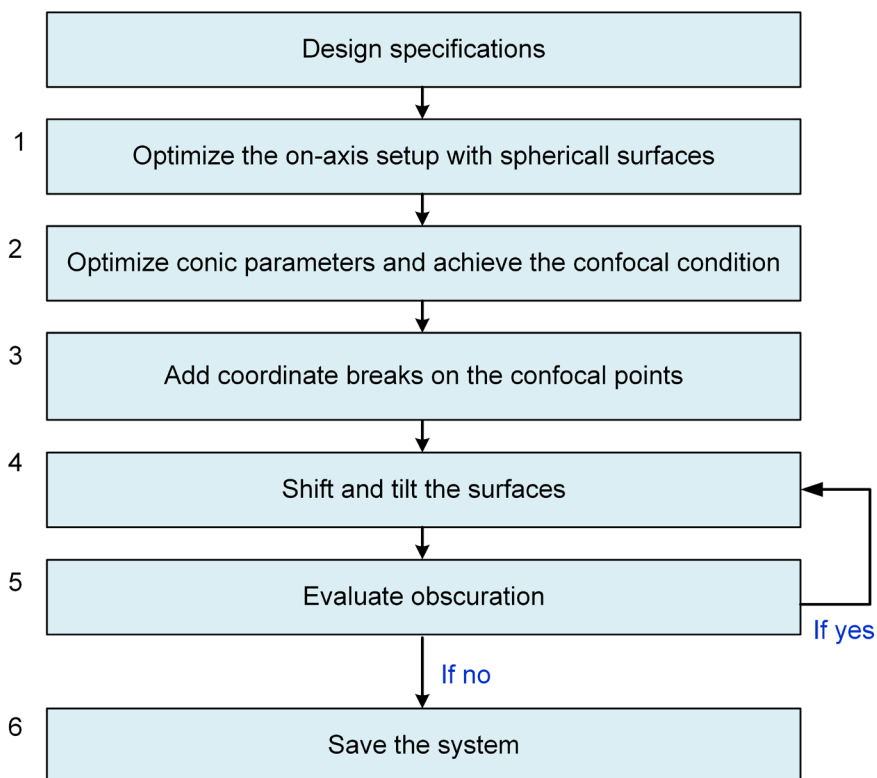


Figure 3-8 Workflow for the conic-confocal design method in Zemax/OpticStudio

Firstly, the on-axis setup should be obtained with only spherical surfaces. The goal of this step is to obtain a three-mirror telescope system with a Galileo telescope formed by the first two mirrors. The third mirror converges the collimated beam to the image plane [35]. Therefore, the radii of curvature and distances should follow certain relations. The relations to obtain the on-axis setup with spherical surfaces are given as Eqs. (3-6)-(3-10) and the Petzval vanishing condition is given as in Eq. (3-3), where d_1 denotes the distance from the first mirror to the second mirror, d_3 denotes the image distance from the third mirror to the

image plane, and f' denotes the focal length of the whole system. Since the field is collimated after the second mirror, the distance between the second mirror and the third mirror can be arbitrary. Thus, the distance d_2 between the second mirror and the third mirror is defined the same as d_1 .

$$\frac{1}{c_1} + 2(d_3 + f') = 0 \quad (3-6)$$

$$\frac{1}{c_2} - 2d_3 \left(\frac{d_3}{f'} + 1 \right) = 0 \quad (3-7)$$

$$\frac{1}{c_3} - 2d_3 = 0 \quad (3-8)$$

$$d_1 + \frac{1}{f'} (f' + d_3)^2 = 0 \quad (3-9)$$

$$|d_3| - |d_1| > 0 \quad (3-10)$$

Some of the relations are hard to define in the merit function. In Zemax or Optic-Studio, it is possible to define certain functions in the ZPL file (language macro) and call the value of the function in the merit function. Therefore, the conditions to obtain the setup can be defined and then optimized by the combination of ZPL file and merit function.

2) Optimize the conic parameters and achieve the confocal condition

In the second step, the surfaces are optimized to conic shape. The geometric focal points should also coincide with each other. It is mentioned that the first mirror should be parabolic shape, if the object is at infinite distance. Thus, the conic parameter should be optimized to -1 due to the optimization of spherical aberration. The other two surfaces can be either elliptical or hyperbolic. Thus, the conic parameters of the second and the third mirrors should be smaller than zero. The Petzval curvature vanishing condition as in Eq. (3-3) still should be fulfilled. In the merit function, the focal length of the whole system should be also defined. To obtain confocal condition, the Seidel coefficient of spherical aberration of each mirror should be optimized to zero. Following this rule, the geometric focal points will automatically coincide. Because for a Cartesian surface, only when the stigmatism condition is fulfilled, the spherical aberration vanishes. The intermediate image points move to the geometric focal points during optimization to fulfill the stigmatism condition.

3) Add coordinate breaks at the confocal points

After the conic confocal setup on axis is obtained, it is possible to calculate the position of the geometric focal points. To maintain the confocal condition during tilting the surfaces, the surfaces should be tilted around the geometric focal points. For instance, in a TMA system with one parabolic mirror and two elliptical mirrors as in Figure 3-9, the first confocal point is called F_1 , which is the focal point of the parabolic mirror and the first geometric focal point of the second mirror. The second confocal point F_2 is the second focal point of the second mirror and the first focal point of the third mirror. Then the sharp image will locate at the second focal point F_3 of the third mirror. The coordinate breaks are added at the two confocal points F_1 and F_2 . The second mirror can be tilted by tilting the coordinate break (CB2) at the point F_1 , and the third mirror can be rotated by tilting the coordinate break (CB3) at the point F_2 . Since in conic-confocal method, the stop is normally located before the first mirror, there is another coordinate break (CB1) added before the first mirror to decenter the stop. Since the first mirror is parabolic, the shift of the stop only decenters the field, but the rays of the central field are still parallel to the surface axis, which will be perfectly focused to the first confocal point F_1 . The locations of the confocal points and the coordinate breaks are illustrated in Figure 3-9.

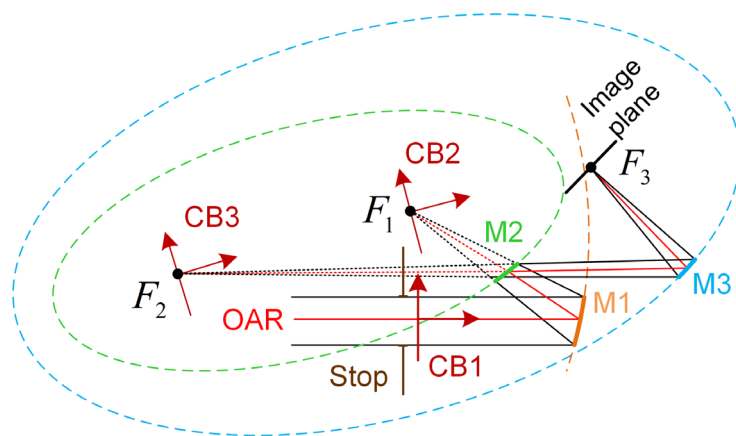


Figure 3-9 Locations of the coordinate breaks in a conic-confocal setup

4) Shift and tilt the mirrors to correct linear astigmatism

As mentioned in the third step, the first mirror is only decentered. The second and third mirror are tilted around the confocal points. There are two options to shift and tilt the mirrors. The first one is to shift the first mirror and tilt the second mirror with certain value and avoid obscuration of the ray bundles on M1 and M2. The

tilt of the third mirror is calculated according to the condition in Eq. (3-4). After the first mirror and the second mirror are moved off-axis, the incident angles and local magnifications of the first two mirrors are obtained. The local magnification of the first mirror is zero since the object is at infinite distance. The incident angles of the first two mirror are obtained by the ray direction of the OAR and the normal vector of the intersection point on the surface. As it is known in an elliptical conic section, the sum of the distances from a point to the two focal points, which means the sum of l and l' , equals the length of the major axis. In a hyperbolic conic section the absolute value of the difference between l and l' equals the length of the major axis. This relation of the lengths gives one equation. With law of cosines, it is possible to obtain the relation between the lengths l , l' and the incident angle, which gives the second equation. Therefore, including Eqs. (3-4)-(3-5), it is possible to solve the four unknown parameters m_3 , l_3 , l_3' , and i_3 with four equations. The incident angle can be converted into the tilt angle of the surface. Thus, it is possible to calculate the tilt angle of the third mirror, which fulfills the linear astigmatism vanishing condition as Eq. (3-4). The second option is to shift the first mirror and tilt the second mirror linearly. Every step is considered as a new system, and the tilt of the third mirror is calculated according to the condition to vanish linear astigmatism.

5) Evaluate obscuration

Every intermediate system obtained from step 4 should be evaluated for the obscuration condition. Only when the system is obscuration free, it will be saved as an initial setup. The main criterion is to evaluate the position of the intersection points on the surfaces. When the intersection points on one surface are not inside any other ray bundles, it means no ray bundle is truncated by the surface. For a design with certain FOV, the boundary fields in y direction should be added for the evaluation. The details for the obscuration evaluation are introduced in the following sections.

6) Save the system

The systems without obscuration will be saved. Therefore, there are more than one solution from the same on-axis setup. They all have one perfectly imaged point in the center of the field of the FOV. The linear astigmatism vanishes. However, since the tilt angle of the third mirror is calculated, the direction of the tilt

cannot be predicted. Thus, the designer can select one design as the initial setup from all the results, which has relatively small residual aberrations and proper system size.

As an example, the on-axis setup of a TMA system is designed with the entrance pupil diameter of 80mm, focal length of 325 mm and free working distance of 200 mm, and the FOV of $2^\circ \times 2^\circ$. The on-axis setup is designed following the step 1) to 3) mentioned above. Two results with different tilt angles of the second mirror are shown in Figure 3-10. The decentering of the first mirror is 200mm for both cases. The second mirror is tilted with -20° for the case in Figure 3-10 (a) and 10° for the case in Figure 3-10(b). Then the solution of the tilt angle of M3 is 1.281° for the first case in Figure 3-10(a) and 2.480° for the second case in Figure 3-10(b). It is seen from the spot diagram that the central field is imaged to a sharp point, and the fields near the central field only suffer from coma. Linear astigmatism vanishes. However, due to the different magnifications in x- and y-direction, the anamorphism and the sine-condition are not comfortable.

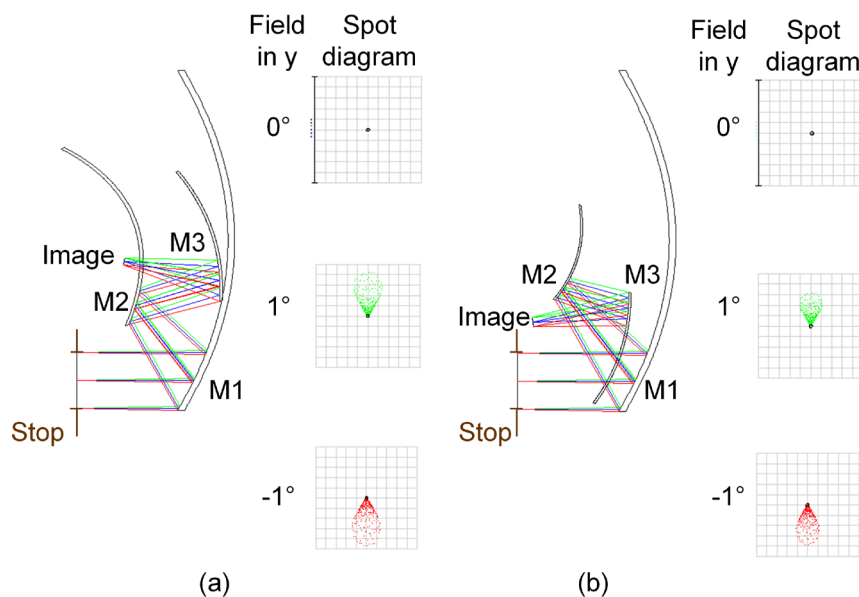


Figure 3-10 Example for conic-confocal method

This method works perfectly in obtaining the nodal point in the center of the FOV. However, it can be seen from Figure 3-10 that the conic surfaces are off-axis used. If we only consider the off-axis used part, it is so called the quasi-freeform surface. When a conic surface is off-axis used, the effect can be seen as a freeform surface, which will be explained in detail in the following sections. If the

vertex of the conic surface is still located at the rotational symmetry center, when freeform surfaces are added, the off-axis used part will locate at the boundary of the freeform surface. During optimization, the basic shape parameter and the lower order terms of the freeform surface will influence the bending of the off-axis used part tremendously, which makes the surface very sensitive to small change of the parameters. This is one of the inconvenience of this method. One possible method to overcome the shortcoming is to shift the vertex to the intersection point of the OAR. Then the conic surface will be converted into a freeform surface, based on which the further optimization with additional freeform polynomials will be less sensitive. Another possibility is to design the initial system with only spherical surfaces since the vertex can be an arbitrary point on a spherical surface, for which a completely different design method called Gaussian brackets method is proposed. This method is introduced in the next section.

3.3.2 Gaussian brackets method

It is known that the main idea to design an initial system is to reduce the aberrations before adding freeform surfaces and numerical correction. For a non-rotationally symmetric system, the distribution of aberrations are also non-rotationally symmetric. It is known that the central field of the rotationally symmetric system only suffers from spherical aberration. For off-axis systems such as TMAs and HMDs, the tilt of each component introduces field-independent aberrations, such as field-constant coma and astigmatism. Therefore, if the total contribution of field-constant aberrations does not vanish, the central field suffers from large aberrations. In this case, the FOV is far away from the nodal points, so that the system suffers from large aberrations. Therefore, for initial system design of off-axis systems, the main idea is to optimize the aberrations of the central field in order to move the nodal point in the center of the FOV.

For special designs as Scheimpflug systems, the optical components are still centered. Thus the system does not suffer from field-constant aberrations. Instead, the large shift of object distance leads to large variation of aberrations over the FOV. Even the spherical aberration is field-variant in a Scheimpflug system. Thus, the main idea is to uniform the aberrations over the FOV to obtain uniform system performance.

The already existing initial system design methods mentioned in Section 2.1 deal with either specialized system types or limited number of surfaces. In addition, they provide limited ability in the analysis of the system during the design procedure due to extended FOV and broadband illumination. Therefore, one of the aims of the thesis is to propose a method, which has no limitation in the system type and the number of surfaces. This method is directly aberration related. Thus it also can be used to analyze the residual aberrations in the system and provide a feedback for further structural modification or adding freeform surfaces.

In Section 2.4, the Gaussian brackets formulated by Tanaka is introduced. The four GGC's as in Eqs. (2-30)-(2-33) are defined to formulate the paraxial theory of optical systems. Therefore, the paraxial ray tracing data and some first-order properties can be derived fast and analytically in matrix computation using the GGC's. The paraxial ray tracing data provides the possibility to derive the Seidel aberration coefficients. This method was used to design initial configuration of centered imaging systems based on Seidel aberration theory [38]. In this thesis, the Gaussian brackets method is extended from the paraxial environment to the paraxial environment based on NAT. The main idea is to derive the aberrations of the selected fields and the first-order properties analytically. By solving nonlinear equations, the solution for the system data is obtained to achieve minimum aberrations of the selected fields.

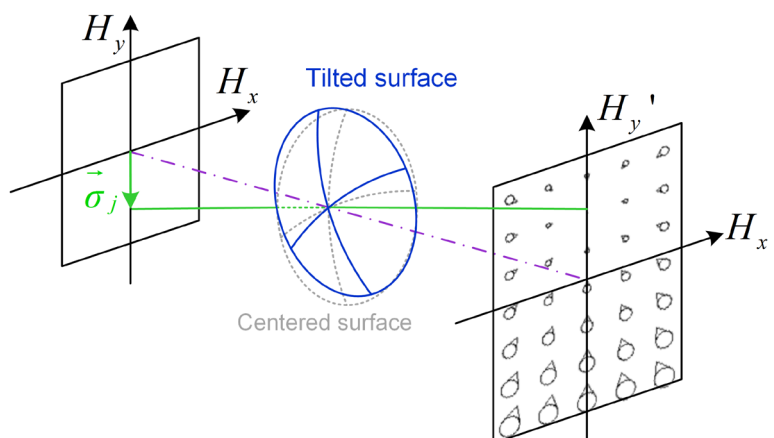


Figure 3-11 Shift of nodal point of a single surface by tilting the surface

According to nodal aberration introduced by Thompson as mentioned in Section 2.3, the wave aberration for non-rotationally symmetric systems is built upon a vectorial formulation. The decenter contribution of the field is described by a displacement vector of each surface. The field shift vector shifts the nodal point

away from the central field for the aberration contribution of each surface. The shift of nodal point of a single surface is illustrated in Figure 3-11. The surface is tilted around the x-axis, which means a field shift vector $\vec{\sigma}_j$ direction is introduced in y. The distribution of coma is shown in the image plane of the surface. It is seen that the green ray stands for the chief ray of the field, which has the same normalized field height as $\vec{\sigma}_j$ and corresponds to the nodal point. Therefore, the nodal point is shifted from the origin point to this field.

The distribution of coma is shown here as an example. The nodal point of coma, astigmatism, focal plane of medial astigmatism, and distortion of a single surface is the same. Therefore, it is impossible to shift the nodal point back to the center of the FOV with only one surface. By using more than one tilted surface, it is possible to obtain the solutions which lead to nodal points at the selected fields.

In off-axis systems, the solutions of the Gaussian brackets method contain the field shift vector of each surface. The value of the field shift vector should be converted to the tilt angles of the surfaces, which can be used to construct the setup in the design software.

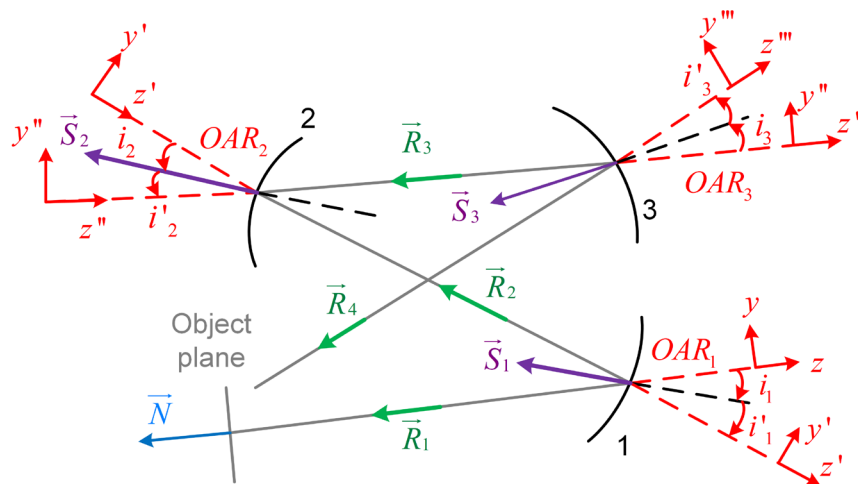


Figure 3-12 Tilt angles and real-ray-based vectors of plane-symmetric mirror system

In plane-symmetric systems, the surfaces are only tilted around x-axis. For a plane-symmetric reflective system as in Figure 3-12, the tilt angle of the j^{th} surface around the vertex point is equal to the incident angle i_j of the OAR, which is also equal to the angle between \vec{R}_j and \vec{S}_j . After the surface, the coordinate should be tilted by reflection angle i'_j to keep the optical axis along the optical axis ray.

According to the real-ray-based normal vectors as in Eqs. (2-20)-(2-22), the tilt angles of a plane-symmetric reflective system can be derived as

$$i_j = i'_j = \arctan\left(-\frac{SRM_j}{SRN_j}\right). \quad (3-11)$$

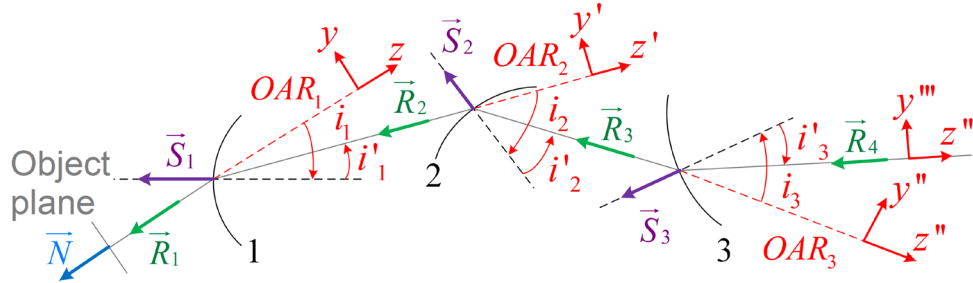


Figure 3-13 Tilt angles and real-ray-based vectors of plane-symmetric refractive system

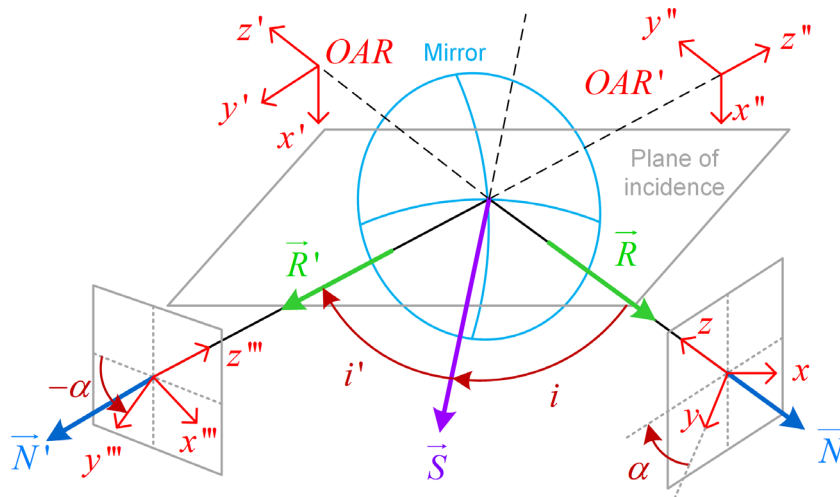


Figure 3-14 Tilt angles and real-ray-based vectors of a mirror tilted in both x- and y- direction

In a plane-symmetric refractive system as in Figure 3-13, the first coordinate break should also be tilted with the angle i_j , which equals the incident angle of the OAR. The incident angle is calculated following the same relation as Eq. (3-11). The second coordinate break after the surface should be tilted with the refractive angle, which is calculated by refraction law as

$$i'_j = -\arcsin\left(\frac{n_{j-1}}{n_j}\sin(i_j)\right). \quad (3-12)$$

For a non-symmetric system with off-axis components, the field shift vector contains components in both x- and y-direction. A tilted mirror in Figure 3-14 is shown as an example.

The first step is to rotate the coordinate around z-axis before the surface with an angle of α , then x-axis is perpendicular to the plane, where the reflection takes places. The second step is similar to plane-symmetric case that the coordinate before the surface should be tilted around x-axis with an angle of i , which is the incident angle of the OAR. After the surface, the coordinate is tilted with the reflection angle i' to keep the z-axis along the OAR. Since the field shift vector of each surface is calculated according to the real-ray-based vectors in the local coordinate of the object (or intermediate images) as reference, at the end the coordinate should be tilted around z-axis by an angle of $-\alpha$ to keep the x-y axis of the intermediate image the same as the field coordinate in the object plane. Then the conversion of Euler angles according to the real-ray-based vectors of the next surface is correct.

Thus, the tilt angles of the coordinates of the j^{th} surface are given in four steps.

- 1) Tilt the coordinate around z-axis with the angle of α_j before the surface.

When the value of SRM_j is not zero:

$$\alpha_j = \arctan\left(-\frac{SRL_j}{SRM_j}\right). \quad (3-13)$$

When the value of SRM_j is zero:

$$\alpha_j = -90^\circ. \quad (3-14)$$

- 2) Tilt the coordinate around x-axis with the angle of i_j before the surface.

When the value of SRM_j is not zero:

$$\text{if } SRM_j < 0, \quad i_j = \arctan\left(\frac{\sqrt{SRL_j^2 + SRM_j^2}}{SRN_j}\right), \quad (3-15)$$

$$\text{if } SRM_j > 0, \quad i_j = -\arctan\left(\frac{\sqrt{SRL_j^2 + SRM_j^2}}{SRN_j}\right). \quad (3-16)$$

When the value of SRM_j is zero:

$$i_j = -\arctan\left(\frac{SRL_j}{SRN_j}\right). \quad (3-17)$$

3) Tilt the coordinate around x-axis with the angle of i'_j after the surface are as

$$i'_j = i_j \quad (\text{Reflective}), \quad (3-18)$$

$$i'_j = -\arcsin\left[\frac{n_{j-1}}{n_j}\sin(i_j)\right] \quad (\text{Refractive}). \quad (3-19)$$

4) Tilt the coordinate around x-axis with the angle of $-\alpha_j$ after the surface.

In off-axis systems and anamorphic systems, due to the incident angle of the OAR at each surface, the focal powers are different in tangential and sagittal planes. Therefore, Coddington equations are applied as an additional constraint in the method to control the astigmatism of the central field more directly. If the chief ray incident angle at a surface is presented by i and the refractive angle is i' , the Coddington equations are shown as in Eq. (3-20) for the sagittal imaging and Eq. (3-21) for the tangential imaging [6].

$$\frac{n'}{s'} - \frac{n}{s} = c[n'\cos(i') - n\cos(i)], \quad (3-20)$$

$$\frac{n'\cos^2(i')}{t'} - \frac{n\cos^2(i)}{t} = c[n'\cos(i') - n\cos(i)], \quad (3-21)$$

where s and t denote the object distance of a surface in sagittal and tangential planes, s' and t' denote the image distance of a surface in sagittal and tangential planes along the OAR, n and n' denote the refractive index before and after the surface, and c denotes the curvature of the surface. The local focal power Φ_{skew} of the OAR of each surface is defined as

$$\Phi_{skew} = c[n'\cos(i') - n\cos(i)]. \quad (3-22)$$

For each surface, the object distance and image distance respectively in sagittal and tangential plane are derived as

$$s' = \frac{n'}{\frac{n}{s} + \Phi_{skew}}, \quad (3-23)$$

$$t' = \frac{n' \cos^2(i')}{\frac{n \cos^2(i)}{t} + \Phi_{skew}} \quad (3-24)$$

Therefore, using Eqs. (3-23)-(3-24) and the distance between the surfaces, for a system with the number of surfaces as k , the total image distance s'_k and t'_k in tangential and sagittal planes can be derived analytically.

In this method, if the solutions are obtained to minimize the focal plane of medial astigmatism of the central field, it only characterizes one field point. It is known that the focal plane of medial astigmatism contains the field curvature part. Therefore, one more condition based on the Petzval sum of the system is added as Eq. (3-2) to correct the field curvature. This condition also reduces one unknown parameter, since the one of the curvatures can be represented by the refractive indices and the curvatures of other surfaces.

Table 3-4 Nonlinear functions in the optimization procedure

Term	Function
Spherical aberration	$\sum_j W_{040j}$
Coma in x	$\sum_j W_{131j} (H_x - \sigma_{jx})$
Coma in y	$\sum_j W_{131j} (H_y - \sigma_{jy})$
Astigmatism (axis in 0°)	$\frac{1}{2} \sum_j W_{222j} [(H_x - \sigma_{jx})^2 - (H_y - \sigma_{jy})^2]$
Astigmatism (axis in 45°)	$\sum_j W_{222j} [(H_x - \sigma_{jx})(H_y - \sigma_{jy})]$
Focal plane of medial astigmatism	$\sum_j \left(W_{220j} + \frac{1}{2} W_{222j} \right) [(H_x - \sigma_{jx})^2 + (H_y - \sigma_{jy})^2]$
Distortion in x	$\sum_j W_{311j} [(H_x - \sigma_{jx})^2 + (H_y - \sigma_{jy})^2] (H_x - \sigma_{jx})$
Distortion in y	$\sum_j W_{311j} [(H_x - \sigma_{jx})^2 + (H_y - \sigma_{jy})^2] (H_y - \sigma_{jy})$
Focal length	$f' - \frac{1}{\sum_k C_k}$
Coddington equations	$s'_k - t'_k$
Other first-order properties	For instance: back focal length S'_F

Therefore, with the paraxial ray tracing data obtained by GGC's, a series of nonlinear functions can be derived based on the NAT, the Coddington equations, the focal length, and other first-order properties of the system. The functions are given as in Table 3-4.

The design procedure of the Gaussian bracket method is given in the following steps.

1) Define the number of surfaces including the pupils

The number of surfaces should include the object plane, the pupil and its conjugates (intermediate pupils), and the image plane. For a system with infinite object, the entrance pupil is regarded as the first surface.

2) Define initial ray data

The paraxial ray tracing data are derived based on the GGC's in the matrix approach. Thus, the initial ray data of the marginal ray and chief ray should be defined according to the specifications. Since the system is regarded as centered in the paraxial model, only the ray heights and ray angles in the tangential plane should be defined. They can also be defined with the system parameters analytically. For instance, when the system has a finite object distance, the initial chief ray angle is defined using the field height and the distance from the object plane to the entrance pupil.

3) Define stop position

Since the pupils and the intermediate pupils are considered as surfaces with no power in the system, the reduced distances consist of the distances between the real surfaces and the pupils. It provides the possibility to define the location of the stop at a real surface location. If the distances from the real surface to its two pupils are both zero, the stop is defined at the surface location. For some systems, the stop location is not fixed. After the solutions are obtained, the stop can be defined at any pupil or intermediate pupil location in the system. For systems with the stop before the first surface, the entrance pupil is defined as the stop.

4) Apply the equation of Petzval curvature vanishing to present one surface curvature by the other curvatures

In a system with certain number of surfaces, the curvature of one surface can be represented by the refractive indices and the curvatures of other surfaces using Eq. (3-2). Then one unknown parameter is reduced.

5) Define Gaussian brackets and derive the Generalized Gaussian constants

After the number of surfaces is defined, the curvature, the reduced distance, and the refractive indices are defined. Some of the parameters are variables, and the others are already known. For instance, the refractive indices can be defined with values, and the curvature is zero for each pupil. If the stop is located at a real surface, the reduced distances before and after the real surface are also zero. With the system parameters, the GGC's are derived analytically.

6) Fast on-axis paraxial ray trace by using GGC's

When the initial ray data are defined, and the GGC's are derived, the paraxial ray trace data on each surface can be obtain in the matrix approach.

7) Derive the Seidel aberration coefficients using the on-axis paraxial ray tracing data

Using the paraxial ray trace data obtained in the last step, the Seidel aberration coefficients W_{klm} are derived using the equations in Table 2-1.

8) Derive focal length and other first-order properties by using GGC's

It is mentioned in Section 2.4 that the first-order properties can be represented by the GGC's. Therefore, the focal length is derived using Eq. (2-45) and the back focal length is defined using Eq. (2-44).

9) Derive the primary aberrations of the selected field by adding the real-ray-based field decenter vectors as variables

In this step, field decenter vectors are defined as variables for tilted surfaces. For the object plane, pupils, centered surfaces, and the image plane, the field decenter vectors are defined as zero. Therefore, the primary aberrations as in Table 3-4 are derived using the Seidel coefficients obtained in step 7) and the field decenter vectors based on NAT. For an off-axis system, normally the selected field is the central field. Thus the five primary aberrations of the central field are derived. For a Scheimpflug system, the goal is a good uniformity of the performance. It is not realistic to optimize all the aberrations for different object distances in the initial configuration. Therefore, several fields are selected along the object distance, and only some of the aberrations of the selected fields are optimized for the initial setup. For instance, spherical aberration and distortion of individual selected field are selected. The keystone distortion of the whole FOV cannot be avoided.

10) Derive the sagittal and tangential image distances.

This step is only for off-axis systems. Using the defined system parameters, the image distances of the central field can be derived in sagittal and tangential planes according to the Coddington equations as Eqs. (3-20)-(3-24).

11) Obtain the analytical functions

In this step, all the aberrations derived in step 9) are defined as analytical functions. The first-order properties should equal to the target value. Thus the difference between the focal length or the other first-order parameters and their target values can also be defined as functions. The image distances in sagittal and tangential planes obtained by Coddington equations should be the same after optimization. Thus the difference between them is also defined as a function. The value of all the functions should be minimized to obtain the initial system.

12) Minimize the functions by nonlinear least-squares solver

The nonlinear least-squares solver in Matlab is used to solve the nonlinear equations. The optimization toolbox in Matlab provides the possibility of nonlinear fitting optimization. The working principle of this solver is that, when a group of functions are defined with the same variables, it solves the fitting problem to obtain a group of solutions, which leads to the minimum value of a series of the nonlinear functions. Here, the variables are the system parameters. The functions are the aberrations and the first-order properties of the system. Therefore, the nonlinear least-squares solver provides an optimization procedure to obtain a group of system data, which leads to minimum aberrations and fulfills the first-order properties. In the nonlinear least-squares solver, the starting value and boundary values should be given for each variable. The designers can set proper boundary conditions to obtain a physical setup. The range of tilt angles can also be controlled by the boundary values to avoid obscuration.

13) Convert the solutions into system data and check the performance of the system in the design software

Since the solutions are the curvature, field shift vectors, and reduced distances for both real surfaces and pupils, they must be converted into the data, which can be used as input in a design software, such as radius of curvature, tilt angles of the coordinate breaks, and distances between real surfaces. The conversion of

tilt angles are mentioned. After the system data are inserted, the system performance and obscuration are checked in the design software.

Although this method works for both refractive and reflective systems with unlimited number of surfaces, it also has certain limitations. The first limitation is that the number of nonlinear functions is limited by the computational capability of the computer. The complexity of the system will influence the memory space that each function takes. The second limitation is that the nonlinear least-squares solver provides a local minimum searching approach. The boundary values of the unknown parameters should be defined according to the pre-defined geometry of the system. If the solver cannot obtain a good solution, the boundary and starting values should be re-adjusted until a good initial setup is obtained. The method will be demonstrated in Chapter 4 with the TMA systems as an example. The initial setups of the Yolo system and the Scheimpflug system in Chapter 4 are both obtained using this method. The strategies to select aberrations and fields are different for those systems, which will be discussed.

3.4 Obscuration

In the design of off-axis systems, obscuration is always one of the problems. For the system performance and first-order properties, it is possible to define the error functions directly and optimize the error functions. However, obscuration cannot be directly defined in the error function. Therefore, there are some methods to control the obscuration indirectly.

Off-axis systems can be classified into two types. One is the plane-symmetric off-axis system, in which the components are off-axis only in the tangential plane. The other type is the non-symmetric off-axis system, in which the components are off-axis in both tangential and sagittal planes.

The main idea to avoid obscuration is to avoid any truncation of the ray bundles by other surfaces. For plane-symmetric off-axis systems, the position of the surfaces and the ray bundles are considered only in one plane. If there is obscuration, it will be seen that parts of the ray bundles are truncated by the other surface in the tangential plane, which is more obvious compared with the non-symmetric case. For non-symmetric system, the layouts in tangential plane and sagittal planes do not give the complete information of the geometry. For instance, if we

take the plane-symmetric system as a special case of the general non-symmetric system, although the surfaces occur in the other ray bundles in the sagittal layout, the system is still obscuration free. Therefore, currently we only discuss the techniques to avoid obscuration in plane-symmetric off-axis systems.

The TMA system is taken as an example to show the often used methods to avoid obscuration. For off-axis TMA systems, there are two types of geometry. One is called the zigzag structure. The mirrors are always tilted to bend the OAR towards the same direction in y -axis as shown in Figure 3-15(a). The other one is called folding structure as in Figure 3-15(b). The tilt angle around x -axis of all the mirrors are of the same sign. Therefore, the OAR is folded and goes through the same space for several times. The folding structure is more compact compared with the zigzag structure, since the zigzag structure requires relatively large diameter in the y direction.

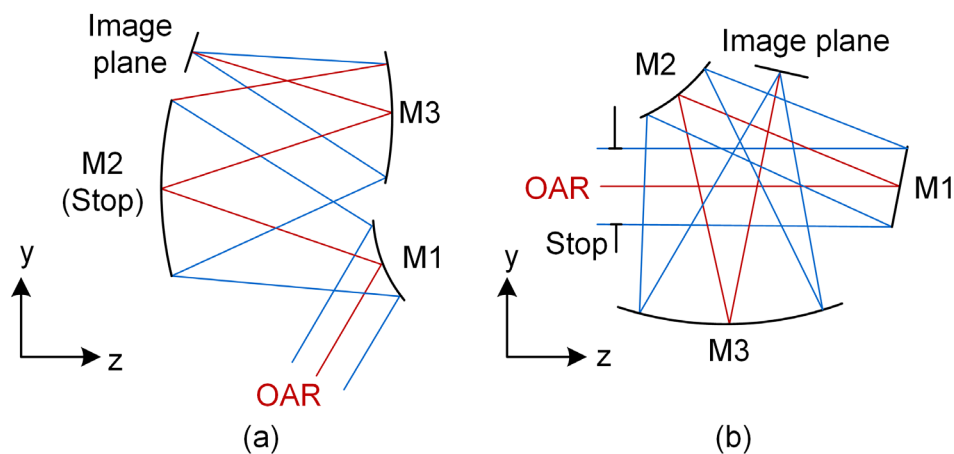


Figure 3-15 Different geometric structure of TMA systems. (a) Zigzag structure; (b) Folding structure.

For the zigzag structure as in Figure 3-16, the traditional way to avoid obscuration during optimization is to add some virtual planes at certain positions. For instance, if the distance between $M1$ and $M2$ is d_1 , and the distance between $M2$ and $M3$ is d_2 , one virtual plane (VP1) is added before $M1$ with a distance of d_1 , and another virtual plane (VP2) is added after $M3$ with a distance of d_2 . Then the two virtual planes will have intersection points with the rays. To avoid obscuration by $M2$, the intersection points of VP1 should have smaller ray heights in y -axis compared with the intersection points on $M2$. Therefore, if the system consists of only one field, the upper marginal ray height in y -axis on VP1 should be smaller

than the lower marginal ray height on M2, which means point A is below point A' as in Figure 3-16. Similarly, the ray height of the upper marginal ray on M2 should be smaller than the ray height of the lower marginal ray on VP2 in y-axis, which means point B is below point B'. To avoid obscuration of M1 and M3, each of the two surfaces should not truncate the rays reflected by the other one. Therefore, it means the upper marginal ray height on M1 should be smaller than the lower marginal ray height on M3 in y, which means point C is below point C'. The difference between the ray heights can be defined in the merit function and the value can be optimized according to the mechanical constraints. When the system has certain FOV, the ray heights of the marginal rays are replaced by the ray heights of the coma rays of the boundary fields in y direction.

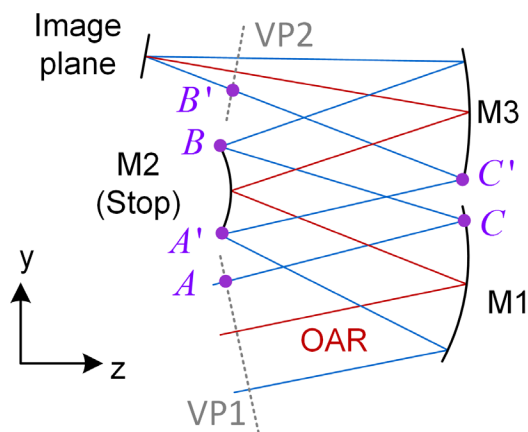


Figure 3-16 Virtual planes in a TMA system to avoid obscuration

However, the method to add virtual planes and optimize the position of the intersection points of the rays in y direction works only for the zigzag structure. If the system has a folding structure as in Figure 3-15(b), the orientation of the surface is arbitrary. By only controlling the difference of the ray heights in x- and y-direction, the obscuration cannot be avoided. The relation between the surfaces and the ray bundles should be considered in a more general point of view. Since the main idea is to avoid truncation of rays, it means that none of the points on a surface should appear within the other ray bundles.

In Figure 3-17, part of a multi-plane reflective system is shown. The system contains some off-axis surfaces, which are tilted in the tangential plane. To show the relation of the surfaces and the ray bundles more clearly, the system layout is drawn as a zigzag structure, but it can also be applied to folding structure. If only

the central field is taken into consideration, the intersection points of the upper marginal ray on the surfaces are the points A, B, C, D, and E, while the intersection points of the lower marginal ray are the points A', B', C', D' and E'. Each pair stands for the boundary of a surface. For example, C and C' are the boundary points of the j^{th} surface. Between two surfaces, the ray bundle is formed by four points, for instance, the ray bundle between the $(j-2)^{\text{th}}$ surface and the $(j-1)^{\text{th}}$ surface is formed by points A, B, B' and A'. If the system has a certain FOV, the four points will be extended to the intersection points of coma rays of the boundary fields. The polygon formed by the boundary intersection points of two neighboring surfaces includes all the ray bundles. Therefore, the main idea to avoid obscuration is to keep the points on a surface out of the polygon formed by other surfaces. For instance, for an arbitrary surface in a system such as the j^{th} surface in Figure 3-17, the points of j^{th} surface should be out of the polygon formed by the $(j-1)^{\text{th}}$ surface and the $(j-2)^{\text{th}}$ surface, which means the polygon AA'B'B. It should also be out of the polygon formed by $(j+1)^{\text{th}}$ surface and the $(j+2)^{\text{th}}$ surface, which is the polygon DD'E'E.

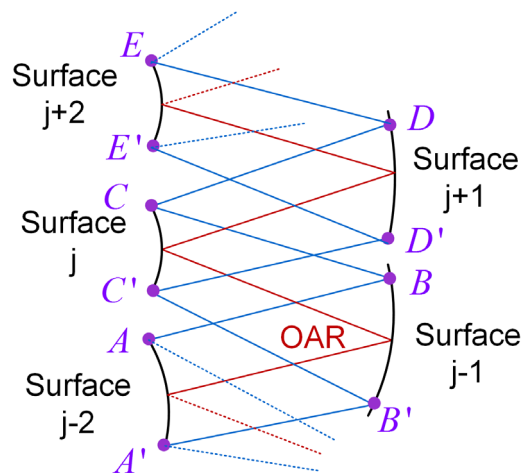


Figure 3-17 Relation of surfaces and ray bundles to avoid obscuration

For the conic-confocal method in Section 3.3.1, the shift of the first mirror and the tilt of the second mirror is arbitrary. The designer can try to avoid obscuration of the first two mirrors by setting proper values of the shifts and tilts. However, the tilt angle of the third mirror is calculated according to the condition to vanish linear astigmatism. Thus, the value cannot be defined to obtain obscuration free. After the shifts and tilts are obtained for the mirrors, the obscuration condition should be checked.

Based on the idea mentioned above, two boundary points and the intersection point of the OAR on the surface are taken into consideration. If those three points of each surface are all out of the polygons formed by other surfaces, the system is obscuration free. The criterion to check whether one point is inside a polygon is shown in Figure 3-18. When the point E is inside the polygon ABCD as in Figure 3-18(a), if the each points of the polygon is connected with the point E, the sum of the four angles ω_1 , ω_2 , ω_3 and ω_4 of between the lines is always 360° . If the point E is outside of the polygon as in Figure 3-18(b), the sum of the angles is smaller than 360° . Therefore, after the three points of every surface are checked, the system without obscuration is saved as an initial system in the conic-confocal method.

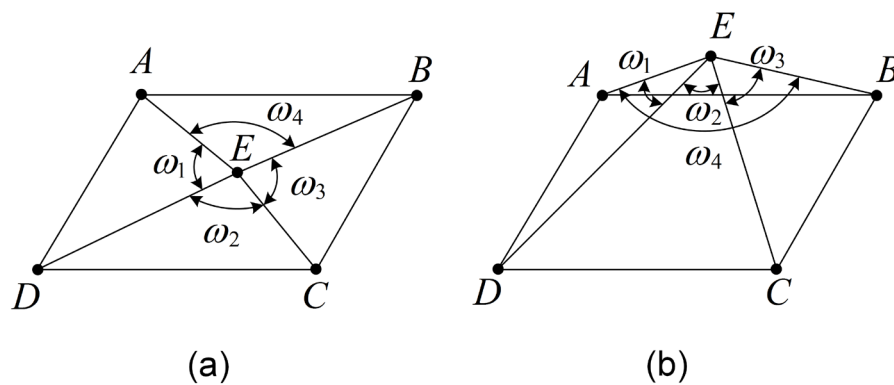


Figure 3-18 Criteria to check the position of a point (a) in a polygon; (b) outside of the polygon

This criterion mentioned above is for checking the obscuration. However, it is not an error function, which can be optimized during the design process. In the research of C. Xu, the distance from the point to the edges of the polygon is defined as an error function for optimization [39]. Since the system geometry of off-axis system can be very complicated, the relation of a surface and the polygon formed by other surfaces are discussed in different cases [39].

3.5 Aberrations

As mentioned, the aberrations in the non-rotationally symmetric system are represented in vectorial form. In this section, the vectorial aberrations of the basic shape and the deformation from the basic shape are introduced. It is known that

the surface shape starts from a basic spherical shape. With aspherical deformation, it is extended to a conic or aspherical surface. With the freeform deformation, it is further extended to a freeform surface. As mentioned in Section 2.6, the biconic surface is used as a basic shape of the surface representations due to its benefit of correcting astigmatism. Therefore, the aberrations generated by the biconic surface is of interest to analyze the performance of the system. By understanding the aberrations in the system, the design strategy and surface selection rules can be generated.

3.5.1 Primary coefficients

The vectorial aberration representation is given by the NAT, which also includes the tilt effect of surfaces. For the spherical surface shape, the primary aberrations are given as Eq. (2-18).

Therefore, for a certain object distance, the spherical aberration is constant along the FOV. The total spherical aberration of the system is the sum of the spherical aberration of each surface. Therefore, the spherical aberration is influenced by the bending of the surface, the refractive index of the material and the distance between surfaces. When designing the initial setup of an off-axis system, one of the most difficult tasks is to correct coma and astigmatism of the central field simultaneously. With only spherical surfaces, it is known from the Seidel aberration theory that the Seidel coefficients W_{klm} of the primary aberrations are coupled. For an off-axis surface, the other parameter, which influences the value of the aberration, is the tilt of the surface.

The vectorial aberration representation of coma coefficient of the whole system is given as

$$\begin{aligned} W_{Coma} &= \sum_j W_{131j} (\bar{H} - \bar{\sigma}_j) = \bar{H} \sum_j W_{131j} - \sum_j W_{131j} \bar{\sigma}_j \\ &= \bar{H} W_{131}^{sum} - \sum_j W_{131j} \bar{\sigma}_j. \end{aligned} \quad (3-25)$$

It is seen from Eq. (3-25) that the total coma of the off-axis system with spherical surfaces is formed by two parts. One is the field-linear part, which is the same as the centered system. The second part is the field-constant part, which purely depends on the field shift vectors of the surfaces. For the central field, the total coma equals the field-constant part in Eq. (3-25) as

$$W_{Coma}^{\bar{H}=0} = -\sum_j W_{131j} \bar{\sigma}_j = \begin{pmatrix} \sum_j W_{131j} \frac{SRL_j}{\bar{i}_j} \\ \sum_j W_{131j} \frac{SRM_j}{\bar{i}_j} \end{pmatrix} = \begin{pmatrix} \sum_j W_{131j} \frac{SRL_j}{\bar{h}_j c_j + \bar{u}_j} \\ \sum_j W_{131j} \frac{SRM_j}{\bar{h}_j c_j + \bar{u}_j} \end{pmatrix}. \quad (3-26)$$

From Eq. (3-26), it can be seen that coma of the central field is determined by the Seidel coefficient of W_{131} , the paraxial chief ray incident angle \bar{i} of the centered model as in Figure 2-8(a), and the real ray direction cosines SRL and SRM in x and y directions of the OAR, which corresponds to the tilt of the surface. If radii of curvature and the distances between the surfaces are fixed, the sign of the coma value of each surface is determined by the tilt angle of the surface. If the direction cosines of the OAR lead to the same sign of coma value of all the surfaces, it is impossible to correct coma of the central field. The whole FOV is dominated by a large field-constant coma, which equals the total coma of the central field. The strategy to compensate the field-constant coma will be shown in Chapter 4 in the Yolo telescope example.

It is known from the Coddington equations that the astigmatism of the central field of an off-axis system is determined by the incident angles of the OAR, which lead to different the focal power in tangential and sagittal planes. The Coddington equations also correspond to the astigmatism in NAT. The incident angles in Coddington equations correspond to the field shift vectors in NAT. The astigmatism (in 0° axis) of the central field is given as

$$W_{Astig\ 0^\circ}^{\bar{H}=0} = \frac{1}{2} \sum_j W_{222j} (\sigma_{jx}^2 - \sigma_{jy}^2) = \frac{1}{2} \sum_j W_{222j} \left(\frac{SRL_j^2 - SRM_j^2}{\bar{i}_j^2} \right). \quad (3-27)$$

It is seen in Eq. (3-27) that only the absolute values of SRL and SRM can influence the sign of astigmatism. The sign of SRL and SRM individually will not influence the astigmatism. Therefore, the sign of the incident angle of the OAR will not influence the value of the field-constant astigmatism. For a plane-symmetric off-axis system, the astigmatism value of a surface is the same when it is tilted clockwise or counterclockwise with the same angle around the x-axis. Since in this case $SRL = 0$ and the value of SRM^2 is always positive, the sign of W_{222} / \bar{i} should not be the same of all the surfaces. Otherwise, the astigmatism cannot be corrected for the central field.

Since the Seidel coefficients W_{222} of astigmatism and W_{131} of coma are coupled, it is difficult to obtain the tilt angles of spherical surfaces, which could correct coma and astigmatism of the whole system simultaneously, especially when the range of the tilt angle is limited to avoid obscuration. Therefore, in some cases with high specification, it is unrealistic to optimize all the aberrations of the initial setup. Only some of the aberrations are derived as the nonlinear functions in the Gaussian brackets method.

It is known that aspherical deformation is added on the basic spherical shape to correct aberrations to some extent. The aberrations generated by the asphere can be decomposed into one part generated by the basic spherical shape and the other part generated by the aspherical deformation. If the aspherical representation is expanded up to the 4th order, the Eq. (2-48) is written as

$$z_{asphere} = \frac{1}{2}c(x^2 + y^2) + \frac{1}{8}c^3(x^2 + y^2)^2 + \frac{1}{8}\kappa^3(x^2 + y^2)^2 + a_4(x^2 + y^2)^2. \quad (3-28)$$

The first two terms of Eq. (3-28) are the same as the expansion of a spherical surface up to the 4th order. The Seidel aberration theory is derived based on the expansion of a spherical surface up to the 4th order. Thus the aberrations generated by the aspherical deformation correspond to the last two terms of Eq. (3-28). When the pupil is located at the surface, the relation between the normalized pupil vector in Figure 2-4 and the radial aperture vector in Figure 2-10 of the surface aperture is written as

$$\vec{\rho} = \frac{\vec{r}}{h}, \quad (3-29)$$

where h denotes the paraxial marginal ray height on the surface. The contribution of the aspherical deformation at the pupil is given by

$$\Delta W = \Delta(n) \left(\frac{1}{8}\kappa^3 + a_4 \right) h^4 \left[\left(\frac{x}{h} \right)^2 + \left(\frac{y}{h} \right)^2 \right]^2 = \Delta(n) \left(\frac{1}{8}\kappa^3 + a_4 \right) h^4 (\vec{\rho} \cdot \vec{\rho})^2, \quad (3-30)$$

where $\Delta(n)$ denotes the difference between the refractive index after and before the surface. When the surface is located away from the pupil, the normalized pupil vector is shifted by $\Delta\vec{h}$ due to the finite chief ray height \bar{h} on the surface as in Figure 3-19. The shifted normalized pupil vector is written as

$$\vec{\rho}_{shift} = \vec{\rho} + \Delta\vec{h} = \vec{\rho} + \frac{\bar{h}}{h} \vec{H}. \quad (3-31)$$

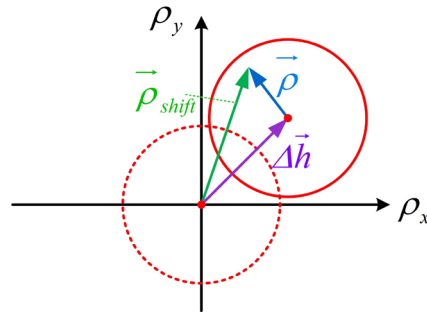


Figure 3-19 Pupil shift with finite chief ray height

The spherical aberration coefficient W_{040j}^{ASPH} of the j^{th} surface generated by the aspherical deformation is defined as

$$W_{040j}^{ASPH} = \Delta(n) \left(\frac{1}{8} \kappa^3 + a_4 \right) h^4. \quad (3-32)$$

By substituting the normalized pupil vector in Eq. (3-30) with the shift factor in Eq. (3-31), the primary aberrations generated by the aspherical deformation are derived and listed in Table 3-5.

Table 3-5 Primary aberration coefficients generated by the aspherical part of a surface away from the pupil in vectorial representation [14]

Aberration	Value
Spherical aberration	$W_{040}^{ASPH} (\bar{\rho} \cdot \bar{\rho})^2$
Coma	$4 \left(\frac{\bar{h}}{h} \right) W_{040}^{ASPH} (\bar{H} \cdot \bar{\rho}) (\bar{\rho} \cdot \bar{\rho})$
Astigmatism	$2 \left(\frac{\bar{h}}{h} \right)^2 W_{040}^{ASPH} (\bar{H}^2 \cdot \bar{\rho}^2)$
Focal plane of medial astigmatism	$4 \left(\frac{\bar{h}}{h} \right)^2 W_{040}^{ASPH} (\bar{H} \cdot \bar{H}) (\bar{\rho} \cdot \bar{\rho})$
Distortion	$4 \left(\frac{\bar{h}}{h} \right)^3 W_{040}^{ASPH} (\bar{H} \cdot \bar{H}) (\bar{H} \cdot \bar{\rho})$

It can be seen that when the asphere is away from the pupil, it generates all types of primary aberrations. However, coma and astigmatism are still coupled. Both of them are related with the value of the spherical aberration W_{040}^{ASPH} generated by the aspherical deformation, which limits the correction ability.

Therefore, it is impossible to decouple coma and astigmatism with rotationally symmetric components. Freeform surfaces provide the possibility to decouple

coma and astigmatism by introducing the polynomials corresponding to the aberration terms.

3.5.2 Zernike fringe freeform surface

Although aspheres and biconic surface provide certain ability to correct aberrations in non-rotationally symmetric systems, it is required to add higher order polynomials to further correct the residual aberrations. It is mentioned in Section 2.6 that the freeform deformation from the basic surface can be represented by different polynomials, which means different polynomials can describe the same surface sag. Therefore, we only use Zernike fringe polynomials to show how the aberrations are derived. For the other types of polynomials, the behavior is similar.

The relation between the normalized radial aperture coordinate \bar{r} of a Zernike fringe surface at the pupil and the radial coordinate ρ of the normalized pupil vector in the wave aberration expression is given by

$$\rho = \frac{r}{h} = \frac{r_{norm} \bar{r}}{h}. \quad (3-33)$$

The freeform deformation of a surface is given by the Zernike fringe polynomials as

$$Z_{Zernike\ poly} = \sum_{i=1}^N C_i Z_i(\bar{r}, \phi) = \bar{C} \cdot \bar{Z}, \quad (3-34)$$

where C denotes the coefficients of the Zernike fringe terms, Z denotes the Zernike polynomials, and ϕ denotes the azimuthal angle of the aperture coordinate.

When n denotes the refractive index, the coefficients \bar{M} calculated in lens unit is defined as

Refractive

$$\bar{M} = \Delta(n) \bar{C}. \quad (3-35)$$

Mirror

$$\bar{M} = -2n \bar{C}. \quad (3-36)$$

Then the wavefront deformation of the generated by the Zernike fringe freeform polynomials at the pupil is given as

$$\Delta W_{Zernike\ poly} = \bar{M} \cdot \bar{Z}(\bar{r}, \phi) = \Delta(n) \bar{C} \cdot \bar{Z} \left[\left(\frac{h}{r_{norm}} \right) \bar{\rho} \right]. \quad (3-37)$$

When the surface is located away from the pupil, the normalized pupil vector in Eq. (3-37) will be replaced as the shifted pupil vector as in Eq. (3-31).

The wavefront deformation generated by the freeform deformation described Zernike fringe polynomials is derived as in Eqs. (3-33)-(3-37). The theory has been proposed from the extension of NAT [26, 27, 40].

However, the influence of the normalization radius was not discussed before. When the same freeform deformation is described by Zernike fringe polynomials with different normalization radius, the value of the coefficients will also be different. The deformation of the wavefront is the same, although the coefficients of the polynomials are different. Thus, Eq. (3-33) is used to obtain the relation of the normalized pupil coordinate and the normalized aperture coordinate. The influence of the normalization radius is included in the wavefront deformation as in Eq. (3-37).

Table 3-6 Wavefront deformation generated by term 2 to term 16 of a Zernike fringe surface at the pupil

Deformation	Vectorial representation
Spherical aberration	$6M_9 \left(\frac{h}{r_{norm}} \right)^4 (\vec{\rho} \cdot \vec{\rho})^2 - 30M_{16} \left(\frac{h}{r_{norm}} \right)^4 (\vec{\rho} \cdot \vec{\rho})^2$
Coma	$3 \left(\frac{h}{r_{norm}} \right)^3 (\vec{M}_{7/8} \cdot \vec{\rho})(\vec{\rho} \cdot \vec{\rho}) - 12 \left(\frac{h}{r_{norm}} \right)^3 (\vec{M}_{14/15} \cdot \vec{\rho})(\vec{\rho} \cdot \vec{\rho})$
Astigmatism	$\left(\frac{h}{r_{norm}} \right)^2 \vec{M}_{5/6} \cdot \vec{\rho}^2 - 3 \left(\frac{h}{r_{norm}} \right)^2 \vec{M}_{12/13} \cdot \vec{\rho}^2$
Defocus	$2 \left(\frac{h}{r_{norm}} \right)^2 M_4 (\vec{\rho} \cdot \vec{\rho}) - 6 \left(\frac{h}{r_{norm}} \right)^2 M_9 (\vec{\rho} \cdot \vec{\rho}) + 12 \left(\frac{h}{r_{norm}} \right)^2 M_{16} (\vec{\rho} \cdot \vec{\rho})$
Tilt	$\left(\frac{h}{r_{norm}} \right) \vec{M}_{2/3} \cdot \vec{\rho} - 2 \left(\frac{h}{r_{norm}} \right) \vec{M}_{7/8} \cdot \vec{\rho} + 3 \left(\frac{h}{r_{norm}} \right) \vec{M}_{14/15} \cdot \vec{\rho}$

The aberrations generated by the freeform deformation of a surface located at the pupil with Zernike fringe polynomials from term 2 to term 16 are shown in Table 3-6. It is seen in Table 3-6 that when the freeform surface is located at the pupil, it only generates field-constant aberrations. There is also no influence on field curvature or distortion. For some systems with large field-constant aberrations, such as TMAs with large field-constant coma, the freeform surface placed at the pupil position will contribute to the aberration correction effectively.

When the surface is located away from the pupil, all the field-constant aberrations in Table 3-6 are also generated. Due to the shift of the pupil vector according to finite chief ray height as in Eq. (3-31), each Zernike term generates also some other field-dependent aberrations. For instance, aberration generated by term 5 and 6 when the surface is located away from the pupil is derived as

$$\begin{aligned}
 \Delta W_{5/6} &= \bar{M}_{5/6} \cdot \left[\left(\frac{h}{r_{norm}} \right) (\bar{\rho} + \Delta \bar{h}) \right]^2 = \left(\frac{h}{r_{norm}} \right)^2 \bar{M}_{5/6} \cdot \bar{\rho}^2 \\
 &+ 2 \left(\frac{h}{r_{norm}} \right)^2 \left(\frac{\bar{h}}{h} \right) \bar{M}_{5/6} \cdot \bar{H} \bar{\rho} + \left(\frac{h}{r_{norm}} \right)^2 \left(\frac{\bar{h}}{h} \right)^2 \bar{M}_{5/6} \cdot \bar{H}^2 \\
 &= \left(\frac{h}{r_{norm}} \right)^2 \bar{M}_{5/6} \cdot \bar{\rho}^2 + 2 \left(\frac{h\bar{h}}{r_{norm}^2} \right) \bar{M}_{5/6} \bar{H}^* \cdot \bar{\rho} + \left(\frac{\bar{h}}{r_{norm}} \right)^2 \bar{M}_{5/6} \cdot \bar{H}^2.
 \end{aligned} \tag{3-38}$$

astigmatism, primary
change of magnification

It is seen from Eq. (3-38) that terms 5 and 6 generate another two terms in addition to the field-constant astigmatism. One is the change of magnification with the conjugate of field. The other one is quadratic piston.

Table 3-7 Aberrations generated by terms 7 and 8 of a Zernike fringe surface away from the pupil

Aberrations	Vectorial representation
Coma	$3 \left(\frac{h}{r_{norm}} \right)^3 (\bar{M}_{7/8} \cdot \bar{\rho}) (\bar{\rho} \cdot \bar{\rho})$
Astigmatism	$3 \left(\frac{\bar{h}h^2}{r_{norm}^3} \right) (\bar{M}_{7/8} \bar{H} \cdot \bar{\rho}^2)$
Focal plane of medial astigmatism	$6 \left(\frac{\bar{h}h^2}{r_{norm}^3} \right) (\bar{M}_{7/8} \cdot \bar{H}) (\bar{\rho} \cdot \bar{\rho})$
Distortion	$6 \left(\frac{\bar{h}^2 h}{r_{norm}^3} \right) (\bar{H} \cdot \bar{H}) (\bar{M}_{7/8} \cdot \bar{\rho}) + 3 \left(\frac{\bar{h}^2 h}{r_{norm}^3} \right) (\bar{H}^2 \bar{M}_{7/8}^* \cdot \bar{\rho})$

Following the same method to derive the aberrations, the aberrations generated by terms 7 and 8 of a Zernike fringe surface away from the pupil are listed in Table 3-7.

The aberrations generated by terms 7 and 8 in Table 3-7 are shown as an example because those two terms generate complicated aberrations away from the pupil. The field-constant coma is generated no matter where the surface is located. However, some aberrations have special relation to the field. The astigmatism generated from terms 7 and 8 is field-linear. It is known from Section 3.1

that the wave aberration generated by rotationally symmetric surface contains only terms with even order. The primary aberrations are of 4th order. Therefore, the primary astigmatism generated from the rotationally symmetric shape of the surface has a quadratic relation with field. However, the aberrations generated from the freeform deformation consist of even order terms and odd order terms. This special property will be mentioned in the surface selection rule in the following section.

The wavefront deformation generated by the Zernike fringe terms 2 to 16 when the surface is away from the pupil can be found in Appendix B.

3.5.3 Impact of a biconic basic shape

It is mentioned that rotationally-symmetric surfaces cannot decouple the astigmatism and coma. Biconic surface shape is nowadays used as an extension of the basic shape in surface representations. Due to the different focal powers in tangential and sagittal planes, the biconic surface can be used to correct astigmatism. The aberrations generated by the biconic surface are derived in this section. Therefore, the behavior of the biconic surface and its potential to correct aberrations can be studied.

As mentioned, the aberrations generated by the aspherical surface can be decomposed into one part generated by the basic spherical shape of the surface and the other part generated by the aspherical deformation. If the surface shape is further extended to the freeform shape, the aberrations generated by the freeform deformation is the third part of the total aberration contribution.

Due to the difference in x- and y-direction of the biconic surface, it is known that there is a freeform deformation from the rotationally symmetric shape. Therefore, the first step is to decompose the biconic surface representation into the spherical part, the aspherical part, and the freeform part. If the curvatures in x- and y-direction of a biconic surface are c_x and c_y , and the conic parameters in x- and y-direction are κ_x and κ_y , the surface representation is given as Eq. (2-55). We make a Taylor expansion of the surface sag about x^2 and y^2 around the origin. The second order expansion is given as

$$\begin{aligned}
Z_{biconic}^{(2nd)} &= \frac{c_x}{2}x^2 + \frac{c_y}{2}y^2 = \frac{c_x}{2}(x^2 + y^2) + \frac{c_y - c_x}{2}y^2 \\
&= \frac{c_x}{2}(\vec{r} \cdot \vec{r}) + \frac{c_y - c_x}{2}r^2 \sin^2 \phi \\
&= \frac{c_x}{2}(\vec{r} \cdot \vec{r}) + \frac{c_y - c_x}{2}r^2 \left(\frac{1 - \cos 2\phi}{2} \right) \\
&= \frac{1}{2} \left(\frac{c_x + c_y}{2} \right) (\vec{r} \cdot \vec{r}) + \frac{c_x - c_y}{4} r^2 \cos 2\phi.
\end{aligned} \tag{3-39}$$

basic spherical term *astigmatism, primary (axis in 0°), term 5*

The fourth order expansion is given as

$$\begin{aligned}
Z_{biconic}^{(4th)} &= \frac{1}{8}c_y^3(1 + \kappa_y)(y^2)^2 + \frac{1}{8}c_x^3(1 + \kappa_x)(x^2)^2 \\
&\quad + \frac{1}{8}c_x c_y (c_x + c_y + c_x \kappa_x + c_y \kappa_y) x^2 y^2 \\
&= \frac{1}{8} \left(\frac{c_x + c_y}{2} \right)^3 (\vec{r} \cdot \vec{r})^2 + \frac{1}{32} (c_x^2 - c_y^2) (c_x - c_y) (\vec{r} \cdot \vec{r})^2 \\
&\quad + \frac{1}{64} [c_x^2 \kappa_x (3c_x + c_y) + c_y^2 \kappa_y (3c_y + c_x)] (\vec{r} \cdot \vec{r})^2 \\
&\quad + \frac{1}{16} [c_x^3 (1 + \kappa_x) - c_y^3 (1 + \kappa_y)] r^4 \cos 2\phi \\
&\quad + \frac{1}{64} \left\{ \begin{aligned} &[c_x^3 (1 + \kappa_x) + c_y^3 (1 + \kappa_y)] \\ &- c_x c_y [c_x (1 + \kappa_x) + c_y (1 + \kappa_y)] \end{aligned} \right\} r^4 \cos 4\phi.
\end{aligned} \tag{3-40}$$

basic spherical term *aspherical deformation I*
aspherical deformation II
Astigmatism, secondary (axis in 0°), term 12
Tetrafoil, primary in x, term 17

From Eqs. (3-39)-(3-40), the biconic surface can be decomposed into the basic spherical shape and the anamorphic deformation. The basic shape is described as a spherical surface with the mean curvature as

$$c_{basic}^{biconic} = \frac{c_x + c_y}{2} \tag{3-41}$$

The expansion of the biconic surface up to the fourth order is converted into a freeform surface as

$$\begin{aligned}
Z_{biconic} &= \frac{1}{2} c_{basic}^{biconic} (\vec{r} \cdot \vec{r}) + \frac{1}{8} (c_{basic}^{biconic})^3 (\vec{r} \cdot \vec{r})^2 + (A_4^{biconic I} + A_4^{biconic II}) (\vec{r} \cdot \vec{r})^2 \\
&\quad + C_5^{biconic} r^{-2} \cos 2\phi + C_{12}^{biconic} (4r^{-4} - 3r^{-2}) \cos 2\phi + C_{17}^{biconic} r^{-4} \cos 4\phi
\end{aligned} \tag{3-42}$$

The biconic surface is formed by one spherical part with the mean mean curvature $c_{basic}^{biconic}$, two aspherical part with the fourth order aspherical coefficients as

$A_4^{biconic I}$ and $A_4^{biconic II}$, and the three Zernike fringe terms Z5, Z12 and Z17 with the

coefficients of the polynomials as $C_5^{biconic}$, $C_{12}^{biconic}$, and $C_{17}^{biconic}$. The value of the normalization radius r_{norm} is arbitrary. The value of the Zernike fringe coefficients will change due to the value of the normalization radius.

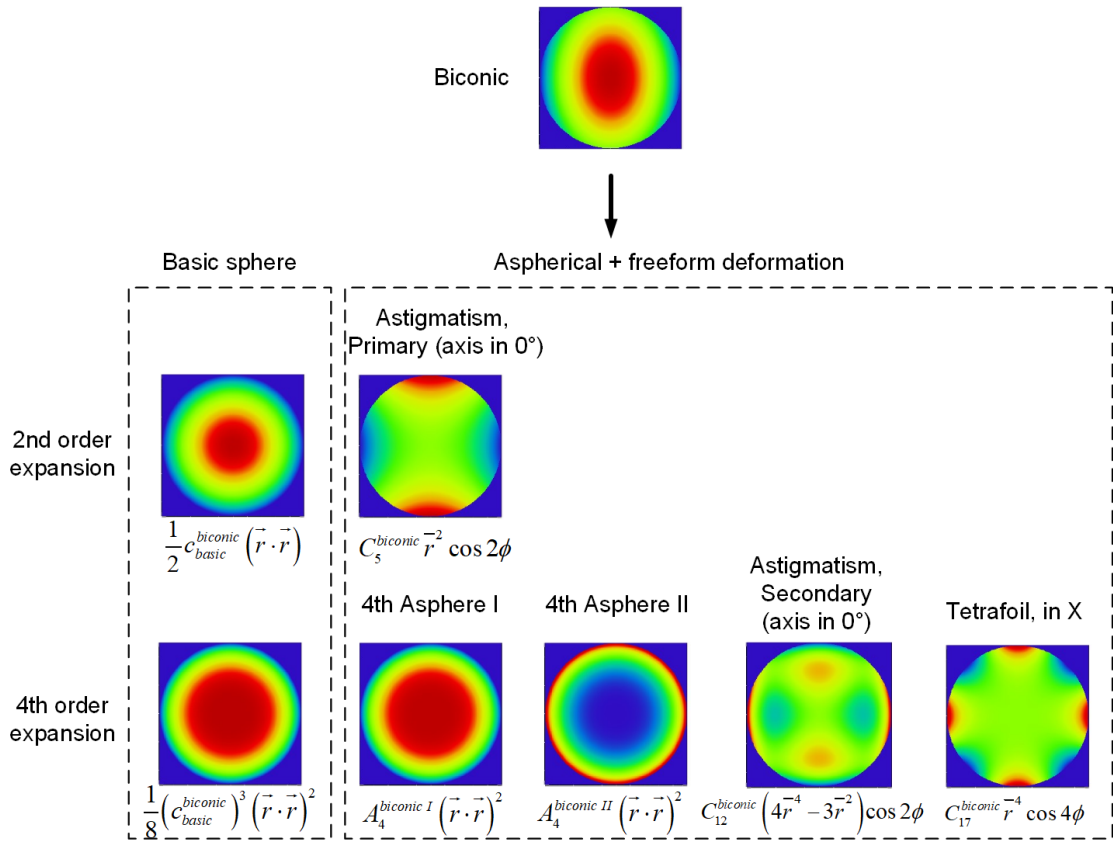


Figure 3-20 Decomposition of a biconic surface up to fourth order

Table 3-8 Aspherical terms of the converted biconic surface

Parameter	Value
$A_4^{biconic I}$	$\frac{1}{32}(c_x^2 - c_y^2)(c_x - c_y)$
$A_4^{biconic II}$	$\frac{1}{64}[c_x^2 \kappa_x (3c_x + c_y) + c_y^2 \kappa_y (3c_y + c_x)]$

Table 3-9 Freeform terms of the converted biconic surface

Parameter	Value
$C_5^{biconic}$	$\frac{c_x - c_y}{4} r_{norm}^2 + \frac{3}{64}[c_x^3(1 + \kappa_x) - c_y^3(1 + \kappa_y)] r_{norm}^4$
$C_{12}^{biconic}$	$\frac{1}{64}[c_x^3(1 + \kappa_x) - c_y^3(1 + \kappa_y)] r_{norm}^4$
$C_{17}^{biconic}$	$\frac{1}{64} \left\{ \begin{array}{l} [c_x^3(1 + \kappa_x) + c_y^3(1 + \kappa_y)] \\ [-c_x c_y [c_x(1 + \kappa_x) + c_y(1 + \kappa_y)]] \end{array} \right\} r_{norm}^4$

The coefficients of the aspherical terms and the freeform terms are listed in Table 3-8 and Table 3-9. The decomposition corresponding to Eq. (3-42) is illustrated in Figure 3-20.

Thus, the primary aberrations generated by the biconic surface as in Eq. (2-55) consists of the three parts:

(1) The primary aberrations generated by the basic spherical shape.

The primary aberration coefficients $W_{040}^{Bic-basic}$, $W_{131}^{Bic-basic}$, $W_{222}^{Bic-basic}$, $W_{220}^{Bic-basic}$, $W_{311}^{Bic-basic}$ can be derived using the mean curvature $C_{basic}^{biconic}$ of the basic spherical shape as in Table 2-1. The vectorial wave aberrations are represented as the terms in Eq. (2-18).

(2) The primary aberrations generated by the two aspherical terms.

Similarly to Eq. (3-32), the spherical aberration coefficient of the aspherical deformation is defined as

$$W_{040}^{Bic-Asph} = \Delta(n) \left(A_4^{biconic I} + A_4^{biconic II} \right) h^4 \quad (3-43)$$

The aberrations generated by the aspherical terms can be represented as the terms in Table 3-5.

(3) Aberrations generated by the freeform terms.

The freeform parts of the biconic surface consist of one primary astigmatic term (axis in 0°), one secondary astigmatic term (axis in 0°), and one tetrafoil term (in x). In the extension of NAT as Eqs. (3-33)-(3-37), when the surface is located at the stop, each freeform term generates only the corresponding field-constant aberration. When the surface is away from the pupil, the normalized pupil vector has a shift factor, which introduces the field-dependent factor in the wavefront deformation. Therefore, the freeform terms also generate field-dependent aberrations when the surface is away from the pupil.

Table 3-10 Aberrations generated by the primary astigmatic term

Aberration	Value
Astigmatism, primary (axis in 0°)	$\left(\frac{h}{r_{norm}} \right)^2 \Delta(n) C_5^{biconic} \rho^2 \cos 2\phi$
Change of magnification	$2 \frac{h\bar{h}}{r_{norm}^2} \Delta(n) C_5^{biconic} \left(\vec{H}^* \cdot \vec{\rho} \right)$

Table 3-11 Aberrations generated by the secondary astigmatic term

Aberration	Value
Astigmatism, Secondary (axis in 0°)	$4\left(\frac{h}{r_{norm}}\right)^4 \Delta(n) C_{12}^{biconic} \rho^4 \cos 2\phi$
Coma	$12 \frac{h^3 \bar{h}}{r_{norm}^4} \Delta(n) C_{12}^{biconic} (\bar{H}^* \cdot \bar{\rho}) (\bar{\rho} \cdot \bar{\rho})$
Astigmatism, primary (axis in 0°)	$-3\left(\frac{h}{r_{norm}}\right)^2 \Delta(n) C_{12}^{biconic} \rho^2 \cos 2\phi$ $+12 \frac{h^2 \bar{h}^2}{r_{norm}^4} \Delta(n) C_{12}^{biconic} (\bar{H} \cdot \bar{H}) \rho^2 \cos 2\phi$
Focal plane of medial astigmatism	$12 \frac{h^2 \bar{h}^2}{r_{norm}^4} \Delta(n) C_{12}^{biconic} (H_x^2 - H_y^2) (\bar{\rho} \cdot \bar{\rho})$
Distortion	$12 \frac{h \bar{h}^3}{r_{norm}^4} \Delta(n) C_{12}^{biconic} (\bar{H} \cdot \bar{H}) (\bar{H}^* \cdot \bar{\rho})$ $+4 \frac{h \bar{h}^3}{r_{norm}^4} \Delta(n) C_{12}^{biconic} (\bar{H}^3 \cdot \bar{\rho})$
Trefoil	$4 \frac{h^3 \bar{h}}{r_{norm}^4} \Delta(n) C_{12}^{biconic} (\bar{H} \cdot \bar{\rho}^3)$

Table 3-12 Aberrations generated by the tetrafoil term

Aberration	Value
Tetrafoil (in x)	$\left(\frac{h}{r_{norm}}\right)^4 \Delta(n) C_{17}^{biconic} \rho^4 \cos 4\phi$
Trefoil	$4 \frac{h^3 \bar{h}}{r_{norm}^4} \Delta(n) C_{17}^{biconic} \bar{H}^* \cdot \bar{\rho}^3$
Astigmatism, primary	$6 \frac{h^2 \bar{h}^2}{r_{norm}^4} \Delta(n) C_{17}^{biconic} (\bar{H}^2)^* \cdot \bar{\rho}^2$
Distortion	$4 \frac{h \bar{h}^3}{r_{norm}^4} \Delta(n) C_{17}^{biconic} (\bar{H}^3)^* \cdot \bar{\rho}$

The aberrations generated by the primary astigmatic term, the secondary astigmatic term and the tetrafoil term of the biconic surface are listed in Table 3-10, Table 3-11 and Table 3-12. It can be seen that there is always the field-constant astigmatism generated by the biconic surface depending on the value of the coefficients $C_5^{biconic}$ and $C_{12}^{biconic}$. But the value of coma is always field-dependent. Therefore, for a biconic surface, the total generated astigmatism is decoupled with coma. The decoupling can be used as an advantage when designing off-axis

systems. It is easier to obtain nodal point of both coma and astigmatism at the center of the FOV. The verification of the aberration values is shown in Appendix C.

3.6 Selection of freeform surface position

It is known that concerning the manufacturing and cost of the optical system, the number of freeform surfaces and aspheres should be as small as possible. The surface shape should also be as simple as possible. Thus, the initial setup is optimized with minimum residual aberrations before adding aspheres and freeform surfaces.

However, the position to add an asphere or a freeform surface is not arbitrary. First of all, the system performance of the initial setup should be analyzed. When the system is dominated by field-constant aberrations or field-dependent aberrations, the locations to place freeform surfaces are completely different. From aberrations generated by aspheres and freeform surfaces, it is known that the three factors, which determine the aberrations generated by the deformation, are the coefficients of the polynomials, the ratio \bar{h}/h between the chief ray height and the marginal ray height, and the ratio h/r_{norm} between the marginal ray height and normalization radius. Among those three factors, the ratio \bar{h}/h is determined by the location of the surface, since it represents the separation of the ray bundles of different fields on the surface. The difference of the ratio at the pupil and away from the pupil is illustrated in Figure 3-21.

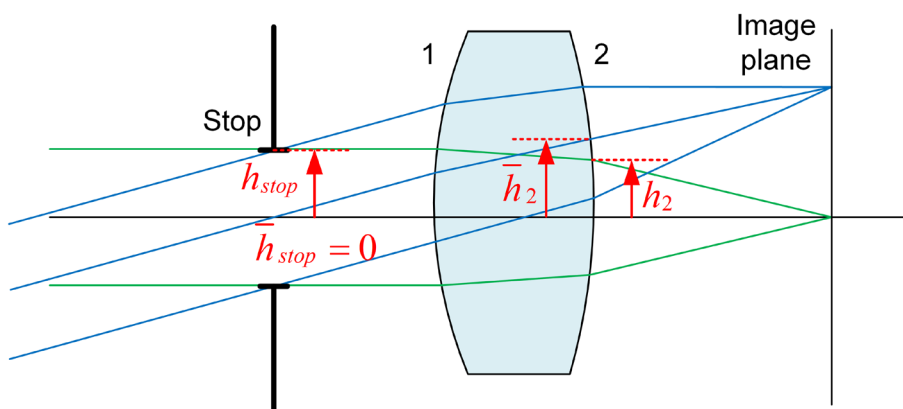


Figure 3-21 Difference of the ratio \bar{h}/h at the pupil and away from the pupil

The surface, which is selected to add the aspheres or freeform surfaces, should perform efficient to compensate the residual aberrations in the system. Thus, the rules for surface position selection are concluded as follows.

(1) If conic surfaces and aspheres are located at the pupil, they can only correct spherical aberration. But away from the pupil, they can correct the other four primary aberrations, which are field-dependent.

(2) The freeform deformation of a Zernike fringe freeform surface at the pupil generates only field-constant aberrations corresponding to the terms, which are used. The Zernike fringe polynomials at the pupil do not influence distortion and field curvature.

(3) When the Zernike fringe freeform surface is located away from the pupil, the freeform part of the surface generates not only field-constant aberrations corresponding to the terms but also other field-dependent aberrations.

(4) The aberrations generated by aspheres and freeform surfaces are both influenced by the separation of the ray bundles of different fields. The separation can be described by the ratio between the paraxial chief ray height of the largest field and the marginal ray height, which is written as \bar{h}/h .

(5) Normally a lens close to the conjugated image plane has large value of the ratio \bar{h}/h . The freeform deformation generates large field-dependent aberrations. It explains the effect that the freeform surface placed at the field lens has large impact on distortion.

(6) When the freeform surface is away from the pupil, the freeform deformation generates both even and odd order aberrations. The aberrations generated by rotationally symmetric components are always of even order. The even order aberrations generated by the freeform deformation are used to compensate the residual aberrations from the initial setup. However, the odd order aberrations should be compensated by another freeform surface away from the pupil.

(7) It is mentioned that the odd order aberrations generated by two freeform surfaces should compensate each other. However, the two freeform surfaces should not be too close to each other. When the two surfaces are close to each other, the values of the ratio \bar{h}/h are similar. If the odd order aberrations generated by two freeform surfaces with the same ratio of \bar{h}/h compensate each other, the generated even order aberrations also compensate each other. The two surfaces

have in total no contribution in the aberration correction. Therefore, it is better to choose two freeform surfaces, which have large difference in the ratio of \bar{h}/h . In this way, it is possible to compensate the odd order aberrations, and certain even order aberrations are generated by the two freeform surfaces to compensate the residual aberrations in the system.

The TMA system has only three surfaces. If the specifications are high, only one freeform surface is allowed, and the other two surfaces are aspheres, the location of the aspheres will never be the surfaces close to the stop. When the asphere is away from the pupil in the off-axis system, it can be regarded as a quasi-freeform surface to compensate the field-dependent aberrations.

For systems with only field-dependent aberrations, such as Scheimpflug systems, the location of freeform surface is never close to the stop, which will be demonstrated in Chapter 4.

4 Examples and applications

In this chapter, three typical non-rotationally symmetric applications are discussed. The TMA system is demonstrated to show the initial system design steps based on Gaussian brackets method. The strategy to correct coma is shown in the initial design of the Yolo telescope. Biconic surfaces are used to further correct the large astigmatism in the system. With the Scheimpflug system, the aberration analysis and the surface position evaluation are shown. By understanding the initial system behavior and following the surface selection rules, the system performance is tremendously improved and uniformed after adding the freeform surfaces.

4.1 TMA system

Two TMA systems are designed with the Gaussian brackets method to demonstrate the initial system design procedure. The TMA systems are of no chromatic aberrations due to the use of mirrors. Thus, the choice and optimization of materials are not necessary. The back focal length is added in the nonlinear functions as another first-order property to control the working distance. As mentioned, the stop position can be defined in this method. For the first example with the zigzag structure, the stop is defined at the location of the second mirror. The stop of the second example with the folding structure is located before the first mirror.

The first step is to establish the on-axis model for the paraxial ray trace. The on-axis model of the TMA system is shown as in Figure 4-1.

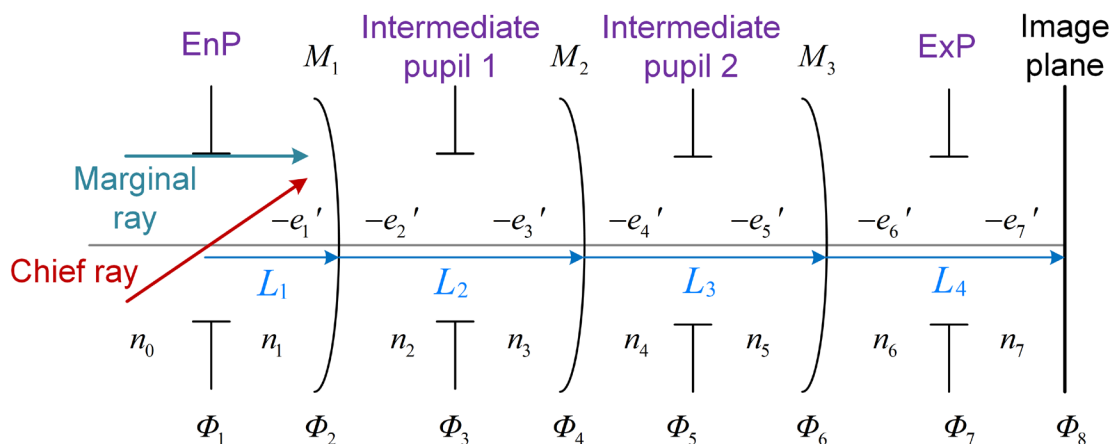


Figure 4-1 On-axis model of a TMA system

It is seen in Figure 4-1 that a TMA system consists of eight surfaces in total including three mirrors, intermediate pupils, and the image plane. The focal powers of the intermediate pupils and the image plane are zero as

$$\Phi_1 = \Phi_3 = \Phi_5 = \Phi_7 = \Phi_8 = 0. \quad (4-1)$$

In Figure 4-1, L_j denotes the thickness from real surface to surface, which can be represented by the reduced distance e_j' .

The first example is the zigzag structure TMA system. The focal power of the three mirrors is defined to be negative-positive-positive (NPP). The NPP structure can be obtained by setting different boundary values for the curvatures in the optimization of the nonlinear functions. The design specifications are listed in Table 4-1. The stop is located at the second mirror. Thus the reduced distances e_3' and e_4' are zero. The intermediate pupil 1 and intermediate pupil 2 in Figure 4-1 coincide at the position of the second mirror.

Table 4-1 Specifications of the zigzag TMA system

Parameter	Specification
Focal length	117.61 mm
Entrance pupil diameter	50 mm
FOV	3°×4°
F-number	2.78
Stop position	Second mirror

According to the FOV and entrance pupil diameter, the initial ray data of the marginal ray and chief ray at the first surface (EnP) are defined as in Table 4-2.

Table 4-2 Initial ray data for paraxial on-axis ray tracing defined at the EnP

Marginal ray	$h_1 = 25.0000 \text{ mm}$	$u_1 = 0.0000 \text{ rad}$
Chief ray	$\bar{h}_1 = 0.0000 \text{ mm}$	$\bar{u}_1 = 0.0436 \text{ rad}$

Using the Petzval curvature vanishing relation as Eq. (3-3), the curvature of M3 can be expressed by the curvatures of M1 and M2. The unknown parameters are the three tilts of the mirrors, curvature of the first two mirrors, and two thicknesses L_1 and L_3 . Since the stop is located at M2, the thicknesses L_2 can be expressed by the imaging relation by M1 from the EnP to M2. The five primary aberrations of the central field, the condition to fulfill Coddington equations, the focal length, and the back focal length are defined as the nonlinear functions. The boundary values and the solutions of the nonlinear optimization are given in Table 4-3. The

sign and boundary values of the tilts are defined in the range to avoid obscuration. When the structure is defined as zigzag, the tilts of M1 and M3 are positive and the tilt of M2 should be negative.

Table 4-3 Boundary values and solutions of the nonlinear functions for the zigzag structure TMA system

Parameter	Lower limit	Upper limit	Solution
$i_2 = i'_2$	13.4148 degree	53.1301 degree	40.6035 degree
$i_4 = i'_4$	-53.1301 degree	-13.4148 degree	-19.3914 degree
$i_6 = i'_6$	13.4148 degree	53.1301 degree	19.3914 degree
$Radius_2$	200.0000 mm	350.0000 mm	269.5010 mm
$Radius_4$	300.0000 mm	500.0000 mm	407.5147 mm
$Radius_6$	---	---	-795.7586 mm
L_1	-120.0000 mm	-80.0000 mm	-80.0000 mm
L_2	---	---	-196.8939 mm
L_3	200.0000 mm	300.0000 mm	200.0000 mm

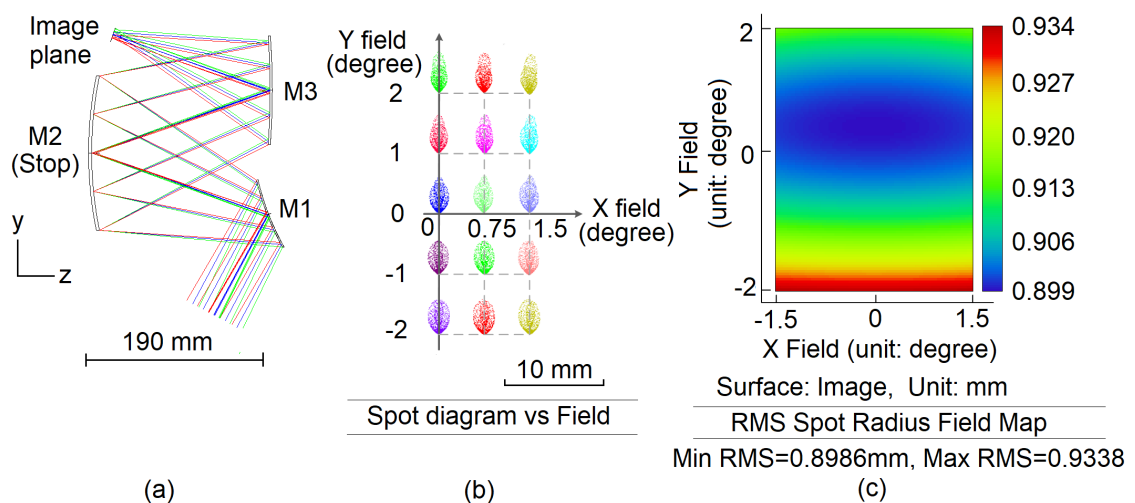


Figure 4-2 System performance of the zigzag structure TMA system (a) System layout; (b) Spot diagram with field; (c) RMS Spot radius map with field.

In Figure 4-2, the layout of the initial setup, the spot diagram, and the RMS spot radius over the whole FOV are illustrated for initial setup of the zigzag structured TMA. The full-field-display of astigmatism by Zernike fringe coefficients $\sqrt{Z5^2 + Z6^2}$, coma by Zernike fringe coefficients $\sqrt{Z7^2 + Z8^2}$, and grid distortion are shown in Figure 4-3. For the initial setup, one nodal point of astigmatism can

be seen in Figure 4-3 (a). The other nodal point of astigmatism is outside of the FOV due to the boundary conditions to achieve obscuration free. Due to the limitations of the angles and focal power, the nodal point of coma is not obtained and the whole FOV is dominated by field-constant coma. Distortion is -1.5%, which is acceptable. Then we set the three radii of curvature and conic parameters as variables. The third mirror is set as a Zernike fringe sag freeform surface with terms Z5, Z8, Z9, Z11, Z12, Z15, and Z16 as variables. The criterion is the resolution of the whole FOV. It can be seen in Figure 4-3(e) that the field-constant coma is reduced by the freeform surface after optimization. The nodal point of coma is obtained in the FOV. The value of astigmatism and coma are both improved.

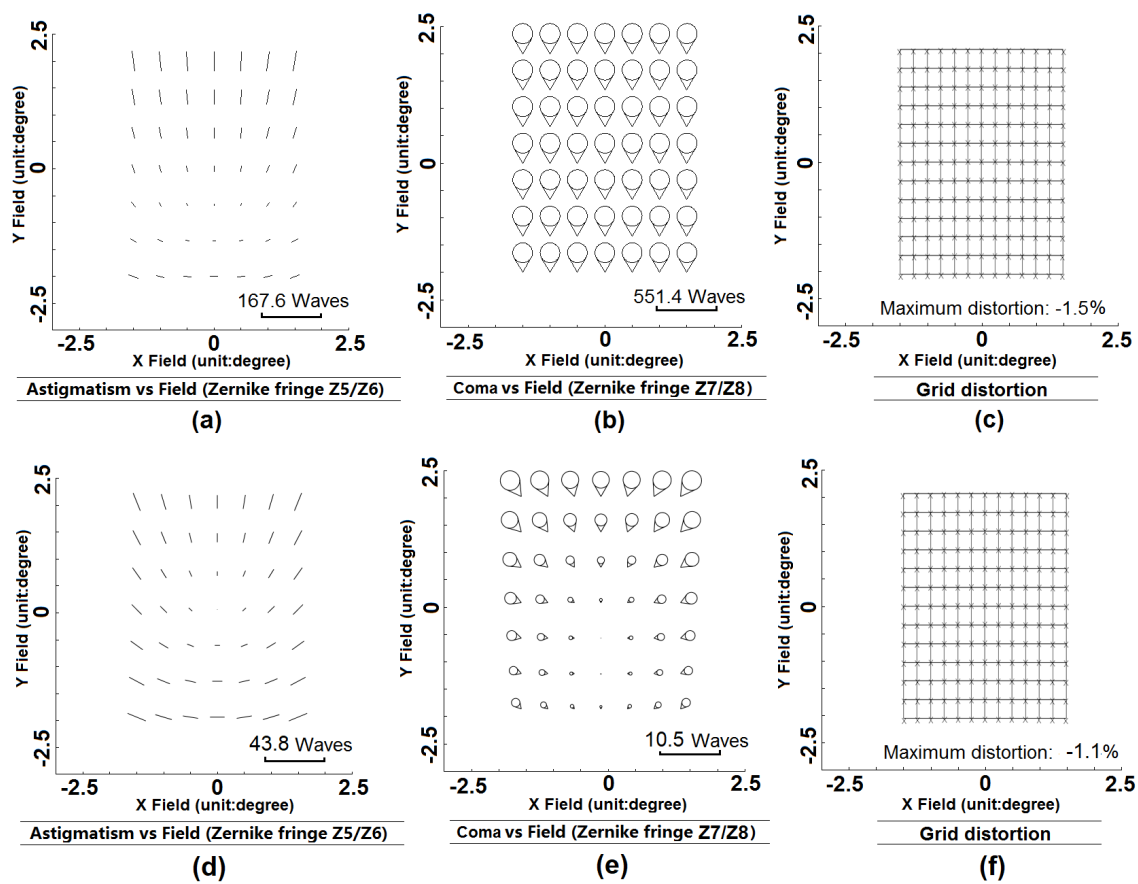


Figure 4-3 Aberrations with field of the zigzag structure TMA system (a) Astigmatism, (b) coma, and (c) grid distortion of initial setup; (d) Astigmatism, (e) coma, and (f) grid distortion of optimized setup;

The second example is a TMA system with folding structure. As it is mentioned in the conic-confocal method, it is inconvenient to optimize the freeform surface

when there is a large off-axis use. The specifications are obtained from the proceeding of H. Zhu [35], in which the TMA was designed based on the conic-con-focal method. Here, only spherical surfaces are used to establish the initial system. Thus, the vertex of the surface is located at the intersection point of the OAR, which overcomes the inconvenience of off-axis use of the surfaces. The central part of the freeform surface will influence the aberrations in the optimization. In this example, the entrance pupil diameter and the focal length are both very large. Therefore, a folding structure is normally used to make the system compact. The design specifications are listed in Table 4-4. The initial ray data of the marginal ray and chief ray are defined as in Table 4-5 at the entrance pupil plane.

Table 4-4 Specifications of the folding structure TMA system

Parameter	Specification
Focal length	310 mm
Entrance pupil diameter	200 mm
FOV	$1.774^\circ \times 1.331^\circ$
F-number	1.55
Stop position	Before the first mirror

Table 4-5 Initial ray data for paraxial on-axis ray tracing defined in the EnP

Marginal ray	$h_1 = 100.0000 \text{ mm}$	$u_1 = 0.0000 \text{ rad}$
Chief ray	$\bar{h}_1 = 0.0000 \text{ mm}$	$\bar{u}_1 = 0.0194 \text{ rad}$

Table 4-6 Boundary values and solutions of the nonlinear functions for the folding structure TMA system

Parameter	Lower limit	Upper limit	Solution
$i_2 = i'_2$	11.5369 degree	30.0000 degree	11.5369 degree
$i_4 = i'_4$	11.5369 degree	30.0000 degree	27.3373 degree
$i_6 = i'_6$	11.5369 degree	30.0000 degree	11.5369 degree
$Radius_1$	-12500.0000 mm	-12000.0000 mm	-12499.9999 mm
$Radius_4$	-800.0000 mm	-770.0000 mm	-790.7689 mm
$Radius_6$	---	---	-844.1725 mm
L_1	710.0000 mm	750.0000 mm	750.0000 mm
L_2	-640.0000 mm	-620.0000 mm	-637.7265 mm
L_3	620.0000 mm	640.0000 mm	640.0000 mm

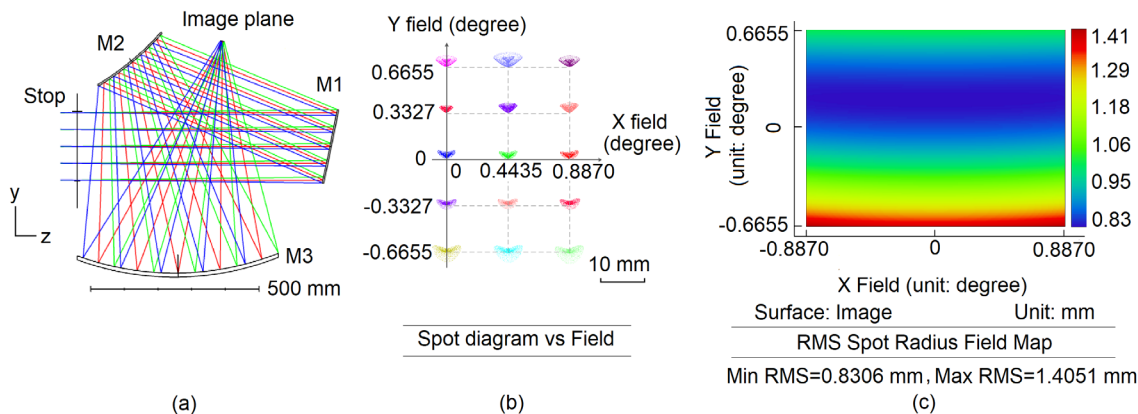


Figure 4-4 System performance of the folding structure TMA system (a) System layout; (b) Spot diagram with field; (c) RMS Spot radius map with field.

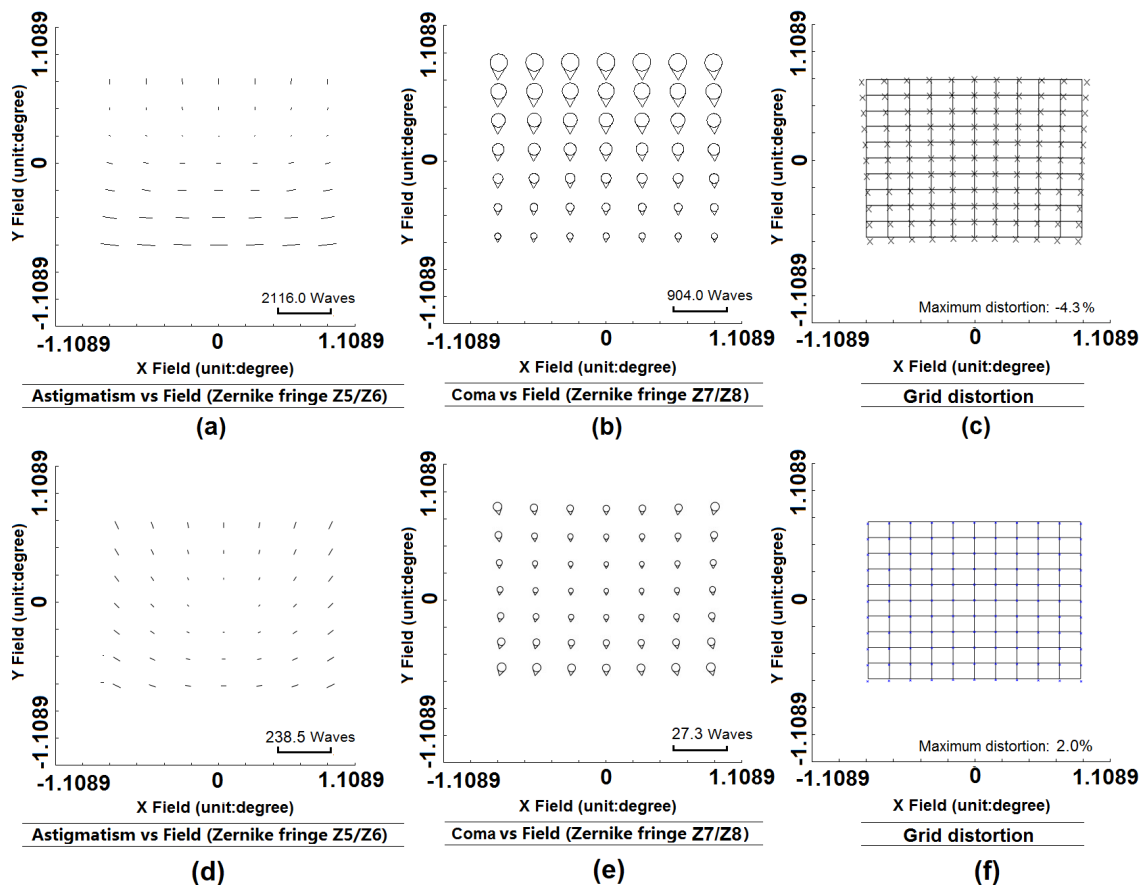


Figure 4-5 Aberrations with field of the compact folding structure TMA system (a) Astigmatism, (b) coma, and (c) grid distortion of initial setup; (d) Astigmatism, (e) coma, and (f) grid distortion of optimized setup;

In this case, the stop is located before M1, which means it is located at the entrance pupil. Therefore, L_2 cannot be represented by other parameters. It is also one of the unknown parameters. The boundary values and the solutions after

nonlinear function optimization are presented in Table 4-6. The three tilts should be all positive to obtain the folding structure.

The layout, the spot diagram, and the RMS spot radius over the whole FOV of the initial system with the folding structure are shown in Figure 4-4. The third mirror is set as a Zernike fringe freeform surface and the initial setup is further optimized. The full-field-display of astigmatism by Zernike fringe coefficients $\sqrt{Z5^2 + Z6^2}$, coma by Zernike fringe coefficients $\sqrt{Z7^2 + Z8^2}$, and grid distortion of both the initial setup and the optimized setup are shown in Figure 4-5. M3 is the freeform surface, and the variables are the same as the zigzag example. The criterion is also the resolution of the whole FOV. In the initial setup, the second nodal point for astigmatism is also out of the field of view. However, although the field-constant coma is not completely corrected, the FOV is closer to the nodal point of coma. The system suffers from keystone distortion. After adding the freeform polynomials to the system, the aberrations are improved.

4.2 Yolo telescope

The Yolo telescope is an unobscured off-axis reflective system with no symmetry due to the tilts of the mirrors in both tangential and sagittal planes. The original Yolo telescope is formed by two mirrors. In 1970s, it is extended with the third mirror to deal with wide field [41]. Therefore, we name the Yolo telescope with three mirrors as extended Yolo telescope. The extended Yolo telescope designed by Arthur S. Leonard has a large f-number of 13.32. In this work, the extended Yolo telescope is improved to an f-number of 2.24 with freeform surface [42]. Since the system size should not be too large and still free of obscuration, the tilt range of the surfaces is quite tight. When the initial system is designed, the spherical aberration and coma are the main selected aberrations to be corrected, due to the large numerical aperture and limited tilt range. Astigmatism is not selected as one of the nonlinear functions in the Gaussian brackets method. After the initial system is obtained, the surfaces are optimized with biconic surfaces, since it is mentioned that biconic surfaces provide large ability to correct astigmatism.

The procedure to design the initial setup is similar with the steps to design a TMA system as in Section 4.1. The only difference is that the x-component of the field

shift vector is also an unknown parameter. The design specifications are listed in Table 4-7.

Table 4-7 Specifications of the small f-number Yolo telescope system

Parameters	Value
Entrance pupil diameter	270 mm
F-number	2.24
Focal length	600 mm
FOV	$1^\circ \times 1^\circ$
Working spectrum	$3 \mu\text{m}$ to $5 \mu\text{m}$ in MWIR
Pixel size	$12.5 \mu\text{m}$
Stop position	First mirror

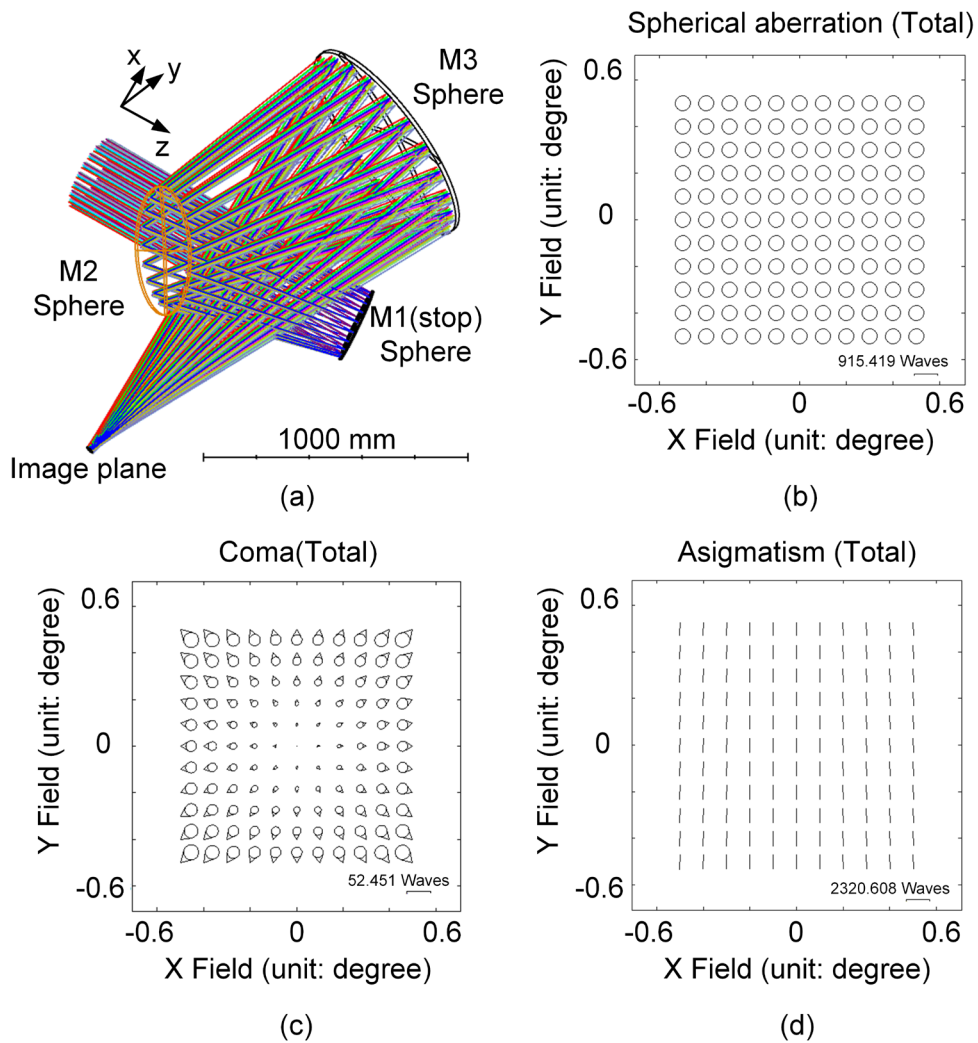


Figure 4-6 (a) Layout of the initial extended Yolo telescope; (b) Total spherical aberration; (c) Total coma; (d) Total astigmatism

The first mirror of the system is only tilted in x-direction. Thus, the y-component of the field shift vector equals zero. The field shift vectors of the other two mirrors have both x- and y-components. The range of the tilt angles should be modified by several iterations in the boundary condition in order to achieve obscuration free condition when solving the nonlinear equations. The layout of the initial setup and the full-field-display of spherical aberration, coma and astigmatism based on NAT are illustrated in Figure 4-6. It can be seen that the nodal point of coma is obtained in the center of the FOV. Compared with astigmatism, the value of spherical aberration and coma is much smaller.

The strategy to obtain the nodal point of coma is discussed in Section 3.5.1. The main idea is to correct the field-constant coma. It is known from Eqs. (3-25)-(3.26) that the field-constant coma of each surface equals the product of the Seidel aberration coefficient of coma and the field shift vector. It is shown in Figure 4-7 (a) that the Seidel coefficients of coma have the same sign for the three mirrors. Thus, the field shift vector should have different sign in x- and y-direction, which can be seen in Figure 4-7 (b).

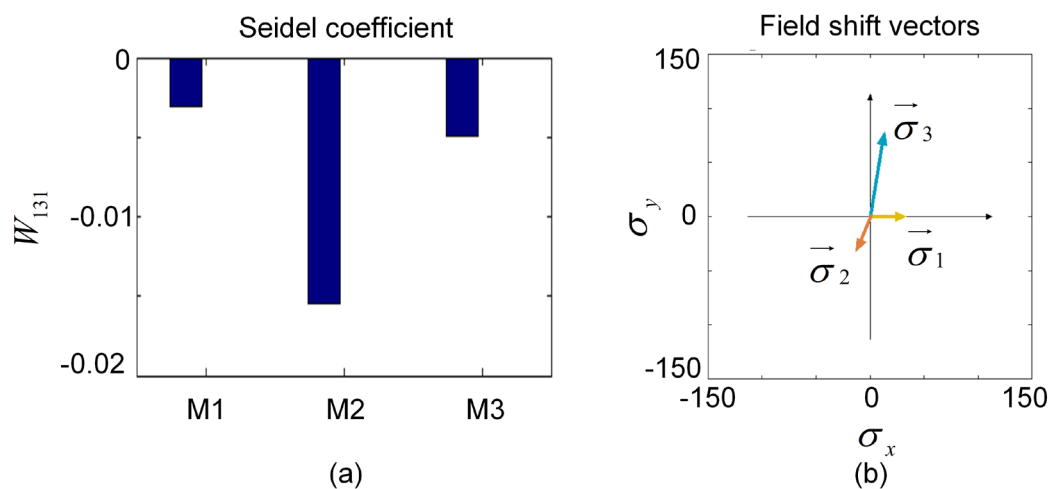


Figure 4-7 Surface contribution of the Yolo telescope (a) Seidel coefficient of coma; (b) Field shift vectors.

The full-field coma contribution of the three mirrors are shown in Figure 4-8 individually. Each of the mirrors introduces a large field constant coma to the system. If the field-constant coma contribution in total do not vanish, it will end up with a very large total field-constant coma.

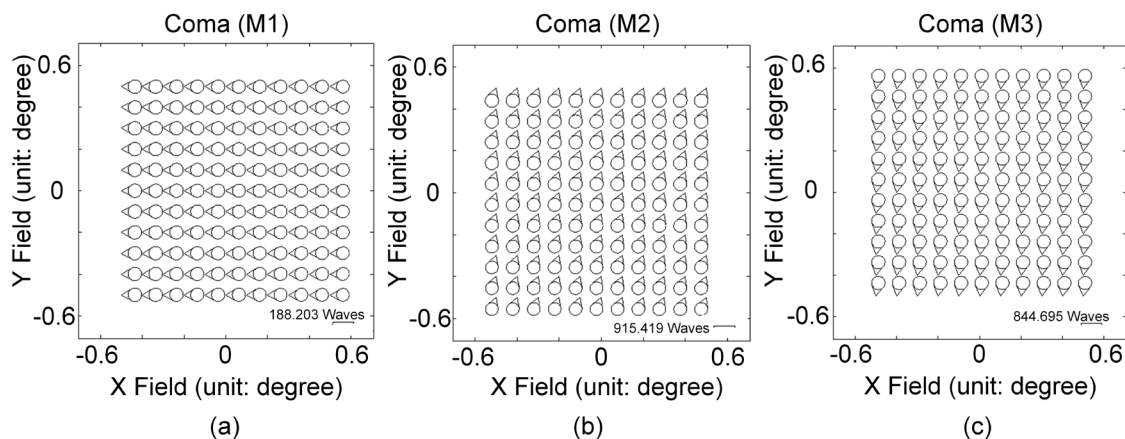


Figure 4-8 Full-field-display of coma surface contribution in the initial setup.
(a) M1, (b) M2, and (c) M3.

The initial setup is further optimized with three freeform surfaces with biconic basic shape and Zernike standard polynomials. The surface type is called Biconic Zernike in OpticStudio. M1 and M2 are both optimized with Zernike polynomials up to the 25th term, and M3 is optimized up to the 16th terms. The final system layout is shown in Figure 4-9(a). The modular transfer function (MTF) is shown in Figure 4-9(b) for wavelength of 4 μm . The MTF is above 0.4 at 40 lp/mm.

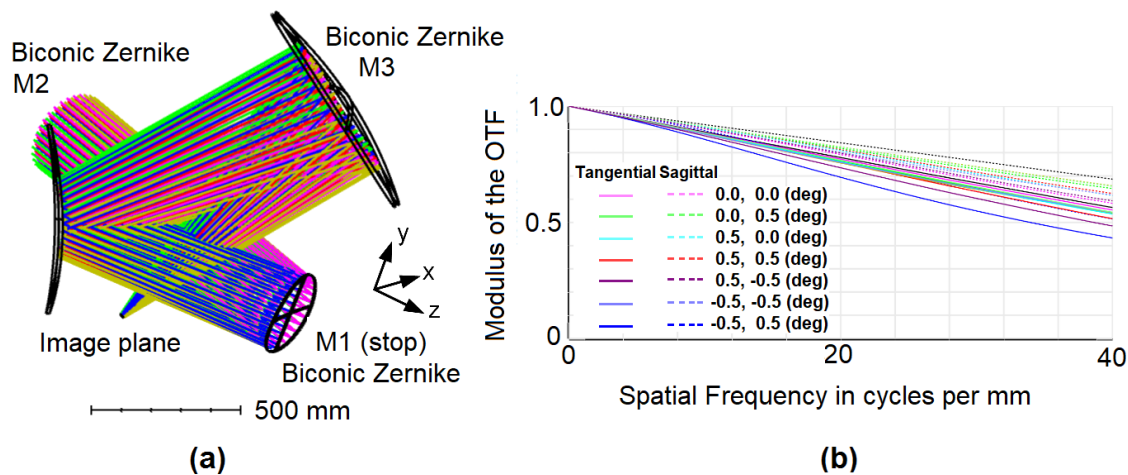


Figure 4-9 (a) 3D System layout of extended Yolo telescope after optimization;
(b) MTF of the extended Yolo telescope system for the wavelength 4 μm .

The total coma and astigmatism are shown in Figure 4-10 based on Zernike fringe coefficients of wave aberration. Due to the use of freeform surfaces, the distribution of aberrations over the FOV is non-rotationally symmetric. But it is seen that the coma distribution of the FOV locates in a valley around the nodal point. From the scale bar, it is seen that the aberrations are tremendously improved compared

with the initial setup in Figure 4-6. The RMS value over the whole FOV is 0.083 Waves of the total coma and 0.251 Waves of the total astigmatism.

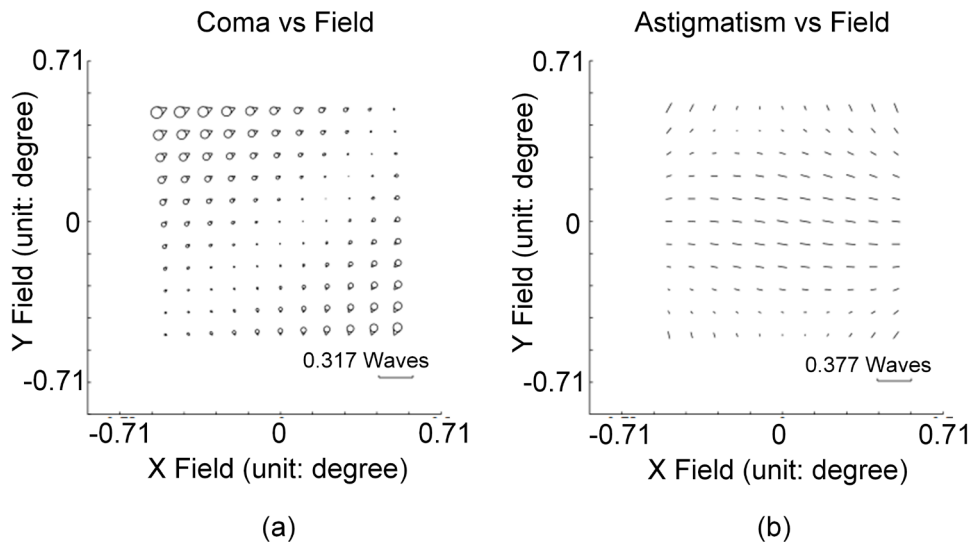


Figure 4-10 Full-field-display of aberrations of the final design of the extended Yolo telescope. (a) Coma by Zernike fringe coefficients $\sqrt{Z7^2 + Z8^2}$; (b) Astigmatism by Zernike fringe coefficients $\sqrt{Z5^2 + Z6^2}$.

4.3 Scheimpflug system

In a Scheimpflug system, the object plane is not perpendicular to the optical axis. In paraxial approximation, the sharp image of the tilted object plane locates on an oblique image plane as shown in Figure 4-11.

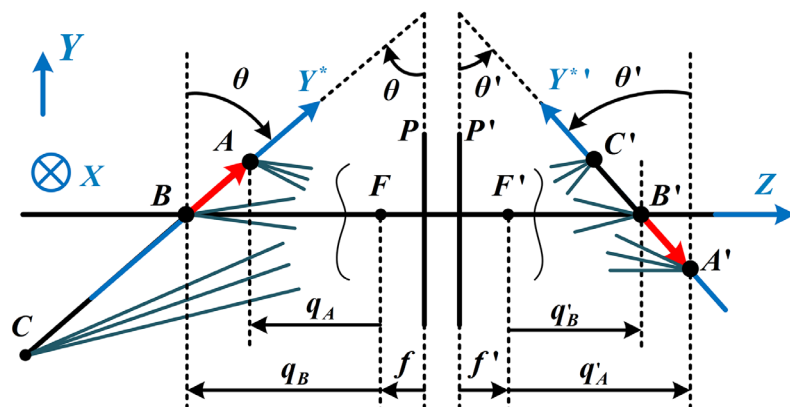


Figure 4-11 Scheimpflug imaging condition in paraxial approximation

If we assume that the angle between the object plane and the front principal plane is θ , the tilted angle θ' of the image plane with the back principal plane follows the relation as

$$m_0 = \frac{\tan \theta'}{\tan \theta}, \quad (4-2)$$

where m_0 denotes the transverse magnification of the axial field, which is point B in Figure 4-11. m_0 is named the axial transverse magnification. In the tangential plane (Y-Z plane), when the object or image plane is tilted clockwise, the tilt angle is defined as negative. On the contrary, when it is tilted counterclockwise, the tilt angle is defined as positive.

However, due to the shift of object distance from point A to point B, the magnification is not constant. It is a function of the object height in Y*-axis [43]. Thus, the system suffers from keystone distortion, non-uniform resolution, and non-uniform intensity distribution. Keystone distortion is normally corrected by image processing techniques. In this work, the aim is to reduce the aberrations and improve the uniformity of aberrations with freeform surfaces in order to improve the performance of the whole FOV.

Table 4-8 Design specifications of the Scheimpflug system

Parameters	Values
Wavelength	632.8nm
Focal length	41.32 mm
Measurement range	20mm×100mm
Size of lens components	7mm~15mm
Size of sensor	9mm×9mm
Size of pixel	5μm×5μm
Object tilt angle	-70°
Working distance	90 mm
Total length	150 mm
Object space NA (axial field point)	0.055
Image space NA (axial field point)	0.268
Axial transverse magnification	-0.205

The design specifications are listed in Table 4-8. It is a scanning system with the scanning range of 20mm×100mm. The tilt angle of the object plane with the principal plane is -70 degree, which leads to a large object distance shift of 93.97mm

compared with the focal length 41.32 mm. The illumination is monochromatic with wavelength of 632.8nm. The free working distance is 90 mm from the axial field to the front surfaces. The total system length from the axial field to its image point is 150 mm. The object and image space numerical apertures are both defined for the axial field.

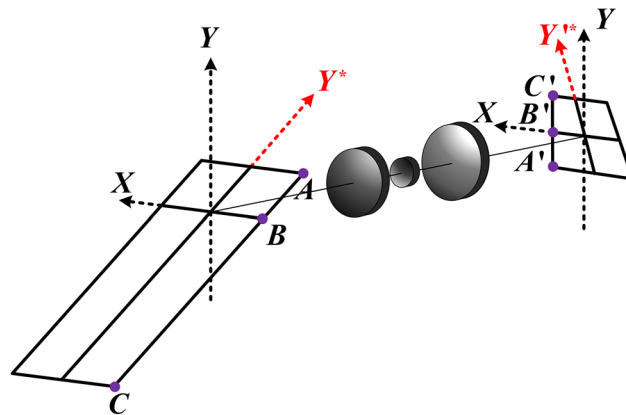


Figure 4-12 3D layout of the Scheimpflug system

The initial setup is obtained using the Gaussian brackets method with spherical surfaces. From the cost and manufacturing point of view, it is expected that the number of elements in the system is small, and materials are supposed to be cheap. Since the system is monochromatic, we construct the system using three single lenses with the glass BK7. According to the measuring range and the axial magnification, it is selected that the focal length is 41.32mm. The maximum and minimum fields are 30 mm and -70mm in Y^* direction.

According to the conclusion of C. G. Wynne mentioned in [44], it is impossible to correct all the aberrations for two different object distances with only spherical surfaces. As mentioned in Chapter 3, each object distance of the Scheimpflug system can be seen as a centered system individually, but the difference in aberrations along the object shift is large. It is known that in centered systems, the five primary aberrations are coupled. We select only the spherical aberration and distortion of three selected points A, B and C in Figure 4-12 together with the focal length as the nonlinear functions to be optimized. When those two aberrations are optimized to be uniform, the non-uniformity of other aberrations will be also reduced. The initial setup is obtained and further optimized according to the constraint of the components size, which is shown in Figure 4-13(a).

Before adding freeform surfaces, the system is further optimized with the conic parameter on each surface. However, due to the coupling of astigmatism and coma, additional aspherical terms are not effective to improve the system performance. Therefore, the system with conic surfaces as shown in Figure 4-13(b) is used as the intermediate system before adding freeform surfaces.

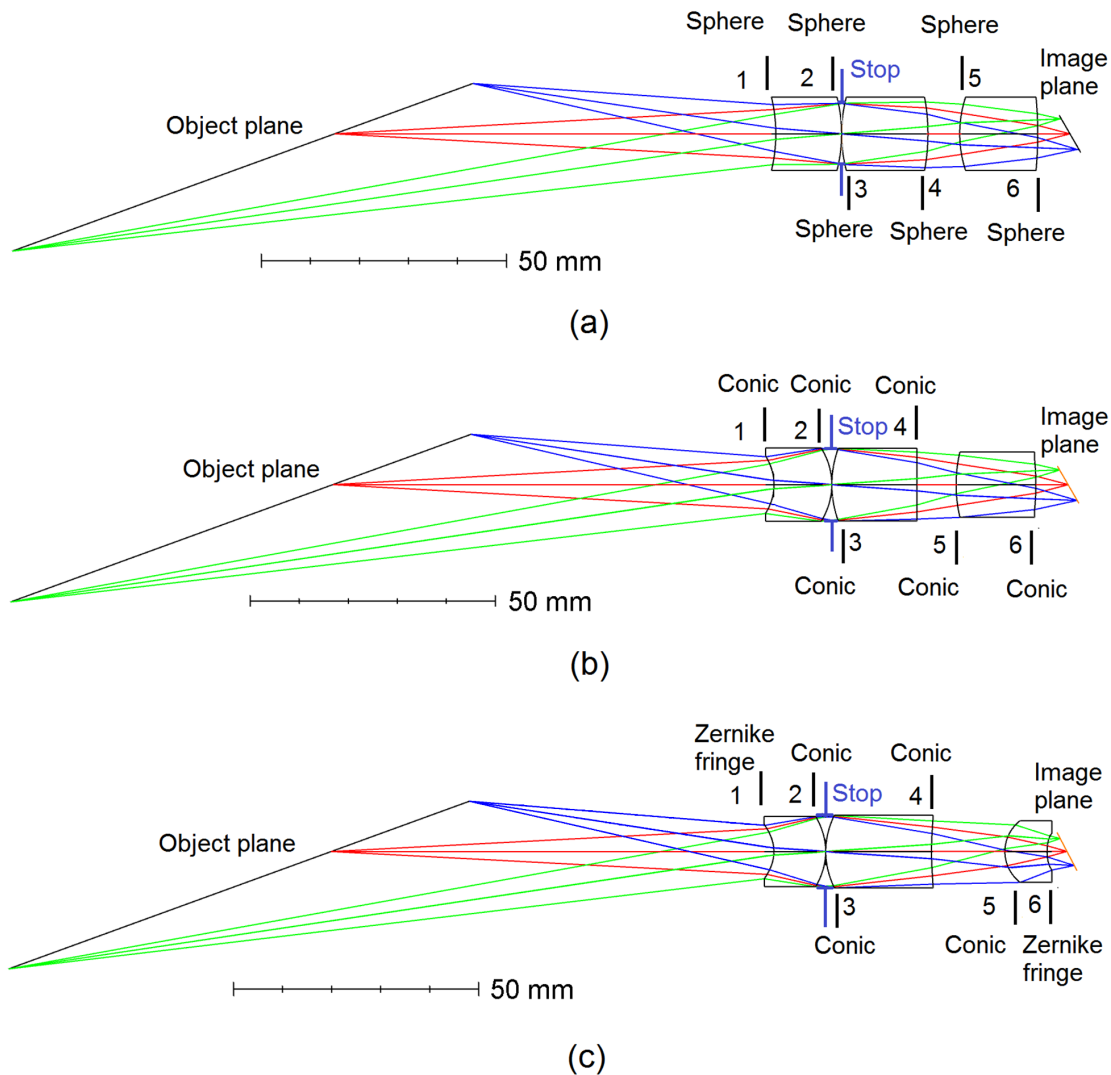


Figure 4-13 Design layout of the Scheimpflug system (a) Starting system with spherical surfaces; (b) Intermediate system with conic surfaces; (c) Final design with two Zernike fringe surfaces

According to the surface position selection rules mentioned in Section 3.6, the aberrations generated by the Zernike fringe freeform deformation depend on the Zernike fringe coefficients, the normalization radius, the separation of the ray bundles of different fields, which is the ratio \bar{h}/h of each surface. The ratio \bar{h}/h of

each object distance corresponding to points A, B and C is calculated and shown as bar diagram of all the surfaces in Figure 4-14. The three points A, B, and C correspond to fields of 30mm, 0mm and -70mm in Y^* direction.

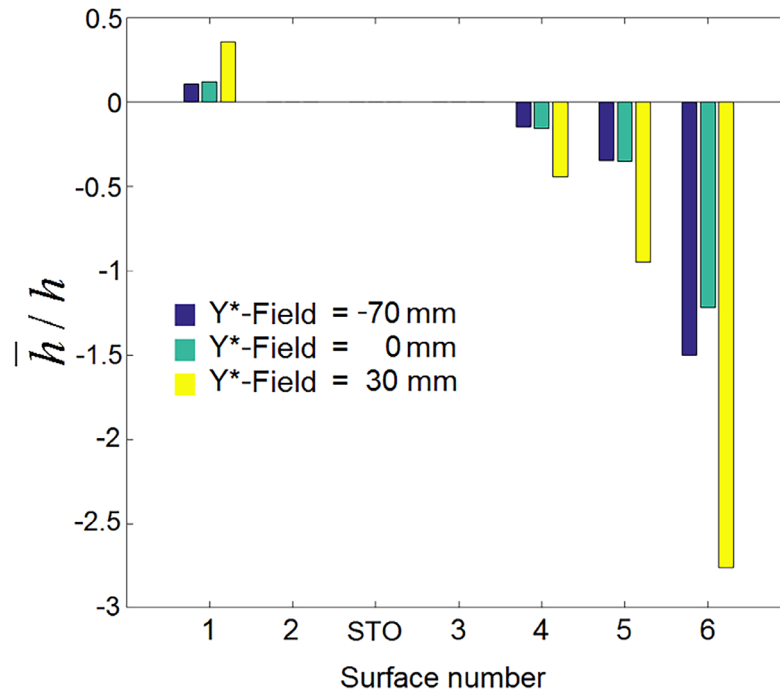


Figure 4-14 Bar diagram of the ratio \bar{h}/h on each surface

Due to the large variance of aberrations over the shift of object distance, the Scheimpflug system suffers from large field-dependent aberrations. Even the spherical aberration is not constant over the FOV. Thus, surfaces 2 and 3 located at the stop position are not the good choices for freeform surfaces. The two freeform surfaces should have large impact on field-dependent aberrations and the difference between the two ratios of \bar{h}/h should be large. Thus, surface 1 and 6 are selected as the freeform surfaces. Both are optimized with the x-direction symmetric Zernike fringe polynomials from term 5 to term 36. The final image quality is evaluated in terms of MTF values of the defined fields as in Figure 4-15(a), which is higher than 0.3 at 100lp/mm. The grid distortion in Figure 4-15(b) shows that the distortion contribution of individual object distance is neglectable compared with the keystone distortion, since the locations of the fields at the same object distance are at the same image height.

The freeform contribution of the surface sag of the two freeform surfaces are shown in Figure 4-16. It is seen that the freeform deviation of both surfaces is smaller than $\pm 3\text{mm}$, which is comfortable for manufacturing.

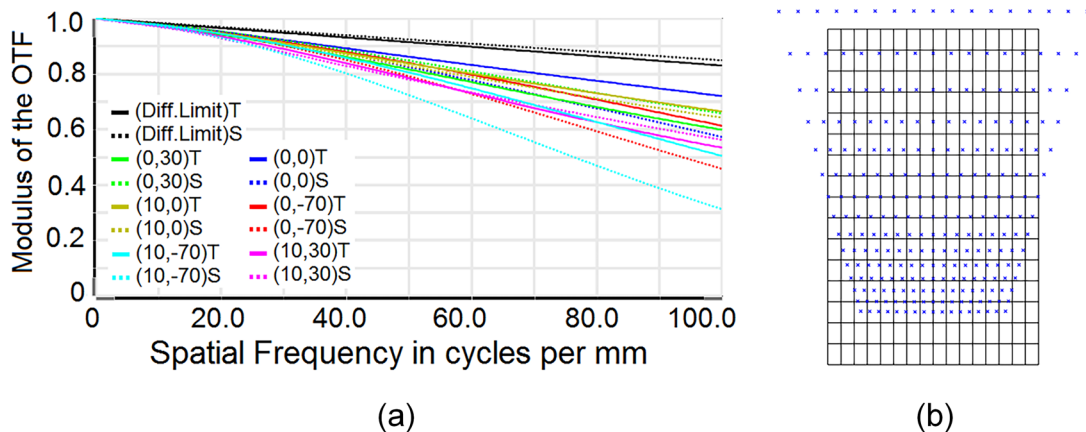


Figure 4-15 (a) MTF performance of the final Scheimpflug system; (b) Grid distortion of the final Scheimpflug system

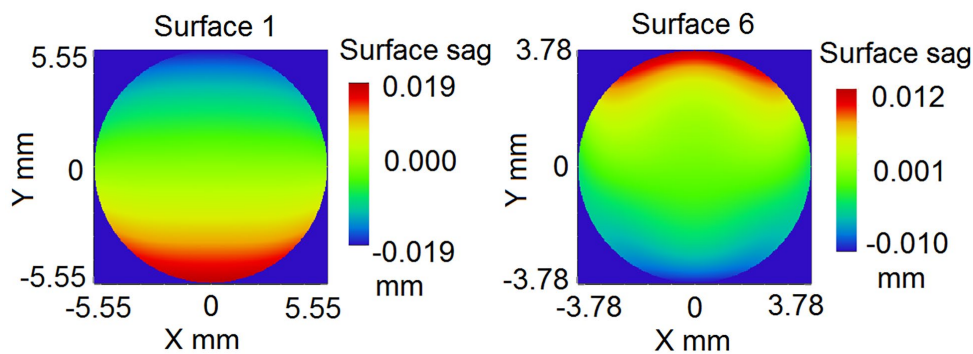


Figure 4-16 Freeform contribution to surface sag of surface 1 (left) and surface 6 (right)

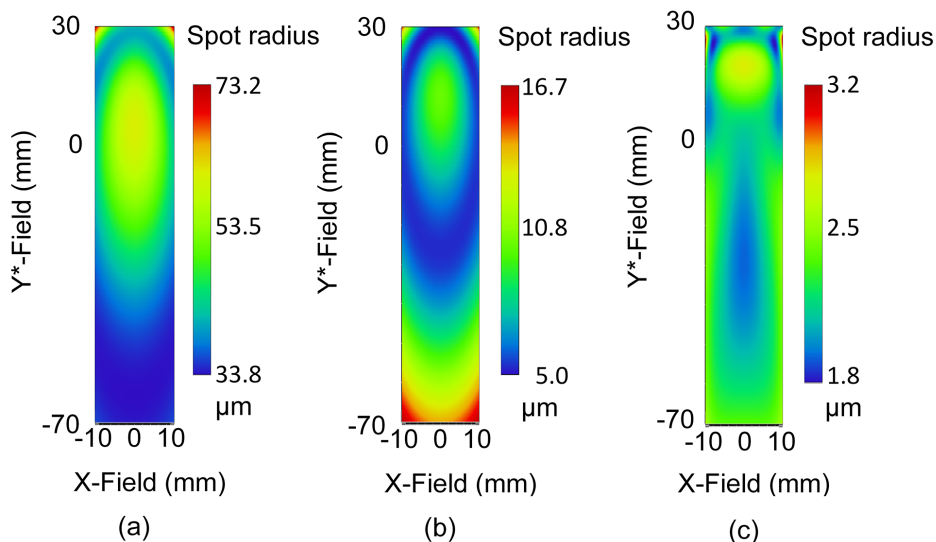


Figure 4-17 RMS spot radius vs field map of the system (a) Starting system with spherical surfaces; (b) Intermediate system with conic surfaces; (c) Final design with two Zernike fringe surfaces

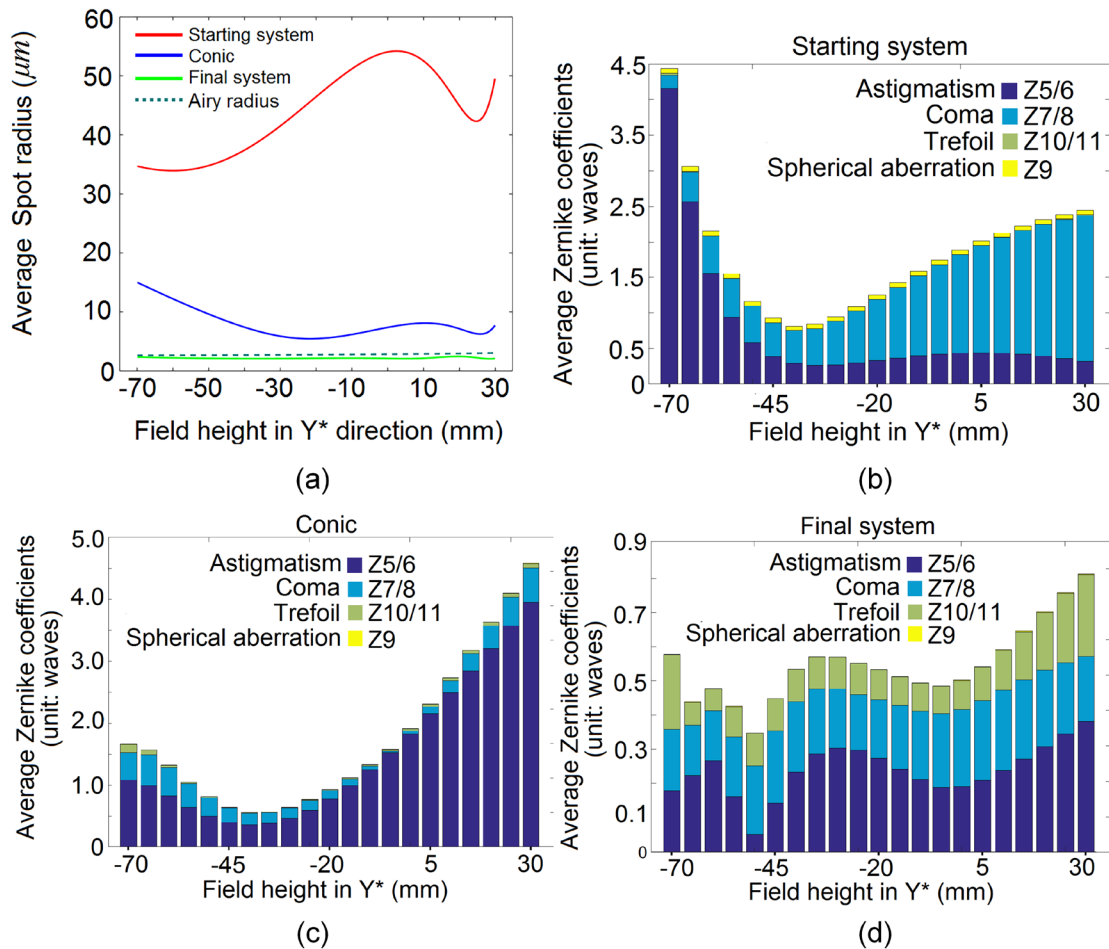


Figure 4-18 (a) Average RMS spot radius vs field height in Y^* ; Bar diagram of average Zernike fringe aberration coefficients vs field height in Y^* for (b) the starting system, (c) the intermediate system, and (d) the final system

The RMS spot radius map with the FOV of the three systems in Figure 4-13 are shown in Figure 4-17. It is seen that the resolution is greatly improved by adding the freeform surfaces. The improvement of the resolution and the uniformity over the object distance shift are observed by calculating the average RMS spot radius and the average magnitude of the Zernike fringe aberrations as astigmatism (Z5/6), coma (Z7/8), trefoil (Z10/11), and spherical aberration (Z9) of the three systems in Figure 4-13 with respect to different object distances. The magnitude of the aberration is calculated as the square root of sum of squares of the two components as

$$Z_{a/b} = \sqrt{Z_a^2 + Z_b^2}. \tag{4-3}$$

The whole field is sampled with I points in X direction and J points in Y* direction. For the sampling of the RMS spot radius, I=J=200. For the sampling of the aberrations, I=100 and J=21. The value of each sampling point is defined as $V_{i,j}$. The average value of each object distance is calculated following:

$$V_j^{Average} = \sum_{i=1}^I V_{i,j} / I. \quad (4-4)$$

The plots of the average values with respect to different object distance are shown in Figure 4-18. The average spot radius of the whole FOV is also calculated and listed in Table 4-9 to show the improvement of resolution.

Table 4-9 Analysis of RMS spot radius for the three systems

	Starting system	Intermediate system (conic)	Final system
Minimum value of the whole FOV (μm)	33.8	5.0	1.8
Maximum value of the whole FOV (μm)	73.2	16.7	3.2
Average value of the whole FOV (μm)	43.6	8.0	2.2

It is shown in Figure 4-18(b) that the starting system suffers from large and non-uniform astigmatism and coma. For the far object distance ($Y^*=-70\text{mm}$), it suffers more from astigmatism, while for near object distance ($Y^*=30\text{mm}$), it suffers more from coma due to the larger NA and larger angle of the chief ray, which are the main problems of classical Scheimpflug systems. Spherical aberration is optimized in the initial design procedure. Thus, it is smaller and more uniform compared with coma and astigmatism. Using conic surfaces, spherical aberration and coma are better corrected as shown in Figure 4-18(c). However, coma and astigmatism of generated by a conic surface are coupled. When coma is compensated, the conic surfaces also generate large astigmatism. Since freeform surfaces allow decoupling in coma and astigmatism, all the primary aberrations are better corrected and uniformed in the final system as in Figure 4-18(d). The aberration analysis explains the improvement of system performance and the uniformity in Figure 4-18(a). The final system has uniform RMS spot radius along the object distance shift, which is smaller than the Airy radius.

5 Conclusions

In this work, several goals are accomplished for the design of non-rotationally symmetric systems. An initial system design method based on Gaussian brackets and NAT is proposed, which has no limitation of surface number and concerning the refractive or reflective surface types. This method can be applied to both non-rotationally symmetric systems and centered systems. The stop position can be defined arbitrarily in this method. The initial setup is designed with spherical surfaces. When adding freeform surfaces, the vertex of geometry can be selected at an arbitrary point on the surface. The primary aberrations and first-order properties are derived analytically and optimized by nonlinear least-squares solver. By setting proper boundary values of the tilt angles in the optimization procedure, it is possible to avoid obscuration.

The already existing design method using confocal conic surface is also further investigated and extended in this work. The whole design procedure is introduced in detail. The Petzval vanishing condition is added to the method. The condition to obtain no obscuration is also discussed. Following the steps, it is possible to design an initial setup of the off-axis mirror system with sharp image in the center of the field of view and the linear astigmatism corrected.

It is necessary to understand the system performance by analyzing the aberrations in the system. In traditional systems, the surface contributions of aberrations are presented by Seidel aberration coefficients. Instead of Seidel coefficients, in non-rotationally symmetric systems, the aberration contribution of each surface can be obtained by the vectorial representation. The aberrations are related with both the field height and the tilt of the surface, since the tilt introduces a shift factor to the field. The field shift vectors have different impact on each aberration. In this work, the design strategies are concluded by proper rotating the surfaces to obtain nodal points based on NAT. In recent years, NAT is extended to the applications with freeform surfaces. Thus, the impact of freeform surfaces at different locations of the system can be analyzed. In this work, the surface selection rules of freeform surfaces are concluded based on the extension of NAT. For different types of systems, the design strategy and surface selection are completely different.

The biconic surface shape is used nowadays in anamorphic systems and as the basic shape in the freeform surface representations. In this work, the primary aberrations of biconic surfaces are derived following the Seidel aberration theory, vectorial aberration theory, and the extension of NAT of freeform surfaces. The biconic surface is converted into a traditional freeform surface representation with spherical part, conic part (or aspherical part), and the freeform part up to the 4th order. The total influence on the wavefront is the sum of the aberrations generated by the different parts of the surface. The aberrations are given in vectorial representation. Compared with the conventional conic surface, the biconic surface provides two additional degrees of freedom with different curvatures and conic parameters in x- and y-direction, which allow the possibility to correct primary aberrations as spherical aberration, coma, and primary astigmatism as well as secondary astigmatism. It is shown that only freeform surfaces allow a decoupling of coma and astigmatism.

With the design procedure following the initial setup establishment, system aberration analysis, surface position evaluation, and surface selection, the non-rotationally symmetric system with freeform surfaces is designed more effectively. The behavior of the system performance is better studied. The system structure can be simplified according to the request to reduce the cost and difficulty in manufacturing. It is shown in the applications that a small f-number of an extended Yolo telescope system can be achieved, and in Scheimpflug systems the uniformity of the performance over the object distance shift can be balanced only with freeform surfaces.

The work in this dissertation solves some of the problems in the design of non-rotationally symmetric systems. In the future, the aberrations in more types of systems can be studied. The aberrations generated by other freeform surface representations can also be derived. Although it is mentioned that the same freeform surface sag can be represented by different polynomials, the impact of different terms is different. During the design process, the freeform terms are added step by step. Thus, the final system could end up with different performance after local optimization, if different freeform surface representations are used. The reason of the difference will be clearer if the aberrations generated by the terms are derived, which also gives certain hints in the selection of freeform surface representations.

Appendix A: Vector relations

As mentioned in Section 2.2 and Section 2.3, in order to unify the definition of the azimuthal angle in the vectorial wave aberration representation and in the freeform surface representation, the definition of the azimuthal angle is illustrated as in Figure 2-4. Thus, the vector representation in Euler's formula is modified. The properties of the vector dot product and the vector multiplication are modified as follows.

The two components of the vectors can be represented as:

$$\vec{A} = ae^{i\alpha} = a_x \hat{i} + a_y \hat{j} \quad (a_x = a \cos \alpha; \quad a_y = a \sin \alpha) \quad (\text{A-1})$$

$$\vec{B} = be^{i\alpha} = b_x \hat{i} + b_y \hat{j} \quad (b_x = b \cos \alpha; \quad b_y = b \sin \alpha) \quad (\text{A-2})$$

a) Dot product:

$$\vec{A} \cdot \vec{A} = a^2 \quad (\text{A-3})$$

$$\vec{A} \cdot \vec{B} = ab \cos(\alpha - \beta) = a_x b_x + a_y b_y \quad (\text{A-4})$$

b) Vector Multiplication:

$$\vec{A}\vec{B} = abe^{i(\alpha+\beta)} = (\vec{A}\vec{B})_x \hat{i} + (\vec{A}\vec{B})_y \hat{j} \quad (\text{A-5})$$

$$(\vec{A}\vec{B})_x = ab \cos(\alpha + \beta) = a \cos \alpha \cdot b \cos \beta - a \sin \alpha \cdot b \sin \beta = a_x b_x - a_y b_y \quad (\text{A-6})$$

$$(\vec{A}\vec{B})_y = ab \sin(\alpha + \beta) = a \sin \alpha \cdot b \cos \beta + a \cos \alpha \cdot b \sin \beta = a_y b_x + a_x b_y \quad (\text{A-7})$$

c) Squared Vector:

$$\vec{A}^2 = a^2 e^{i2\alpha} = (\vec{A}^2)_x \hat{i} + (\vec{A}^2)_y \hat{j} \quad (\text{A-8})$$

$$(\vec{A}^2)_x = a^2 \cos(2\alpha) = a^2 \cos^2 \alpha - a^2 \sin^2 \alpha = a_x^2 - a_y^2 \quad (\text{A-9})$$

$$(\vec{A}^2)_y = a^2 \sin(2\alpha) = 2a^2 \sin \alpha \cos \alpha = 2a_x a_y \quad (\text{A-10})$$

d) Cubic Vector:

$$\vec{A}^3 = a^3 e^{i3\alpha} = (\vec{A}^3)_x \hat{i} + (\vec{A}^3)_y \hat{j} \quad (\text{A-11})$$

$$(\vec{A}^3)_x = a^3 \cos(3\alpha) = a^3 \cos^3 \alpha - 3a^3 \sin^2 \alpha \cos \alpha = a_x^3 - 3a_y^2 a_x \quad (\text{A-12})$$

$$(\vec{A}^3)_y = a^3 \sin(3\alpha) = 3a^3 \sin \alpha \cos^2 \alpha - a^3 \sin^3 \alpha = 3a_y a_x^2 - a_y^3 \quad (\text{A-13})$$

e) Vector conjugates:

$$\vec{A}^* = ae^{-i\alpha} = a_x \hat{i} - a_y \hat{j} \quad (\text{A-14})$$

$$\vec{AB}^* = abe^{i(\alpha-\beta)} = (\vec{AB}^*)_x \hat{i} + (\vec{AB}^*)_y \hat{j} = \vec{A} \cdot \vec{B} \quad (\text{A-15})$$

$$(\vec{AB}^*)_x = ab \cos(\alpha - \beta) = ab \cos \alpha \cos \beta + ab \sin \alpha \sin \beta = a_x b_x + a_y b_y \quad (\text{A-16})$$

$$(\vec{AB}^*)_y = ab \sin(\alpha - \beta) = ab \sin \alpha \cos \beta - ab \cos \alpha \sin \beta = a_y b_x - a_x b_y \quad (\text{A-17})$$

f) Vector Identities:

$$2(\vec{A} \cdot \vec{B})(\vec{A} \cdot \vec{C}) = (\vec{A} \cdot \vec{A})(\vec{B} \cdot \vec{C}) + \vec{A}^2 \cdot \vec{BC} \quad (\text{A-18})$$

$$\vec{A} \cdot \vec{BC} = \vec{AB}^* \cdot \vec{C} \quad (\text{A-19})$$

$$2(\vec{A} \cdot \vec{B})(\vec{AB} \cdot \vec{C}^2) = (\vec{A} \cdot \vec{A})(\vec{B}^2 \cdot \vec{C}^2) + (\vec{B} \cdot \vec{B})(\vec{A}^2 \cdot \vec{C}^2) \quad (\text{A-20})$$

$$2(\vec{A} \cdot \vec{B})(\vec{A}^2 \cdot \vec{C}^2) = (\vec{A} \cdot \vec{A})(\vec{AB} \cdot \vec{C}^2) + \vec{A}^3 \cdot \vec{BC}^2 \quad (\text{A-21})$$

Appendix B: Aberrations generated by Zernike fringe freeform polynomials

When the freeform surface is located away from the pupil, the aberrations generated by the term from 2 to 16 of Zernike fringe polynomials are derived following the relations of Eqs. (3-33)-(3.37) and Eq. (3-31) and listed below. The piston term is always neglected in the tables.

Terms 2 and 3:

$$\Delta W_{2/3} = \bar{M}_{2/3} \cdot \left(\frac{h}{r_{norm}} \right) (\bar{\rho} + \Delta \bar{h}) = \left(\frac{h}{r_{norm}} \right) \bar{M}_{2/3} \cdot \bar{\rho} + \left(\frac{\bar{h}}{r_{norm}} \right) \bar{M}_{2/3} \cdot \bar{H} \quad (\text{B-1})$$

Table B-1 Wavefront deformation generated by terms 2 and 3

Deformation	Vectorial representation
Tilt	$\left(\frac{h}{r_{norm}} \right) \bar{M}_{2/3} \cdot \bar{\rho}$

Term 4:

$$\begin{aligned} \Delta W_4 &= 2M_4 \left(\frac{h}{r_{norm}} \right)^2 (\bar{\rho} + \Delta \bar{h}) \cdot (\bar{\rho} + \Delta \bar{h}) \\ &= 2M_4 \left(\frac{h}{r_{norm}} \right)^2 (\bar{\rho} \cdot \bar{\rho}) + 4M_4 \left(\frac{h\bar{h}}{r_{norm}^2} \right) (\bar{H} \cdot \bar{\rho}) + 2M_4 \left(\frac{\bar{h}}{r_{norm}} \right)^2 (\bar{H} \cdot \bar{H}) \end{aligned} \quad (\text{B-2})$$

Table B-2 Wavefront deformation generated by term 4

Deformation	Vectorial representation
Defocus	$2M_4 \left(\frac{h}{r_{norm}} \right)^2 (\bar{\rho} \cdot \bar{\rho})$
Change of magnification	$4M_4 \left(\frac{h\bar{h}}{r_{norm}^2} \right) (\bar{H} \cdot \bar{\rho})$

Terms 5 and 6:

$$\begin{aligned}
\Delta W_{5/6} &= \bar{M}_{5/6} \cdot \left[\left(\frac{h}{r_{norm}} \right) (\bar{\rho} + \Delta \bar{h}) \right]^2 \\
&= \left(\frac{h}{r_{norm}} \right)^2 \bar{M}_{5/6} \cdot \bar{\rho}^2 + 2 \left(\frac{h}{r_{norm}} \right)^2 \left(\frac{\bar{h}}{h} \right) \bar{M}_{5/6} \cdot \bar{H} \bar{\rho} \\
&\quad + \left(\frac{h}{r_{norm}} \right)^2 \left(\frac{\bar{h}}{h} \right)^2 \bar{M}_{5/6} \cdot \bar{H}^2 \\
&= \left(\frac{h}{r_{norm}} \right)^2 \bar{M}_{5/6} \cdot \bar{\rho}^2 + 2 \left(\frac{\bar{h}h}{r_{norm}^2} \right) \bar{M}_{5/6} \bar{H}^* \cdot \bar{\rho} \\
&\quad + \left(\frac{\bar{h}}{r_{norm}} \right)^2 \bar{M}_{5/6} \cdot \bar{H}^2
\end{aligned} \tag{B-3}$$

astigmatism, primary *change of magnification*

Table B-3 Wavefront deformation generated by terms 5 and 6

Deformation	Vectorial representation
Astigmatism	$\left(\frac{h}{r_{norm}} \right)^2 \bar{M}_{5/6} \cdot \bar{\rho}^2$
Change of magnification	$2 \left(\frac{\bar{h}h}{r_{norm}^2} \right) \bar{M}_{5/6} \bar{H}^* \cdot \bar{\rho}$

Terms 7 and 8:

$$\begin{aligned}
\Delta W_{7/8} &= 3 \left[\left(\frac{h}{r_{norm}} \right)^2 (\bar{\rho} + \Delta \bar{h}) \cdot (\bar{\rho} + \Delta \bar{h}) \right] \left[\bar{M}_{7/8} \cdot \left(\frac{h}{r_{norm}} \right) (\bar{\rho} + \Delta \bar{h}) \right] \\
&\quad - 2 \left[\bar{M}_{7/8} \cdot \left(\frac{h}{r_{norm}} \right) (\bar{\rho} + \Delta \bar{h}) \right] \\
&= 3 \left(\frac{h}{r_{norm}} \right)^3 (\bar{M}_{7/8} \cdot \bar{\rho}) (\bar{\rho} \cdot \bar{\rho}) + 6 \left(\frac{\bar{h}h^2}{r_{norm}^3} \right) (\bar{M}_{7/8} \cdot \bar{H}) (\bar{\rho} \cdot \bar{\rho}) \\
&\quad + 3 \left(\frac{\bar{h}h^2}{r_{norm}^3} \right) (\bar{M}_{7/8} \bar{H} \cdot \bar{\rho}^2) + 6 \left(\frac{\bar{h}^2 h}{r_{norm}^3} \right) (\bar{H} \cdot \bar{H}) (\bar{M}_{7/8} \cdot \bar{\rho}) \\
&\quad + 3 \left(\frac{\bar{h}^2 h}{r_{norm}^3} \right) (\bar{H}^2 \bar{M}_{7/8}^* \cdot \bar{\rho}) + 3 \left(\frac{\bar{h}}{r_{norm}} \right)^3 (\bar{H} \cdot \bar{H}) (\bar{M}_{7/8} \cdot \bar{H}) \\
&\quad - 2 \left(\frac{h}{r_{norm}} \right) \bar{M}_{7/8} \cdot \bar{\rho} - 2 \left(\frac{\bar{h}}{r_{norm}} \right) (\bar{M}_{7/8} \cdot \bar{H})
\end{aligned} \tag{B-4}$$

coma *focal plane of medial astigmatism*
astigmatism *distortion*
distortion
tilt

Table B-4 Wavefront deformation generated by terms 7 and 8

Deformation	Vectorial representation
Coma	$3\left(\frac{h}{r_{norm}}\right)^3 (\vec{M}_{7/8} \cdot \vec{\rho})(\vec{\rho} \cdot \vec{\rho})$
Astigmatism	$3\left(\frac{\bar{h}h^2}{r_{norm}^3}\right) (\vec{M}_{7/8} \vec{H} \cdot \vec{\rho}^2)$
Focal plane of medial astigmatism	$6\left(\frac{\bar{h}h^2}{r_{norm}^3}\right) (\vec{M}_{7/8} \cdot \vec{H})(\vec{\rho} \cdot \vec{\rho})$
Distortion (including tilt)	$6\left(\frac{\bar{h}^2 h}{r_{norm}^3}\right) (\vec{H} \cdot \vec{H})(\vec{M}_{7/8} \cdot \vec{\rho})$ $+3\left(\frac{\bar{h}^2 h}{r_{norm}^3}\right) (\vec{H}^2 \vec{M}_{7/8}^* \cdot \vec{\rho}) - 2\left(\frac{h}{r_{norm}}\right) \vec{M}_{7/8} \cdot \vec{\rho}$

Term 9:

$$\begin{aligned}
\Delta W_9 &= 6M_9 \left(\frac{h}{r_{norm}}\right)^4 \left[(\vec{\rho} + \Delta \vec{h}) \cdot (\vec{\rho} + \Delta \vec{h}) \right]^2 \\
&\quad - 6M_9 \left(\frac{h}{r_{norm}}\right)^2 (\vec{\rho} + \Delta \vec{h}) \cdot (\vec{\rho} + \Delta \vec{h}) \\
&= 6M_9 \left(\frac{h}{r_{norm}}\right)^4 (\vec{\rho} \cdot \vec{\rho})^2 + 12M_9 \left(\frac{\bar{h}^2 h^2}{r_{norm}^4}\right) (\vec{H}^2 \cdot \vec{\rho}^2) \\
&\quad \text{spherical aberration} \qquad \qquad \qquad \text{astigmatism} \\
&\quad + 6M_9 \left(\frac{\bar{h}}{r_{norm}}\right)^4 (\vec{H} \cdot \vec{H})^2 + 24M_9 \left(\frac{\bar{h}h^3}{r_{norm}^4}\right) (\vec{H} \cdot \vec{\rho})(\vec{\rho} \cdot \vec{\rho}) \\
&\quad \qquad \qquad \qquad \qquad \qquad \qquad \qquad \qquad \qquad \qquad \qquad \text{coma} \\
&\quad + 24M_9 \left(\frac{\bar{h}^3 h}{r_{norm}^4}\right) (\vec{H} \cdot \vec{H})(\vec{H} \cdot \vec{\rho}) + 24M_9 \left(\frac{\bar{h}^2 h^2}{r_{norm}^4}\right) (\vec{H} \cdot \vec{H})(\vec{\rho} \cdot \vec{\rho}) \\
&\quad \qquad \qquad \qquad \qquad \qquad \qquad \qquad \qquad \qquad \qquad \qquad \text{distortion} \qquad \qquad \qquad \text{focal plane of medial astigmatism} \\
&\quad - 6M_9 \left(\frac{h}{r_{norm}}\right)^2 (\vec{\rho} \cdot \vec{\rho}) - 12M_9 \left(\frac{\bar{h}h}{r_{norm}^2}\right) (\vec{H} \cdot \vec{\rho}) - 6M_9 \left(\frac{\bar{h}}{r_{norm}}\right)^2 (\vec{H} \cdot \vec{H}) \\
&\quad \qquad \qquad \qquad \qquad \qquad \qquad \qquad \qquad \qquad \qquad \qquad \text{defocus} \qquad \qquad \qquad \text{change of magnification}
\end{aligned} \tag{B-5}$$

Table B-5 Wavefront deformation generated by terms 9

Deformation	Vectorial representation
Spherical aberration	$6M_9 \left(\frac{h}{r_{norm}} \right)^4 (\vec{\rho} \cdot \vec{\rho})^2$
Coma	$24M_9 \left(\frac{\bar{h}h^3}{r_{norm}^4} \right) (\vec{H} \cdot \vec{\rho}) (\vec{\rho} \cdot \vec{\rho})$
Astigmatism	$12M_9 \left(\frac{\bar{h}^2 h^2}{r_{norm}^4} \right) (\vec{H}^2 \cdot \vec{\rho}^2)$
Focal plane of medial astigmatism	$24M_9 \left(\frac{\bar{h}^2 h^2}{r_{norm}^4} \right) (\vec{H} \cdot \vec{H}) (\vec{\rho} \cdot \vec{\rho})$
Distortion	$24M_9 \left(\frac{\bar{h}^3 h}{r_{norm}^4} \right) (\vec{H} \cdot \vec{H}) (\vec{H} \cdot \vec{\rho})$
Change of magnification	$-12M_9 \left(\frac{\bar{h}h}{r_{norm}^2} \right) (\vec{H} \cdot \vec{\rho})$
Defocus	$-6M_9 \left(\frac{h}{r_{norm}} \right)^2 (\vec{\rho} \cdot \vec{\rho})$

Terms 10 and 11:

$$\begin{aligned}
\Delta W_{10/11} &= \bar{M}_{10/11} \cdot \left(\frac{h}{r_{norm}} \right)^3 (\vec{\rho} + \Delta \bar{h})^3 \\
&= \left(\frac{h}{r_{norm}} \right)^3 \bar{M}_{10/11} \cdot \vec{\rho}^3 + 3 \left(\frac{\bar{h}h^2}{r_{norm}^3} \right) \bar{M}_{10/11} \vec{H}^* \cdot \vec{\rho}^2 \\
&\quad + 3 \left(\frac{\bar{h}^2 h}{r_{norm}^3} \right) \bar{M}_{10/11} (\vec{H}^*)^2 \cdot \vec{\rho} + \bar{M}_{10/11} \left(\frac{\bar{h}}{r_{norm}} \right)^3 \cdot \vec{H}^3
\end{aligned} \tag{B-6}$$

Table B-6 Wavefront deformation generated by terms 10 and 11

Deformation	Vectorial representation
Trefoil	$\left(\frac{h}{r_{norm}} \right)^3 \bar{M}_{10/11} \cdot \vec{\rho}^3$
Astigmatism	$3 \left(\frac{\bar{h}h^2}{r_{norm}^3} \right) \bar{M}_{10/11} \vec{H}^* \cdot \vec{\rho}^2$
Distortion	$3 \left(\frac{\bar{h}^2 h}{r_{norm}^3} \right) \bar{M}_{10/11} (\vec{H}^*)^2 \cdot \vec{\rho}$

Terms 12 and 13:

$$\begin{aligned}
\Delta W_{12/13} &= 4 \left[\bar{M}_{12/13} \cdot \left(\frac{h}{r_{norm}} \right)^2 (\bar{\rho} + \Delta \bar{h})^2 \right] \left[\left(\frac{h}{r_{norm}} \right)^2 (\bar{\rho} + \Delta \bar{h}) \cdot (\bar{\rho} + \Delta \bar{h}) \right] \\
&\quad - 3 \bar{M}_{12/13} \cdot \left[\left(\frac{h}{r_{norm}} \right) (\bar{\rho} + \Delta \bar{h}) \right]^2 \\
&= 4 \left(\frac{h}{r_{norm}} \right)^4 \underbrace{\left(\bar{M}_{12/13} \cdot \bar{\rho}^2 \right)}_{\text{Astigmatism, Secondary}} (\bar{\rho} \cdot \bar{\rho}) - 3 \left(\frac{h}{r_{norm}} \right)^2 \underbrace{\bar{M}_{12/13} \cdot \bar{\rho}^2}_{\text{astigmatism}} \\
&\quad + 12 \left(\frac{\bar{h} h^3}{r_{norm}^4} \right) \underbrace{\left(\bar{M}_{12/13} \bar{H}^* \cdot \bar{\rho} \right)}_{\text{coma}} (\bar{\rho} \cdot \bar{\rho}) \\
&\quad + 4 \left(\frac{\bar{h} h^3}{r_{norm}^4} \right) \underbrace{\bar{H} \bar{M}_{12/13} \cdot \bar{\rho}^{-3}}_{\text{trefoil}} \\
&\quad + 12 \left(\frac{\bar{h}^2 h^2}{r_{norm}^4} \right) \underbrace{(\bar{H} \cdot \bar{H})}_{\text{astigmatism}} \left(\bar{M}_{12/13} \cdot \bar{\rho}^2 \right) \\
&\quad - 6 \left(\frac{\bar{h} h}{r_{norm}^2} \right) \underbrace{\left(\bar{M}_{12/13} \bar{H}^* \cdot \bar{\rho} \right)}_{\text{change of magnification}} \\
&\quad + 12 \left(\frac{\bar{h}^2 h^2}{r_{norm}^4} \right) \underbrace{\left(\bar{M}_{12/13} \cdot \bar{H}^2 \right)}_{\text{focal plane of medial astigmatism}} (\bar{\rho} \cdot \bar{\rho}) \\
&\quad + 12 \left(\frac{\bar{h}^3 h}{r_{norm}^4} \right) \underbrace{(\bar{H} \cdot \bar{H})}_{\text{distortion}} \left(\bar{M}_{12/13} \bar{H}^* \cdot \bar{\rho} \right) \\
&\quad - 3 \left(\frac{\bar{h}^2 h^2}{r_{norm}^4} \right) \left(\bar{M}_{12/13} \cdot \bar{H}^2 \right) \\
&\quad + 4 \left(\frac{\bar{h}^3 h}{r_{norm}^4} \right) \underbrace{\left[\bar{H}^2 \left(\bar{M}_{12/13} \bar{H}^* \right)^* \cdot \bar{\rho} \right]}_{\text{distortion}} \\
&\quad + 4 \left(\frac{\bar{h}}{r_{norm}} \right)^4 (\bar{H} \cdot \bar{H}) \left(\bar{M}_{12/13} \cdot \bar{H}^2 \right)
\end{aligned} \tag{B-7}$$

Table B-7 Wavefront deformation generated by terms 12 and 13

Deformation	Vectorial representation
Astigmatism, Secondary	$4 \left(\frac{h}{r_{norm}} \right)^4 \left(\vec{M}_{12/13} \cdot \vec{\rho}^2 \right) (\vec{\rho} \cdot \vec{\rho})$
Coma	$12 \left(\frac{\bar{h}h^3}{r_{norm}^4} \right) \left(\vec{M}_{12/13} \vec{H}^* \cdot \vec{\rho} \right) (\vec{\rho} \cdot \vec{\rho})$
Astigmatism	$12 \left(\frac{\bar{h}^2 h^2}{r_{norm}^4} \right) (\vec{H} \cdot \vec{H}) \left(\vec{M}_{12/13} \cdot \vec{\rho}^2 \right) - 3 \left(\frac{h}{r_{norm}} \right)^2 \vec{M}_{12/13} \cdot \vec{\rho}^2$
Focal plane of medial astigmatism	$12 \left(\frac{\bar{h}^2 h^2}{r_{norm}^4} \right) \left(\vec{M}_{12/13} \cdot \vec{H}^2 \right) (\vec{\rho} \cdot \vec{\rho})$
Distortion	$12 \left(\frac{\bar{h}^3 h}{r_{norm}^4} \right) (\vec{H} \cdot \vec{H}) \left(\vec{M}_{12/13} \vec{H}^* \cdot \vec{\rho} \right)$ $+ 4 \left(\frac{\bar{h}^3 h}{r_{norm}^4} \right) \left[\vec{H}^2 \left(\vec{M}_{12/13} \vec{H}^* \right)^* \cdot \vec{\rho} \right]$
Change of magnification	$-6 \left(\frac{\bar{h}h}{r_{norm}^2} \right) \left(\vec{M}_{12/13} \vec{H}^* \cdot \vec{\rho} \right)$
Trefoil	$4 \left(\frac{\bar{h}h^3}{r_{norm}^4} \right) \vec{H} \vec{M}_{12/13} \cdot \vec{\rho}^3$

Terms 14 and 15:

$$\begin{aligned}
\Delta W_{14/15} &= 10 \left(\frac{h}{r_{norm}} \right)^5 \left[(\vec{\rho} + \Delta \vec{h}) \cdot (\vec{\rho} + \Delta \vec{h}) \right]^2 \left[\bar{M}_{14/15} \cdot (\vec{\rho} + \Delta \vec{h}) \right] \\
&\quad - 12 \left(\frac{h}{r_{norm}} \right)^3 \left[(\vec{\rho} + \Delta \vec{h}) \cdot (\vec{\rho} + \Delta \vec{h}) \right] \left[\bar{M}_{14/15} \cdot (\vec{\rho} + \Delta \vec{h}) \right] \\
&\quad + 3 \bar{M}_{14/15} \cdot \left(\frac{h}{r_{norm}} \right) (\vec{\rho} + \Delta \vec{h}) \\
&= 10 \left(\frac{h}{r_{norm}} \right)^5 \left(\bar{M}_{14/15} \cdot \vec{\rho} \right) (\vec{\rho} \cdot \vec{\rho})^2 \\
&\quad \text{coma, secondary} \\
&\quad + 60 \left(\frac{\bar{h}^2 h^3}{r_{norm}^5} \right) (\bar{H} \cdot \bar{H}) (\bar{M}_{14/15} \cdot \vec{\rho}) (\vec{\rho} \cdot \vec{\rho}) \\
&\quad \text{coma} \\
&\quad + 30 \left(\frac{\bar{h}^2 h^3}{r_{norm}^5} \right) (\bar{H}^2 \bar{M}_{14/15}^* \cdot \vec{\rho}) (\vec{\rho} \cdot \vec{\rho}) \\
&\quad \text{coma} \\
&\quad - 12 \left(\frac{h}{r_{norm}} \right)^3 (\bar{M}_{14/15} \cdot \vec{\rho}) (\vec{\rho} \cdot \vec{\rho}) \\
&\quad \text{coma} \\
&\quad + 10 \left(\frac{\bar{h}^2 h^3}{r_{norm}^5} \right) (\bar{M}_{14/15} \bar{H}^2 \cdot \vec{\rho}^3) + 30 \left(\frac{\bar{h} h^4}{r_{norm}^5} \right) (\bar{M}_{14/15} \cdot \bar{H}) (\vec{\rho} \cdot \vec{\rho})^2 \\
&\quad \text{trefoil} \qquad \qquad \qquad \text{spherical aberration} \tag{B-8} \\
&\quad + 20 \left(\frac{\bar{h} h^4}{r_{norm}^5} \right) (\bar{M}_{14/15} \bar{H} \cdot \vec{\rho}^2) (\vec{\rho} \cdot \vec{\rho}) \\
&\quad \text{astigmatism, secondary} \\
&\quad + 60 \left(\frac{\bar{h}^3 h^2}{r_{norm}^5} \right) (\bar{H} \cdot \bar{H}) (\bar{M}_{14/15} \cdot \bar{H}) (\vec{\rho} \cdot \vec{\rho}) \\
&\quad \text{focal plane of medial astigmatism} \\
&\quad - 24 \left(\frac{\bar{h} h^2}{r_{norm}^3} \right) (\bar{M}_{14/15} \cdot \bar{H}) (\vec{\rho} \cdot \vec{\rho}) \\
&\quad \text{focal plane of medial astigmatism} \\
&\quad + 30 \left(\frac{\bar{h}^3 h^2}{r_{norm}^5} \right) (\bar{H} \cdot \bar{H}) (\bar{M}_{14/15} \bar{H} \cdot \vec{\rho}^2) \\
&\quad \text{astigmatism} \\
&\quad + 10 \left(\frac{\bar{h}^3 h^2}{r_{norm}^5} \right) (\bar{H}^3 \bar{M}_{14/15}^* \cdot \vec{\rho}^2) - 12 \left(\frac{\bar{h} h^2}{r_{norm}^3} \right) (\bar{M}_{14/15} \bar{H} \cdot \vec{\rho}^2) \\
&\quad \text{astigmatism} \qquad \qquad \qquad \text{astigmatism} \\
&\quad + 30 \left(\frac{\bar{h}^4 h}{r_{norm}^5} \right) (\bar{H} \cdot \bar{H})^2 (\bar{M}_{14/15} \cdot \vec{\rho}) \\
&\quad \text{distortion}
\end{aligned}$$

$$\begin{aligned}
& +20 \left(\frac{\bar{h}^4 h}{r_{norm}^5} \right) (\bar{H} \cdot \bar{H}) (\bar{H}^2 \bar{M}_{14/15}^* \cdot \bar{\rho}) \\
& \quad \text{distortion} \\
& -24 \left(\frac{\bar{h}^2 h}{r_{norm}^3} \right) (\bar{H} \cdot \bar{H}) (\bar{M}_{14/15} \cdot \bar{\rho}) - 12 \left(\frac{\bar{h}^2 h}{r_{norm}^3} \right) (\bar{H}^2 \bar{M}_{14/15}^* \cdot \bar{\rho}) \\
& \quad \text{distortion} \qquad \qquad \qquad \text{distortion} \\
& +3 \left(\frac{h}{r_{norm}} \right) \bar{M}_{14/15} \cdot \bar{\rho} + 10 \left(\frac{\bar{h}}{r_{norm}} \right)^5 (\bar{M}_{14/15} \cdot \bar{H}) (\bar{H} \cdot \bar{H})^2 \\
& \quad \text{tilt} \\
& -12 \left(\frac{\bar{h}}{r_{norm}} \right)^3 (\bar{H} \cdot \bar{H}) (\bar{M}_{14/15} \cdot \bar{H}) + 3 \left(\frac{\bar{h}}{r_{norm}} \right) \bar{M}_{14/15} \cdot \bar{H}
\end{aligned}$$

Table B-8 Wavefront deformation generated by terms 14 and 15

Deformation	Vectorial representation
Coma, Secondary	$10 \left(\frac{h}{r_{norm}} \right)^5 (\bar{M}_{14/15} \cdot \bar{\rho}) (\bar{\rho} \cdot \bar{\rho})^2$
Spherical aberration	$30 \left(\frac{\bar{h} h^4}{r_{norm}^5} \right) (\bar{M}_{14/15} \cdot \bar{H}) (\bar{\rho} \cdot \bar{\rho})^2$
Coma	$ \begin{aligned} & 60 \left(\frac{\bar{h}^2 h^3}{r_{norm}^5} \right) (\bar{H} \cdot \bar{H}) (\bar{M}_{14/15} \cdot \bar{\rho}) (\bar{\rho} \cdot \bar{\rho}) \\ & +30 \left(\frac{\bar{h}^2 h^3}{r_{norm}^5} \right) (\bar{H}^2 \bar{M}_{14/15}^* \cdot \bar{\rho}) (\bar{\rho} \cdot \bar{\rho}) \\ & -12 \left(\frac{h}{r_{norm}} \right)^3 (\bar{M}_{14/15} \cdot \bar{\rho}) (\bar{\rho} \cdot \bar{\rho}) \end{aligned} $
Astigmatism	$ \begin{aligned} & 30 \left(\frac{\bar{h}^3 h^2}{r_{norm}^5} \right) (\bar{H} \cdot \bar{H}) (\bar{M}_{14/15} \bar{H} \cdot \bar{\rho}^2) \\ & +10 \left(\frac{\bar{h}^3 h^2}{r_{norm}^5} \right) (\bar{H}^3 \bar{M}_{14/15}^* \cdot \bar{\rho}^2) \\ & -12 \left(\frac{\bar{h} h^2}{r_{norm}^3} \right) (\bar{M}_{14/15} \bar{H} \cdot \bar{\rho}^2) \end{aligned} $
Astigmatism, secondary	$20 \left(\frac{\bar{h} h^4}{r_{norm}^5} \right) (\bar{M}_{14/15} \bar{H} \cdot \bar{\rho}^2) (\bar{\rho} \cdot \bar{\rho})$
Focal plane of medial astigmatism	$ \begin{aligned} & 60 \left(\frac{\bar{h}^3 h^2}{r_{norm}^5} \right) (\bar{H} \cdot \bar{H}) (\bar{M}_{14/15} \cdot \bar{H}) (\bar{\rho} \cdot \bar{\rho}) \\ & -24 \left(\frac{\bar{h} h^2}{r_{norm}^3} \right) (\bar{M}_{14/15} \cdot \bar{H}) (\bar{\rho} \cdot \bar{\rho}) \end{aligned} $

Distortion	$30 \left(\frac{\bar{h}^4 h}{r_{norm}^5} \right) (\bar{H} \cdot \bar{H})^2 (\bar{M}_{14/15} \cdot \bar{\rho})$ $+20 \left(\frac{\bar{h}^4 h}{r_{norm}^5} \right) (\bar{H} \cdot \bar{H}) (\bar{H}^2 \bar{M}_{14/15}^* \cdot \bar{\rho})$ $-24 \left(\frac{\bar{h}^2 h}{r_{norm}^3} \right) (\bar{H} \cdot \bar{H}) (\bar{M}_{14/15} \cdot \bar{\rho})$ $+12 \left(\frac{\bar{h}^2 h}{r_{norm}^3} \right) (\bar{H}^2 \bar{M}_{14/15}^* \cdot \bar{\rho})$
Tilt	$3 \left(\frac{h}{r_{norm}} \right) \bar{M}_{14/15} \cdot \bar{\rho}$
Trefoil	$10 \left(\frac{\bar{h}^2 h^3}{r_{norm}^5} \right) (\bar{M}_{14/15} \bar{H}^2 \cdot \bar{\rho}^3)$

Term 16:

$$\begin{aligned}
\Delta W_{16} &= 20M_{16} \left(\frac{h}{r_{norm}} \right)^6 \left[(\bar{\rho} + \Delta \bar{h}) \cdot (\bar{\rho} + \Delta \bar{h}) \right]^3 \\
&\quad - 30M_{16} \left(\frac{h}{r_{norm}} \right)^4 \left[(\bar{\rho} + \Delta \bar{h}) \cdot (\bar{\rho} + \Delta \bar{h}) \right]^2 \\
&\quad + 12M_{16} \left(\frac{h}{r_{norm}} \right)^2 (\bar{\rho} + \Delta \bar{h}) \cdot (\bar{\rho} + \Delta \bar{h}) \\
&= 20M_{16} \left(\frac{h}{r_{norm}} \right)^6 (\bar{\rho} \cdot \bar{\rho})^3 + 180M_{16} \left(\frac{\bar{h}^2 h^4}{r_{norm}^6} \right) (\bar{H} \cdot \bar{H}) (\bar{\rho} \cdot \bar{\rho})^2 \\
&\quad \text{spherical aberration} \qquad \qquad \qquad \text{spherical aberration} \\
&\quad - 30M_{16} \left(\frac{h}{r_{norm}} \right)^4 (\bar{\rho} \cdot \bar{\rho})^2 \\
&\quad \text{spherical aberration} \\
&\quad + 360M_{16} \left(\frac{\bar{h}^3 h^3}{r_{norm}^6} \right) (\bar{H} \cdot \bar{H}) (\bar{H} \cdot \bar{\rho}) (\bar{\rho} \cdot \bar{\rho}) \\
&\quad \text{coma} \\
&\quad - 120M_{16} \left(\frac{\bar{h} h^3}{r_{norm}^4} \right) (\bar{H} \cdot \bar{\rho}) (\bar{\rho} \cdot \bar{\rho}) \\
&\quad \text{coma} \\
&\quad + 120M_{16} \left(\frac{\bar{h} h^5}{r_{norm}^6} \right) (\bar{\rho} \cdot \bar{\rho})^2 (\bar{H} \cdot \bar{\rho}) + 40M_{16} \left(\frac{\bar{h}^3 h^3}{r_{norm}^6} \right) (\bar{H}^3 \cdot \bar{\rho}^3) \\
&\quad \text{coma, secondary} \qquad \qquad \qquad \text{trefoil} \\
&\quad + 120M_{16} \left(\frac{\bar{h}^2 h^4}{r_{norm}^6} \right) (\bar{H}^2 \cdot \bar{\rho}^2) (\bar{\rho} \cdot \bar{\rho}) \\
&\quad \text{astigmatism, secondary} \\
&\quad + 120M_{16} \left(\frac{\bar{h}^4 h^2}{r_{norm}^6} \right) (\bar{H} \cdot \bar{H}) (\bar{H}^2 \cdot \bar{\rho}^2) \\
&\quad \text{astigmatism} \\
&\quad - 60M_{16} \left(\frac{\bar{h}^2 h^4}{r_{norm}^6} \right) (\bar{H}^2 \cdot \bar{\rho}^2) + 180M_{16} \left(\frac{\bar{h}^4 h^2}{r_{norm}^6} \right) (\bar{H} \cdot \bar{H})^2 (\bar{\rho} \cdot \bar{\rho}) \\
&\quad \text{astigmatism} \qquad \qquad \qquad \text{focal plane of medial astigmatism} \\
&\quad - 120M_{16} \left(\frac{\bar{h}^2 h^2}{r_{norm}^4} \right) (\bar{H} \cdot \bar{H}) (\bar{\rho} \cdot \bar{\rho}) \\
&\quad \text{focal plane of medial astigmatism} \\
&\quad + 120M_{16} \left(\frac{\bar{h}^5 h}{r_{norm}^6} \right) (\bar{H} \cdot \bar{H})^2 (\bar{H} \cdot \bar{\rho}) \\
&\quad \text{distortion}
\end{aligned} \tag{B-9}$$

$$\begin{aligned}
 & -120M_{16} \left(\frac{\bar{h}^3 h}{r_{norm}^4} \right) (\bar{H} \cdot \bar{H}) (\bar{H} \cdot \bar{\rho}) + 12M_{16} \left(\frac{h}{r_{norm}} \right)^2 (\bar{\rho} \cdot \bar{\rho}) \\
 & \quad \text{distortion} \qquad \qquad \qquad \text{defocus} \\
 & + 24M_{16} \left(\frac{\bar{h}h}{r_{norm}^2} \right) (\bar{H} \cdot \bar{\rho}) + 12M_{16} \left(\frac{\bar{h}}{r_{norm}} \right)^2 (\bar{H} \cdot \bar{H}) \\
 & \quad \text{tilt} \\
 & - 30M_{16} \left(\frac{\bar{h}}{r_{norm}} \right)^4 (\bar{H} \cdot \bar{H})^2 + 20M_{16} \left(\frac{\bar{h}}{r_{norm}} \right)^6 (\bar{H} \cdot \bar{H})^3
 \end{aligned}$$

Table B-9 Wavefront deformation generated by term 16

Deformation	Vectorial representation
Spherical aberration	$ \begin{aligned} & 20M_{16} \left(\frac{h}{r_{norm}} \right)^6 (\bar{\rho} \cdot \bar{\rho})^3 \\ & + 180M_{16} \left(\frac{\bar{h}^2 h^4}{r_{norm}^6} \right) (\bar{H} \cdot \bar{H}) (\bar{\rho} \cdot \bar{\rho})^2 \\ & - 30M_{16} \left(\frac{h}{r_{norm}} \right)^4 (\bar{\rho} \cdot \bar{\rho})^2 \end{aligned} $
Coma	$ \begin{aligned} & 360M_{16} \left(\frac{\bar{h}^3 h^3}{r_{norm}^6} \right) (\bar{H} \cdot \bar{H}) (\bar{H} \cdot \bar{\rho}) (\bar{\rho} \cdot \bar{\rho}) \\ & - 120M_{16} \left(\frac{\bar{h}h^3}{r_{norm}^4} \right) (\bar{H} \cdot \bar{\rho}) (\bar{\rho} \cdot \bar{\rho}) \end{aligned} $
Coma, secondary	$ 120M_{16} \left(\frac{\bar{h}h^5}{r_{norm}^6} \right) (\bar{\rho} \cdot \bar{\rho})^2 (\bar{H} \cdot \bar{\rho}) $
Astigmatism	$ \begin{aligned} & 120M_{16} \left(\frac{\bar{h}^4 h^2}{r_{norm}^6} \right) (\bar{H} \cdot \bar{H}) (\bar{H}^2 \cdot \bar{\rho}^2) \\ & - 60M_{16} \left(\frac{\bar{h}^2 h^4}{r_{norm}^6} \right) (\bar{H}^2 \cdot \bar{\rho}^2) \end{aligned} $
Astigmatism, secondary	$ 120M_{16} \left(\frac{\bar{h}^2 h^4}{r_{norm}^6} \right) (\bar{H}^2 \cdot \bar{\rho}^2) (\bar{\rho} \cdot \bar{\rho}) $
Focal plane of medial astigmatism	$ \begin{aligned} & 180M_{16} \left(\frac{\bar{h}^4 h^2}{r_{norm}^6} \right) (\bar{H} \cdot \bar{H})^2 (\bar{\rho} \cdot \bar{\rho}) \\ & - 120M_{16} \left(\frac{\bar{h}^2 h^2}{r_{norm}^4} \right) (\bar{H} \cdot \bar{H}) (\bar{\rho} \cdot \bar{\rho}) \end{aligned} $

Distortion	$120M_{16} \left(\frac{\bar{h}^5 h}{r_{norm}^6} \right) (\bar{H} \cdot \bar{H})^2 (\bar{H} \cdot \bar{\rho})$ $-120M_{16} \left(\frac{\bar{h}^3 h}{r_{norm}^4} \right) (\bar{H} \cdot \bar{H}) (\bar{H} \cdot \bar{\rho})$
Defocus	$12M_{16} \left(\frac{h}{r_{norm}} \right)^2 (\bar{\rho} \cdot \bar{\rho})$
Tilt	$24M_{16} \left(\frac{\bar{h}h}{r_{norm}^2} \right) (\bar{H} \cdot \bar{\rho})$
Trefoil	$40M_{16} \left(\frac{\bar{h}^3 h^3}{r_{norm}^6} \right) (\bar{H}^3 \cdot \bar{\rho}^3)$

Appendix C: Verification of the aberrations generated by the biconic surface

A single centered biconic reflective surface is demonstrated as an example to verify the theoretical aberrations. The surface is located away from the pupil with the data as in Table C-1. The two fields are with field angles 0° and 1° (in y). The object is assumed to be at infinite distance.

Table C-1 Data of the biconic reflective surface

Parameter	Value
$c_x (mm^{-1})$	-0.0100
$c_y (mm^{-1})$	-0.0125
κ_x	-1.0000
κ_y	-0.8000

Due to the large astigmatism of the biconic surface, the circle of least blur is used. The image plane is located at a distance of -43.89mm from the biconic mirror, where the axial field has the minimum spot radius. The system layout in Y-Z plane is illustrated as in Figure C-1.

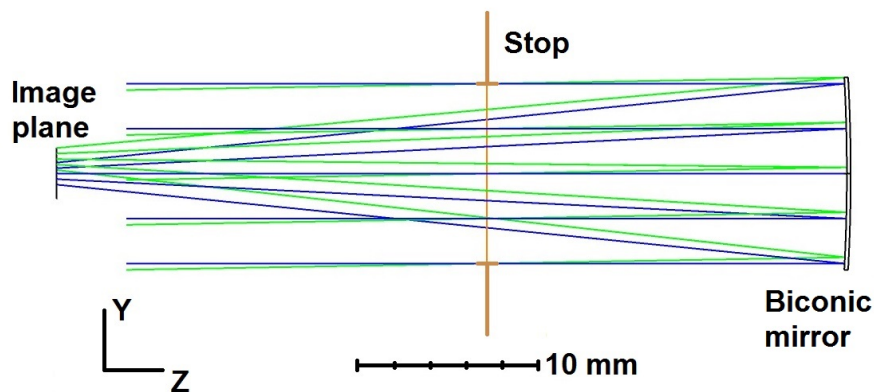


Figure C-1 Biconic reflective mirror

The theoretical aberration values are compared with the Zernike fringe wave aberration coefficients. The theoretical values are calculated according to the aberrations derived in Subsection 3.5.3. If the corresponding wave aberration coefficient of i^{th} term is defined as Z_i , since the higher order Zernike terms also contain lower order terms, the values of higher order terms are also taken into consideration, which are listed in Table C-2. Then the wave aberration coefficients in

Zernike fringe polynomials and the theoretical values of spherical aberration, coma and astigmatism of the off-axis field of 1 degree are listed in Table C-3. The aberration values are all in wavelength unit. The wavelength is set as $1\mu\text{m}$ in the system.

Table C-2 Calculation of wave aberration coefficients using the Zernike fringe coefficients

Aberration	Value in terms of Zernike fringe coefficients
Spherical aberration	$6Z_9 - 30Z_{16} + 90Z_{25}$
Coma (in y)	$3Z_8 - 12Z_{15} + 30Z_{24}$
Astigmatism (axis in 0°)	$Z_5 - 3Z_{12} + 6Z_{21}$

Table C-3 Comparison of the wave aberration value using Zernike fringe polynomials and the theoretical value calculated based on extended nodal aberration theory (in wavelength unit)

Aberration	Zernike fringe wave aberration	Extended nodal aberration (theoretical)
Spherical aberration	0.0282	0.0281
Coma (in y)	-0.239	-0.274
Astigmatism (axis in 0°)	30.915	31.278

It is known that the wave aberration value in terms of Zernike fringe polynomials depends on the image plane position. Here, the error in coma and astigmatism is much larger compared with spherical aberration, because the biconic surface has very large field-constant astigmatism. Since the spot size is always very large even for the on-axis field, it is hard to find the corresponding image plane location, which gives the accurate wave aberration value for coma. However, if we locate the image plane at the middle position between the tangential and sagittal focal plane, which is -44.44 mm from the biconic mirror, the astigmatism value in terms of Zernike fringe wave aberration will be 31.247, which is much closer to the theoretical value.

References

1. W.J. Smith, E. Betensky, D. Williamson, J.C. Miñano, R. J. Koschel, "The past, present, and future of optical design", Proc. SPIE 6342, 63422Y (2006)
2. H. J. Juranek, R. Sand, J. Schweizer, B. Harnisch, B. P. Kunkel, E. Schmidt, A. Litzelmann, F. Schillke, and G. Dempewolf, "Off-axis telescopes: the future generation of Earth observation telescopes," Proc. SPIE 3439, 104-115 (1998)
3. D. Cheng, Y. Wang, H. Hua, and J. Sasian, "Design of a wide-angle, light-weight head-mounted display using free-form optics tiling," Optics letters 36, 2098-2100 (2011).
4. H. Mayer, "Theodor Scheimpflug," Ophthalmic Research 26, 3-9 (1994).
5. R.E. Fischer, B. Tadic-Galeb, P.R.Yoder, R. Galeb, B.C. Kress, S.C. McClain, T. Baur, R. Plympton, B. Wiederhold and Bob Grant Alastair J, *Optical system design* (New York: McGraw Hill, 2000)
6. R. Kingslake, and R. B. Johnson, *Lens Design Fundamentals* (SPIE, 2010)
7. S. Chang, "Linear astigmatism of confocal off-axis reflective imaging systems with N-conic mirrors and its elimination," J. Opt. Soc. Am. A 32(5), 852–859 (2015).
8. D. Korsch, *Reflective Optics* (Academic Press, 1991)
9. J. C. Miñano, P. Benítez, W. Lin, J. Infante, F. Muñoz, and A. Santamaría, "An application of the SMS method for imaging designs," Opt. Express 17, 24036-24044 (2009)
10. Y. Zhong and H. Gross, "Initial system design method for non-rotationally symmetric systems based on Gaussian brackets and Nodal Aberration Theory," Opt. Express 25, 10016-10030 (2017)
11. H. Gross, *Handbook of Optical Systems* (Wiley-VCH, 2005), Vol. 1
12. L. Seidel. Über die Theorie der Fehler, mit welchen die durch optische Instrumente gesehenen Bilder behaftet sind, und über die mathematischen Bedingungen ihrer Aufhebung. Cotta, (1857)
13. W. T. Welford, *Aberrations of optical systems* (CRC Press, 1986)

14. J. Sasián, *Introduction to aberrations in optical imaging systems* (Cambridge University Press, 2013)
15. K. P. Thompson, "Aberration fields in tilted and decentered optical systems," The University of Arizona (1980).
16. R. Shannon, R. Shack, J. Harvey, and R. Hooker, *Robert Shannon and Roland Shack: legends in applied optics*, (Press Monograph, SPIE Press, 2005).
17. K. P. Thompson, T. Schmid, O. Cakmakci, and J. P. Rolland, "Real-ray-based method for locating individual surface aberration field centers in imaging optical systems without rotational symmetry," *J. Opt. Soc. Am. A* 26, 1503-1517 (2009).
18. A. Gerrard, and J. M. Burch, *Introduction to matrix methods in optics* (Courier Corporation, 1975).
19. M. Herzberger, "Gaussian Optics and Gaussian Brackets*†," *J. Opt. Soc. Am.* 33, 651-655 (1943).
20. M. Herzberger, "Precalculation of Optical Systems*," *J. Opt. Soc. Am.* 42, 637-640 (1952).
21. M. Herzberger, *Modern geometrical optics*, (Krieger Pub Co, 1958).
22. K. Tanaka, "II Paraxial theory in optical design in terms of Gaussian Brackets," *Progress in Optics* 23, 63-111 (1986).
23. G. W. Forbes, "Shape specification for axially symmetric optical surfaces," *Opt. Express* 15, 5218-5226 (2007).
24. A. Broemel, U. Lippmann, H. Gross, "Freeform surface descriptions. Part I: Mathematical representations," *Adv. Opt. Technol.* 6 (5), 327-336 (2017).
25. K. Araki, "Paraxial and aberration analysis of off-axial optical systems." *Optical review* 12.3, 219-222 (2005).
26. K. Fuerschbach, J. P. Rolland, and K. P. Thompson, "Extending Nodal Aberration Theory to include mount-induced aberrations with application to freeform surfaces," *Opt. Express* 20, 20139-20155 (2012).

27. K. Fuerschbach, J. P. Rolland, and K. P. Thompson, "Theory of aberration fields for general optical systems with freeform surfaces," *Opt. Express* 22, 26585-26606 (2014).
28. K. Araki, "Analysis of off-axial optical systems (1)", *Optical Review* 7(3), 221-229 (2000).
29. K. Araki, "Analysis of off-axial optical systems (2)", *Optical Review* 7(4), 326-336 (2000).
30. S.H. Brewer, "Surface-contribution algorithms for analysis and optimization," *J. Opt. Soc. Am.* 66, 8-13 (1976).
31. W. Welford, "A new total aberration formula", *Opt. Acta* 19, 179 (1972).
32. M. Oleszko, R. Hambach and H. Gross, "Decomposition of the total wave aberration in generalized optical systems", *J. Opt. Soc. Am. A* 34, 1856-1864 (2017).
33. J. D. Mansell, R. Suizu, R. Praus, B. Strickler, A. Seward, and S. Coy. "Integrating Wave-Optics and 5x5 Ray Matrices for More Accurate Optical System Modeling." DEPS Fourth Directed Energy Modeling & Simulation Conference (2006).
34. R.H.A. El-Maksoud, M. Hillenbrand, and S. Sinzinger, "Parabasal theory for plane-symmetric systems including freeform surfaces." *Optical Engineering* 53.3, 031303 (2013).
35. H. Zhu, Q. Cui, M. Piao, and C. Zhao, "Design of a dual-band MWIR/LWIR circular unobscured three-mirror optical system with Zernike polynomial surfaces," *Proc. SPIE* 9272, 92720W (2014).
36. S. Chang, J.H. Lee, S.P. Kim, H. Kim, W. J. Kim, I. Song, and Y. Park, "Linear astigmatism of confocal off-axis reflective imaging systems and its elimination," *Appl. Opt.* 45, 484-488 (2006).
37. D. Reshidko, J. Sasian, "Method for the design of nonaxially symmetric optical systems using free-form surfaces," *Optical Engineering* 57(10), 101704 (2018).
38. X. Yuan and X. Cheng, "Lens design based on lens form parameters using Gaussian brackets," *Proc. SPIE* 9272, 92721L (2014).

39. C. Xu, D. Cheng, and Y. Wang. "Automatic obscuration elimination for off-axis mirror systems," *Appl. Opt.* 56, 9014-9022 (2017).
40. T. Yang, J. Zhu, and G. Jin, "Nodal aberration properties of coaxial imaging systems using Zernike polynomial surfaces," *J. Opt. Soc. Am. A* 32, 822-836 (2015).
41. A. Buchroeder and A. S. Leonard, "Wide-Field Tilted-Component Telescope: a Leonard Extended Yolo All-Reflecting System," *Appl. Opt.* 11, 1649-1651 (1972).
42. Y. Zhong and H. Gross, "Imaging system design of extended Yolo telescope with improved numerical aperture," in *Imaging and Applied Optics 2017*, paper IM3E.2 (2017).
43. Y. Zhong and H. Gross, "Improvement of Scheimpflug systems with freeform surfaces," *Appl. Opt.* 57, 1482-1491 (2018).
44. C. Wynne, "Primary aberrations and conjugate change," in *Proceedings of the Physical Society, Section B* 65, 429 (1952).

List of Figures

Figure 2-1 Thin lens model of zoom system [6].....	7
Figure 2-2 Relation of different aberration description [11]	8
Figure 2-3 Marginal ray and chief ray in an off-axis field in the optical system.....	9
Figure 2-4 Polar coordinate of pupil and field height.....	10
Figure 2-5 Longitudinal and transverse chromatic aberrations of blue and red wavelengths.....	12
Figure 2-6 Equivalent local axis and tilt parameter of a spherical surface. [15].....	14
Figure 2-7 The effective field height and the field shift vector of a surface [15].....	15
Figure 2-8 Real-ray-based calculation of the field shift vector. (a) Centered surface for paraxial ray trace (b) tilted surface for real OAR trace.....	17
Figure 2-9 Ray path from the i^{th} component to the j^{th} component.	18
Figure 2-10 Polar coordinate of the surface aperture.....	21
Figure 2-11 Aspherical surface	22
Figure 2-12 Deviation from the basic shape (a) along z-direction (b) projected from the normal direction.....	23
Figure 2-13 Workflow of the traditional design process [5].....	30
Figure 3-1 Classification of systems according to symmetry.....	36
Figure 3-2 Normalized field vector \bar{H} and pupil vector	37
Figure 3-3 Vectorial coordinates in a non-rotationally symmetric system.....	37
Figure 3-4 Non-rotationally symmetric systems with paraxial environment. (a) Anamorphic system; (b) Scheimpflug system.....	41
Figure 3-5 Off-axis systems with paraxial environment. (a) Co-axis two-mirror system; (b) TMA system; (c) HMD system; (d) Yolo telescope.....	42
Figure 3-6 Cartesian surfaces	43
Figure 3-7 Local magnification of an off-axis conic surface.....	46
Figure 3-8 Workflow for the conic-confocal design method in Zemax/OpticStudio.....	46
Figure 3-9 Locations of the coordinate breaks in a conic-confocal setup.....	48
Figure 3-10 Example for conic-confocal method	50
Figure 3-11 Shift of nodal point of a single surface by tilting the surface	52
Figure 3-12 Tilt angles and real-ray-based vectors of plane-symmetric mirror system	53

Figure 3-13 Tilt angles and real-ray-based vectors of plane-symmetric refractive system.....	54
Figure 3-14 Tilt angles and real-ray-based vectors of a mirror tilted in both x- and y- direction	54
Figure 3-15 Different geometric structure of TMA systems. (a) Zigzag structure; (b) Folding structure.....	62
Figure 3-16 Virtual planes in a TMA system to avoid obscuration	63
Figure 3-17 Relation of surfaces and ray bundles to avoid obscuration	64
Figure 3-18 Criteria to check the position of a point (a) in a polygon; (b) outside of the polygon.....	65
Figure 3-19 Pupil shift with finite chief ray height.....	69
Figure 3-20 Decomposition of a biconic surface up to fourth order	75
Figure 3-21 Difference of the ratio \bar{h}/h at the pupil and away from the pupil... ..	78
Figure 4-1 On-axis model of a TMA system	81
Figure 4-2 System performance of the zigzag structure TMA system (a) System layout; (b) Spot diagram with field; (c) RMS Spot radius map with field.....	83
Figure 4-3 Aberrations with field of the zigzag structure TMA system (a) Astigmatism, (b) coma, and (c) grid distortion of initial setup; (d) Astigmatism, (e) coma, and (f) grid distortion of optimized setup; .	84
Figure 4-4 System performance of the folding structure TMA system (a) System layout; (b) Spot diagram with field; (c) RMS Spot radius map with field.....	86
Figure 4-5 Aberrations with field of the compact folding structure TMA system (a) Astigmatism, (b) coma, and (c) grid distortion of initial setup; (d) Astigmatism, (e) coma, and (f) grid distortion of optimized setup;.....	86
Figure 4-6 (a) Layout of the initial extended Yolo telescope; (b) Total spherical aberration; (c) Total coma; (d) Total astigmatism	88
Figure 4-7 Surface contribution of the Yolo telescope (a) Seidel coefficient of coma; (b) Field shift vectors.....	89
Figure 4-8 Full-field-display of coma surface contribution in the initial setup. (a) M1, (b) M2, and (c) M3.....	90
Figure 4-9 (a) 3D System layout of extended Yolo telescope after optimization; (b) MTF of the extended Yolo telescope system for the wavelength 4 μm	90
Figure 4-10 Full-field-display of aberrations of the final design of the extended Yolo telescope. (a) Coma by Zernike fringe coefficients $\sqrt{Z7^2 + Z8^2}$; (b) Astigmatism by Zernike fringe coefficients $\sqrt{Z5^2 + Z6^2}$	91
Figure 4-11 Scheimpflug imaging condition in paraxial approximation	91
Figure 4-12 3D layout of the Scheimpflug system	93

Figure 4-13 Design layout of the Scheimpflug system (a) Starting system with spherical surfaces; (b) Intermediate system with conic surfaces; (c) Final design with two Zernike fringe surfaces.....	94
Figure 4-14 Bar diagram of the ratio \bar{h}/h on each surface.....	95
Figure 4-15 (a) MTF performance of the final Scheimpflug system; (b) Grid distortion of the final Scheimpflug system.....	96
Figure 4-16 Freeform contribution to surface sag of surface 1 (left) and surface 6 (right).....	96
Figure 4-17 RMS spot radius vs field map of the system (a) Starting system with spherical surfaces; (b) Intermediate system with conic surfaces; (c) Final design with two Zernike fringe surfaces.....	96
Figure 4-18 (a) Average RMS spot radius vs field height in Y^* ; Bar diagram of average Zernike fringe aberration coefficients vs field height in Y^* for (b) the starting system, (c) the intermediate system, and (d) the final system.....	97
Figure C-1 Biconic reflective mirror.....	115

List of Tables

Table 2-1 Calculation of primary monochromatic aberration coefficients.....	11
Table 2-2 Chromatic aberration terms	12
Table 2-3 Calculation of the primary chromatic aberration coefficients.....	13
Table 2-4 Shape of the conic sections as a function of the parameter [6, 11] ..	21
Table 2-5 Comparison of different freeform surface representations.....	27
Table 3-1 List of aberrations in scalar and vectorial representations.....	38
Table 3-2 Properties of systems with different symmetry	39
Table 3-3 Surface types in conic-confocal method	44
Table 3-4 Nonlinear functions in the optimization procedure	57
Table 3-5 Primary aberration coefficients generated by the aspherical part of a surface away from the pupil in vectorial representation [14]...	69
Table 3-6 Wavefront deformation generated by term 2 to term 16 of a Zernike fringe surface at the pupil.....	71
Table 3-7 Aberrations generated by terms 7 and 8 of a Zernike fringe surface away from the pupil.....	72
Table 3-8 Aspherical terms of the converted biconic surface	75
Table 3-9 Freeform terms of the converted biconic surface.....	75
Table 3-10 Aberrations generated by the primary astigmatic term	76
Table 3-11 Aberrations generated by the secondary astigmatic term.....	77
Table 3-12 Aberrations generated by the tetrafoil term.....	77
Table 4-1 Specifications of the zigzag TMA system	82
Table 4-2 Initial ray data for paraxial on-axis ray tracing defined at the EnP	82
Table 4-3 Boundary values and solutions of the nonlinear functions for the zigzag structure TMA system	83
Table 4-4 Specifications of the folding structure TMA system	85
Table 4-5 Initial ray data for paraxial on-axis ray tracing defined in the EnP	85
Table 4-6 Boundary values and solutions of the nonlinear functions for the folding structure TMA system	85
Table 4-7 Specifications of the small f-number Yolo telescope system	88
Table 4-8 Design specifications of the Scheimpflug system	92
Table 4-9 Analysis of RMS spot radius for the three systems	98
Table B-1 Wavefront deformation generated by terms 2 and 3	103
Table B-2 Wavefront deformation generated by term 4	103
Table B-3 Wavefront deformation generated by terms 5 and 6	104
Table B-4 Wavefront deformation generated by terms 7 and 8	105
Table B-5 Wavefront deformation generated by terms 9	106

Table B-6 Wavefront deformation generated by terms 10 and 11.....	106
Table B-7 Wavefront deformation generated by terms 12 and 13.....	108
Table B-8 Wavefront deformation generated by terms 14 and 15.....	110
Table B-9 Wavefront deformation generated by term 16	113
Table C-1 Data of the biconic reflective surface.....	115
Table C-2 Calculation of wave aberration coefficients using the Zernike fringe coefficients	116
Table C-3 Comparison of the wave aberration value using Zernike fringe polynomials and the theoretical value calculated based on extended nodal aberration theory (in wavelength unit).....	116

List of Abbreviations

FOV	Field of view
DOF	Depth of field
TMA's	Three mirror anastigmats
HMD	Head-mounted displays
DLS	Damped Least Squares
NAT	Nodal Aberration Theory
SMS	Simultaneous Multiple Surface
MR	Marginal ray
CR	Chief ray
OPD	Optical path difference
TCS	Tilted component systems
OAR	Optical axis ray
GGC's	Generalized Gaussian Constants
Qcon	Strong asphere
Qbfs	Mild asphere
F#	F-number
RMS	Root-mean-square
MTF	Modulate transfer function
EnP	Entrance pupil
ExP	Exit pupil

List of Symbols

$\Delta x'$	Transverse aberration in x
$\Delta y'$	Transverse aberration in y
$\Delta s'$	Longitudinal aberration
R_{ref}	Radius of the reference sphere
x_p	Pupil coordinate in x
y_p	Pupil coordinate in y
n	Refractive index
W	Wave aberration
W_{klm}	Wave aberration coefficients
H	Normalized field height
ρ	Normalized radial aperture height in the pupil coordinate
\overline{H}	Normalized field vector
$\overline{\rho}$	Normalized pupil vector
θ	Azimuthal angle of the pupil coordinate
ϕ	Azimuthal angle of the pupil coordinate
$S_I \sim S_V$	Seidel coefficients
u_j	Marginal ray angle
\overline{u}_j	Chief ray angle
h_j	Marginal ray height
\overline{h}_j	Chief ray height
$H_{Lag\ j}$	Lagrange invariant
$\partial_\lambda W$	Chromatic wave aberration
C_I	Transverse chromatic aberration coefficient
C_{II}	Longitudinal chromatic aberration coefficient
δv	Shift of a surface
β	Tilt angle of a surface
β_0	Total tilt parameter of a surface
O	Center of curvature of a surface
δo	Displacement of the center of curvature

v	Vertex of a surface
c_j	Curvature of the j^{th} surface
$\vec{\sigma}_j$	Displacement of the normalized field vector of the j^{th} surface
\vec{H}_{Aj}	Effective normalized field vector of the j^{th} surface
\vec{i}_j^*	Incident angle of the OAR at the j^{th} surface in the NAT
\vec{S}	Unit normal vector of the intersection point of OAR
\vec{R}	Unit direction vector of the OAR
\vec{N}	Unit normal vector of the object plane
SRL	Direction cosine in x-axis of the unit direction vector of the OAR
SRM	Direction cosine in y-axis of the unit direction vector of the OAR
SRN	Direction cosine in z-axis of the unit direction vector of the OAR
iG_j	Gaussian bracket defined from the i^{th} elements to the j^{th} elements
Φ_j	The power of the j^{th} element for defining the GGC's
$-e'_j$	The reduced distances of the j^{th} element for defining the GGC's
d_i	The distance from the i^{th} surface to the $(i+1)^{\text{th}}$ surface
iA_j	Generalized Gaussian Constant A from the i^{th} surface to the j^{th} surface
iB_j	Generalized Gaussian Constant B from the i^{th} surface to the j^{th} surface
iC_j	Generalized Gaussian Constant C from the i^{th} surface to the j^{th} surface
iD_j	Generalized Gaussian Constant D from the i^{th} surface to the j^{th} surface
f'	Focal length of an element
S'_F	Back focal length of the system
z	Surface sag
κ	Conic parameter of a surface
\vec{r}	Aperture vector of a surface
r	Radial coordinate of an aperture
\bar{r}	Normalized radial aperture coordinate
$Q_m^{\text{con}}(x)$	Polynomials Q-type (strong) asphere
$Q_m^{\text{bfs}}(x)$	Polynomials Q-type (mild) asphere
$Q_m^{\text{Slope}}(\bar{r})$	Normal-departure slope of the polynomials for mild asphere
$Q_n^m(x)$	Forbes polynomials (Q-polynomials)

c_{bfs}	Curvature of best-fit-sphere
$s_{poly}(r)$	Polynomials without projection factor
$z_{poly}(r)$	Polynomials measured along z-axis
r_{norm}	Normalization radius
x_{norm}	Normalization length in x-direction
y_{norm}	Normalization length in y-direction
\bar{x}	Normalized aperture coordinate in x-direction
\bar{y}	Normalized aperture coordinate in y-direction
$A(\bar{x}, \bar{y})$	Boundary function of the general description of a freeform surface
$P(x, y)$	Projection factor of the general description of a freeform surface
$F(\bar{x}, \bar{y})$	Polynomials of the general description of a freeform surface
c_x	Curvature in x of a biconic surface
c_y	Curvature in y of a biconic surface
κ_x	Conic parameter in x of a biconic surface
κ_y	Conic parameter in y of a biconic surface
$Z_i(\bar{r}, \phi)$	Zernike fringe polynomials
$Z_n^m(\bar{r}, \phi)$	Zernike standard polynomials
$T_n(x)$	1D function of Chebyshev polynomials
$P_n(x)$	1D function of Legendre polynomials
$A_i(\bar{x}, \bar{y})$	The i^{th} term of A-polynomials
R_{ptz}	Petzval curvature
m_j	Local magnification of the j^{th} mirror
i_j, i'_j	Incident angle and refractive/reflective angle of the OAR on the j^{th} surface
l, l'	Object distance and image distance of the OAR on a surface
R_j	Radius of curvature of the j^{th} surface
F_j	Confocal points of the Cartesian surfaces
α_j	Tilt angle around z-axis of one surface according to the real OAR

Φ_{skew}	Local focal power according to the Coddington equations
s, s'	Object and image distances in sagittal plane
t, t'	Object and image distances in tangential plane
ω_j	Angles between the lines from a point to the corners of a polygon
C_i	Coefficients of Zernike fringe polynomials
\vec{M}	Vector of coefficients calculated for the wavefront deformation caused by corresponding Zernike fringe terms
$V_{i,j}$	Value of a sampling point for the RMS radius map or the Zernike wave aberration value.

Acknowledgement

I would like to express my deepest gratitude to my supervisor, Prof. Herbert Gross. He not only is my academic supervisor but also influences my way of behavior in life. Since I met him in 2012, he has been imparting his knowledge to me unselfishly. With his generous heart and patience, I was allowed to grow little by little. Whenever I reach rock bottom or have trouble, he always gives me help and support. In the six years of working in his group, I gradually build up my self-confidence and become a person whom I like. Being his student and colleague is a great honor and a pleasure.

I would also like to thank my best friend, Anika Brömel. It is a gift that I could meet such a warm-hearted friend overseas. It is her enthusiasm and selflessness that change me from an introvert person into an open-minded person and to adapt well to the German culture. I am an only child in my family. Her appearance makes me feel like that I have a sister, who cares a lot about my work and life. In the four years of Ph.D. work with her, I feel my life colorful and not alone.

My appreciation also goes to my lovely group members. As the one, who stays longest in the group, I feel honored to appear in every group photo and every important moment with them. In the past few years, all the colleagues in the group have been very friendly to me. I have been working in a happy atmosphere. It is full of good memories, whether it was in the days in the “container” or the days in the IAP building. I would also extend my thanks to those colleagues who offered guidance and support over the years.

In addition, I am thankful to all my friends both in Jena and far away. Thank them for always listening to me and being behind me, when I am full of troubles and worries. They help me survive all the stress from those years and never let me give up.

Last but not least, I am grateful to my parents, who brought me into the world and give me the chance to experience the beauty of life. Many thanks to them for supporting every decision in my life and encouraging me to travel overseas for studying. With their support, I am always brave to embrace all the challenges in my life.

Ehrenwörtliche Erklärung

Ich erkläre hiermit ehrenwörtlich, dass ich die vorliegende Arbeit selbständig, ohne unzulässige Hilfe Dritter und ohne Benutzung anderer als der angegebenen Hilfsmittel und Literatur angefertigt habe. Die aus anderen Quellen direkt oder indirekt übernommenen Daten und Konzepte sind unter Angabe der Quelle gekennzeichnet.

Bei der Auswahl und Auswertung folgenden Materials haben mir die nachstehend aufgeführten Personen in der jeweils beschriebenen Weise ~~entgeltlich~~/unentgeltlich geholfen:

- Herbert Gross, Betreuer.

Weitere Personen waren an der inhaltlich-materiellen Erstellung der vorliegenden Arbeit nicht beteiligt. Insbesondere habe ich hierfür nicht die entgeltliche Hilfe von Vermittlungs- bzw. Beratungsdiensten (Promotionsberater oder andere Personen) in Anspruch genommen. Niemand hat von mir unmittelbar oder mittelbar geldwerte Leistungen für Arbeiten erhalten, die im Zusammenhang mit dem Inhalt der vorgelegten Dissertation stehen.

Die Arbeit wurde bisher weder im In- noch im Ausland in gleicher oder ähnlicher Form einer anderen Prüfungsbehörde vorgelegt.

Die geltende Promotionsordnung der Physikalisch-Astronomischen Fakultät ist mir bekannt.

Ich versichere ehrenwörtlich, dass ich nach bestem Wissen die reine Wahrheit gesagt und nichts verschwiegen habe.



Jena, 23.07.2018

Ort, Datum

Unterschrift d. Verfassers

Curriculum Vitae

Name: Zhong, Yi
Date of birth: 12.06.1989 in Guiyang, Guizhou Province, P.R. China

Education:

10/2011 – 05/2014 Master of Photonics
Friedrich-Schiller-Universität, Jena

09/2007 – 06/2011 Bachelor of Applied Physics
Nankai University (Tianjin, China)

09/2004 – 06/2007 High school (Graduation exam)
Guiyang No.1 High School (Guiyang, China)

09/2001 – 06/2004 Middle school (Graduation exam)
Guiyang No. 17 Middle School (Guiyang, China)

09/1995 – 06/2001 Primary school
Xiang Shi Lu Primary School (Guiyang, China)

Work experience:

07/2014 - Now Research assistant and doctoral candidate
Group: Optical System Design (Prof. Dr. Herbert Gross)
Institute of Applied Physics
Friedrich-Schiller-Universität, Jena



Jena, 23.07.2018

Yi Zhong

Publications

Journals

Y. Zhong and H. Gross,

"Initial system design method for non-rotationally symmetric systems based on Gaussian brackets and Nodal aberration theory,"

Opt. Express 25, 10016-10030 (2017)

Y. Zhong and H. Gross,

"Improvement of Scheimpflug systems with freeform surfaces,"

Appl. Opt. 57, 1482-1491 (2018)

Y. Zhong and H. Gross,

"Vectorial aberrations of biconic surfaces,"

J. Opt. Soc. Am. A 35, 1385-1392 (2018)

A. Broemel, C. Liu, Y. Zhong, Y. Zhang and H. Gross

"Freeform surface descriptions. Part II: Application benchmark",

Adv. Opt. Tech., Vol. 6, 337-347 (2017)

Y. Nie, H. Gross, Y. Zhong, and F. Duerr,

"Freeform optical design for a non-scanning corneal imaging system with a convexly curved image,"

Appl. Opt. 56, 5630-5638 (2017)

Conference proceedings

Y. Zhong, H. Gross, A. Broemel, S. Kirschstein, P. Petruck and A. Tuennermann,

"Investigation of TMA systems with different freeform surfaces",

Proc. SPIE 9626, 9626-0X (2015)

Y. Zhong and H. Gross,

"Imaging system design of extended Yolo telescope with improved numerical aperture," in Imaging and Applied Optics 2017 (3D, AIO, COSI, IS, MATH, pcAOP), OSA Technical Digest (online) (Optical Society of America, 2017), paper IM3E.2.

A. Broemel, H. Gross, D. Ochse, U. Lippmann, C. Ma, Y. Zhong and M. Oleszko,
“Performance comparison of polynomial representations for optimizing optical freeform systems”,
Proc. SPIE 9626, 9626-0W (2015)

H. Gross, A. Broemel, M. Beier, R. Steinkopf, J. Hartung, Y. Zhong, M. Oleszko, and D. Ochse,
“Overview on surface representations for freeform surfaces,”
Proc. SPIE 9626, 9626-0U (2015)

Y. Nie, H. Gross, Y. Zhong, H. Thienpont, and F. Duerr,
"Optical design of freeform mirror systems with tailored field curvatures for corneal imaging,"
in Optical Design and Fabrication 2017 (Freeform, IODC, OFT), OSA Technical Digest (online) (Optical Society of America, 2017), paper JW2C.1.

Talks (only own)

Y. Zhong, H. Gross, A. Broemel, S. Kirschstein, P. Petruck and A. Tuennermann,
"Investigation of TMA systems with different freeform surfaces",
Optical Systems Design 2015: Optical Design and Engineering VI, Jena (2015)

Y. Zhong and H. Gross,
"Imaging system design of extended Yolo telescope with improved numerical aperture,"
IM3E.2 Imaging Systems and Applications (ISA), San Francisco (2017)

Y. Zhong and H. Gross,
"Starting configuration and surface type selection for freeform optical systems,"
Invited talk, UPM workshop (Ultra Precision Manufacturing of Aspheres and Freeforms) Changchun (2017)